

STRUCTURAL AND MAGNETIC PROPERTIES OF PYROCHLORE STRUCTURED MATERIALS

Thesis

Submitted to

DELHI TECHNOLOGICAL UNIVERSITY

For the Award of the Degree of

DOCTOR OF PHILOSOPHY

By

KAILASH CHANDRA

(2K18/PHDAP/517)

Under the Supervision of

Prof. Vinod Singh

Professor

Department of Applied Physics
Delhi Technological University,
New Delhi

Dr. Pawan Kumar Kulriya

Associate Professor

School of Physical Sciences
Jawaharlal Nehru University,
New Delhi



Department of Applied Physics

Delhi Technological University

Bawana Road, Delhi-110042

Dedicated
To
My Loving Family



Delhi Technological University

(Govt. of National Capital Territory of Delhi)

Shahabad Daultpur, Bawana Road, Delhi-110042

CERTIFICATE

This is to certify that the thesis entitled “**Structural and magnetic properties of pyrochlore structured materials**” submitted by **Kailash Chandra (2K18/PHDAP/517)** to Delhi Technological University (DTU) Delhi, India for the degree of Doctor of Philosophy, is a bonafide record of research work carried out by him under our supervision and guidance. This work embodied in this thesis has been carried out in the Nano Fabrication Laboratory, Department of Applied Physics Delhi Technological University (DTU), Delhi, India, and Advanced Materials Research Laboratory, School of Physical Sciences (SPS) Jawaharlal Nehru University (JNU) New Delhi, India. The work of this thesis is original and has not been submitted in parts or fully to any other institute or university for the award of any other degree or diploma.

Prof. Vinod Singh
Professor
Department of Applied Physics
Delhi Technological University
Delhi- 110042, India

Dr. Pawan Kumar Kulriya
Associate Professor
School of Physical Sciences
Jawaharlal Nehru University
Delhi- 110067, India



Delhi Technological University
(Govt. of National Capital Territory of Delhi)
Shahabad Daulatpur, Bawana Road, Delhi-110042

DECLARATIONS

I *Kailash Chandra*, hereby certify that the thesis titled “*Structural and magnetic properties of pyrochlore structured materials*” submitted in the fulfilment of the requirement for the award of the degree of the Doctor of Philosophy is an authentic record of my research work carried out under the supervision of *Prof. Vinod Singh* and *Dr. Pawan Kumar Kulriya*. This work in the same form or any other form has not been submitted by me or anyone else earlier for any purpose. Any material borrowed or referred to is duly acknowledged.

Kailash Chandra
(2K18/PHDAP/517)
Department of Applied Physics
Delhi Technological University
Delhi- 110042, India

ACKNOWLEDGEMENT

First and above all, I thank almighty for giving me the strength and patience to work through all the years.

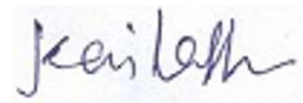
I express my sincere thanks to my esteemed research supervisor, **Prof. Vinod Singh**, for his supervision, genuine advice and valuable guidance from the early stage of the research. His dedication, scientific intuition and motivation have exceptionally inspired me. I owe him special thanks for always helping me out in all official work and enabling me to accomplish my Ph.D. thesis on time. Despite all his other tasks, he still finds time to discuss about research and our well being too.

Special thanks to my research co-supervisor, **Dr. Pawan Kumar Kulriya**, for integrating me in his group and providing a nice scientific environment. I am grateful for the insightful discussions, valuable advice and trust he showed during the research work. He is a person with foresight, benevolence, enthusiasm and patience. He never turns me to wait for any research related work. Throughout my Ph.D. duration, he provided sound advice, a good company and a lot of good ideas for research related work. I feel very fortunate having had the opportunity to complete this challenging journey under his guidance.

My sincere thanks also go to Hon'ble Vice chancellor, DTU **Prof. Jai Prakash Saini**, and officials of DTU for their precious support and providing ample research facilities to conduct this research. I would also like to thank head of the department **Prof. A. S. Rao**, for developing a research friendly environment in the department. Moreover, I would also thank all other faculty and staff members of department of applied physic DTU, for their help and cooperation throughout my research period.

I express my heartfelt gratitude to all my colleagues, labmates and friends **Deshraj Meena, Ashok Kumar, Yogendra Singh Shekhawat, Saurabh Kumar Sharma, Nikita Jain, Anurag, Umang, Priya, Ramesh Kulriya, Jasveer Singh, Shivani, Vivek Mithaliya, Ankita Rawat, Anju Sihag and Naima Tyagi** for their constant motivation and support during my research work.

I want to pay high regard to my father, **Mr. Ishwar Agarwal**, and my mother **Mrs. Prema Devi**, for their love constant care and emotional support throughout my life. Their faith trust and confidence in me always pushed me towards my goal. Last but not least, I would like to thank my wife **Mrs. Khushbu Jain** for always being there for me. I would not have started this journey without her encouragement. The love from my beautiful daughter **Aanvika Garg** kept me motivated throughout.



Kailash Chandra

ABSTRACT

This thesis focuses on the investigations of structural and magnetic behavior of pyrochlore structured materials synthesized by standard solid-state method. The two main ideas of my work magnetism and geometric frustration are discussed in this thesis. This work explores the substitution effect at A site and B site of $\text{Ho}_2\text{Ti}_2\text{O}_7$ pyrochlore on structural and magnetic properties and understands the frustration phenomenon at low temperatures. The pyrochlore structured ceramic $\text{A}_2\text{B}_2\text{O}_7$ (A and B stand for rare earth elements and transition metal respectively) has fascinated an excessive deal of research interest over the last two decades. Important titanate oxides ($\text{A}_2\text{Ti}_2\text{O}_7$) have a wide range of applications, such as solid catalysts, electrolytes, nuclear reactor materials, and more. Due to its unique low temperature magnetic characteristics, $\text{Ho}_2\text{Ti}_2\text{O}_7$ is known for both its remarkable spin ice behaviors and its evident quantum nature. A crucial aspect of focus for theorists and experimenters is geometrical frustration in pyrochlore oxides. Strong magnetic characteristics are provided by rare-earth ions with unpaired electrons in the 4f configuration, which exhibits enormous magnetic moments. The effect of B site Ge doped pyrochlore titanate $\text{Ho}_2(\text{Ti}_{1-x}\text{Ge}_x)_2\text{O}_7$ ($x = 0.0, 0.2$ and 0.4) is detailed, along with its structural and magnetic behaviors. As per structural analysis, the pyrochlore superstructural ordering improves with rising x-value in $\text{Ho}_2(\text{Ti}_{1-x}\text{Ge}_x)_2\text{O}_7$ as seen by the increase in radii ratio (R_A/R_B) or variation in O_{48f} oxygen as on increasing Ge content over Ti. Further confirmation of the pyrochlore phase with hardness of the phonon mode by Raman spectroscopy was provided by the interaction between phonons and the phonon anharmonic. Conversely, magnetic analysis of the spin-frustrated material $\text{Ho}_2(\text{Ti}_{1-x}\text{Ge}_x)_2\text{O}_7$ pyrochlore revealed a decrease in magnetization caused by weakened ferromagnetic character and non-magnetic 16c site contributed by rise in chemical pressure. Strong crystal field generated Ising type anisotropy which results in a "two-in/two-out" arrangement in the spin

configuration according to the spin ice rule produces ferromagnetic exchange interactions. Thus, pyrochlore structured compositions that are more stable exhibit less ferromagnetic character. Further, despite reducing the temperature to 2 K, no spin glass like transition was seen. Further, we have also studied the effect of A site nonmagnetic La^{3+} doping on magnetic and structural behavior of $\text{Ho}_{2-x}\text{La}_x\text{Ti}_2\text{O}_7$ ($x = 0.0, 0.1, \text{ and } 0.2$) pyrochlore. Structural studies revealed that a stable single-phasic pyrochlore crystal structure had formed. Raman research has shown the red and blue shift of the phonon mode and an increase in structural ordering as a result of the inclusion of La^{3+} into $\text{Ho}_{2-x}\text{La}_x\text{Ti}_2\text{O}_7$, which has increased the ionic radii ratio. In all specimens, it was noted that the ferromagnetic feature continuously reduces with chemical pressure. This trend in the magnetic data is caused by variations in the dipolar and exchange interaction. A comparison of the doping at the A and B sites in the $\text{Ho}_2\text{Ti}_2\text{O}_7$ demonstrates that the θ_{CW} dropped by 71% and 33% as a result of 10% doping of larger cations (La^{3+}) at the A site and smaller cations (Ge^{4+}) at the B site respectively. These findings support the conclusion that B site doping is more susceptible to controlling magnetic characteristics than A site doping. $\text{Ho}_2\text{Ti}_2\text{O}_7$ doped with La^{3+} showed a significant decrease in the θ_{CW} indicating that the θ_{CW} can be tuned by doping at the A site. Finally, Probed the influence of Ho^{3+} substitution at A-site on structural and magnetic studies of $(\text{Gd}_{1-y}\text{Ho}_y)_2\text{Ti}_2\text{O}_7$ ($y = 0.0, 0.2, 0.4 \text{ and } 0.8$) pyrochlore. Antiferromagnetically (AFM) linked Heisenberg spins are predicted to be extremely frustrating in the $\text{Gd}_2\text{Ti}_2\text{O}_7$ pyrochlore lattice because there are numerous ways to minimize the exchange energy. The result of rising Ho content is that there is increase in magnetic parameters (θ_{CW} and μ_{eff}) and decrease in the ionic radii ratio ($R_{\text{A}}/R_{\text{B}}$) which leads to enhancement of ferromagnetic feature of the materials. Magnetic studies have also demonstrated the system becomes less antiferromagnetic (AFM) character as a result of the increased chemical pressure in $\text{Gd}_2\text{Ti}_2\text{O}_7$. This is due to generation of ferromagnetic interaction among Gd–Ho (Ho–Ho) spins and disrupted network of Gd^{3+} ions. This character is considered

to be relevant to the fight between FM and AFM interaction, which is correlated to local structural disorder and magnetic frustration. Although, Magnetic investigations did not reveal any evidence of a spin glassy pattern in all compositions. Based on these findings, it is logical to conclude that B site doping is more capable of controlling magnetic characteristics than A site doping. Furthermore, the nature and location of the dopant have an impact upon the value of θ_{CW} changes. As conclusion, when comparing the current work to prior findings, a higher increment in θ_{CW} was seen with an equivalent quantity of doping. This may be caused by the Gd-Ho cation's significant crystal field splitting. Structural evaluation has proven that cubic pyrochlore (impurity-free) crystals with a cell parameter that continuously shrinkage and justifies Vegard rule. The crystallite size figured from W-H graph is diminished with magnetic Ho substituting which is validate the reduction in structural ordering of prepared specimens. Raman bands show the red and blue shift of phones modes with increasing Ho content. Single ion anisotropy with dipolar exchanges was realized to harvest interesting magnetic assets. Examining this structure's whole AC and DC magnetic learning is exceedingly difficult. It would be exciting to examine the crystal structural transformations of such systems in the future at temperatures where spin ices are prone to freezing and becoming unstable.

List of Publications

Part of Thesis:

1. **Kailash Chandra**, Vinod Singh, Saurabh K. Sharma, and Pawan K. Kulriya, "Structural magnetic properties correlation in Ge doped frustrated $\text{Ho}_2\text{Ti}_2\text{O}_7$ pyrochlore." *Journal of Magnetism and Magnetic Materials* 561(2022):169694 **(Impact factor- 3.09)**
2. **Kailash Chandra**, Vinod Singh, Saurabh K. Sharma, and Pawan K. Kulriya, " La^{3+} substitution effect on structural and magnetic properties of frustrated $\text{Ho}_2\text{Ti}_2\text{O}_7$ pyrochlore." *Journal of Alloys and Compounds* 937(2022):168311 **(Impact factor- 6.34)**
3. **Kailash Chandra**, Vinod Singh, Saurabh K. Sharma, and Pawan K. Kulriya, "Probing the influence of Ho^{3+} doping on structural and magnetic properties of $(\text{Gd}_{1-y}\text{Ho}_y)_2\text{Ti}_2\text{O}_7$ pyrochlore". *Journal of Alloys and Compounds* 960 (2023):170779 **(Impact factor- 6.34)**

Not Part of Thesis:

1. Vinod Singh, Pawan K. Kulriya, Ashok Kumar, Ramesh Kumar, Priya Pradeep Kumar, Umang Berwal, **Kailash Chandra**, and Kedar Singh. "Hydrogen induced structural modifications in size selected Pd-Carbon core-shell NPs: Effect of carbon shell thickness, size and pressure." *International Journal of Hydrogen Energy* 47(2022): 12642-12652 **(Impact factor- 7.139)**

CONTENTS

	<i>Page No.</i>
<i>Certificate</i>	i
<i>Candidate's Declaration</i>	ii
<i>Acknowledgement</i>	iii
<i>Abstract</i>	v
<i>List of Publications</i>	viii
<i>List of Figures</i>	xii
<i>List of Tables</i>	xvi
CHAPTER - 1: Introduction	1 – 40
1.1 Background	3
1.2 Pyrochlore Structured Materials	3
1.3 Pyrochlore Structure	5
1.4 Electron Magnetic Moment	8
1.5 Atomic Magnetic Moment	9
1.6 Magnetic Interaction	9
1.7 Geometrical Frustration	13
1.8 Spin Ice Phase	16
1.9 Spin Glassy Phase	20
1.10 Literature Review	22
1.11. Motivation and Scope of Work	28
1.12 Objectives of the Thesis	29
1.13. Arrangement of Thesis	29
References:	32
CHAPTER - 2: Techniques for Synthesis and Characterization	41 – 63
2.1 Introduction	42

2.2	Solid-State Sintering Synthesis Method	43
2.2.1	Application of Solid-State Sintering Method	46
2.3	Techniques for Structural Analysis	46
2.3.1	X-Ray Diffraction Technique	46
2.3.2	Raman Spectroscopic Technique	52
2.4	Scanning Electron Microscopy (SEM) Technique	55
2.4.1	Fundamentals of SEM	56
2.4.2	Applications of SEM	57
2.5	Physical Property Measurement System (PPMS)	57
2.5.1	Application of PPMS	60
	References:	61

CHAPTER - 3: Structural Magnetic Properties Correlation in B- Site Ge

Doped Frustrated Ho₂Ti₂O₇ Pyrochlore 64 – 95

3.1	Introduction	66
3.2	Synthesis and Characterization	68
3.3	Results and Discussions	69
3.3.1	Structural Investigation using XRD	69
3.3.2	Raman Spectroscopy Investigation	76
3.3.3	Compositions and Microstructure Analysis	79
3.3.4	Magnetization Investigations	83
3.4	Conclusion	88
	References:	89

CHAPTER - 4: A Site La³⁺ Substitution Effect on Structural and Magnetic

Properties of Frustrated Ho₂Ti₂O₇ Pyrochlore 96 – 128

4.1	Introduction	98
4.2	Synthesis and Characterization	99
4.3	Results and Discussions	99

4.3.1	Stability and Structural Investigation <i>via</i> XRD	101
4.3.2	Structural Investigation <i>via</i> Raman Spectroscopy	108
4.3.3	Composition and Microstructure Investigation	111
4.3.4	DC Magnetization Study	115
4.4	Conclusion	121
	References:	123
CHAPTER - 5: Probing the Influence of Ho³⁺ Substitution at A-site on Structural and Magnetic Studies of (Gd_{1-y}Ho_y)₂Ti₂O₇ (y = 0.0, 0.2, 0.4 and 0.6) Pyrochlore		129 – 158
5.1	Introduction	131
5.2	Experimental Procedure	133
5.3	Results and Discussions	134
5.3.1	Stability and Structural Investigation using XRD	134
5.3.2	Raman Spectroscopic Study	141
5.3.3	Compositional Analysis by EDX	144
5.3.4	Study of DC Magnetization	145
5.4	Conclusion	151
	References:	153
CHAPTER - 6: Summary and Future Perspective		159 – 164
6.1	Summary	161
6.2	Future Perspective	164

LIST OF FIGURES

<i>Fig. No.</i>		<i>Page No.</i>
CHAPTER - 1:		
1.1	Element that can be arranged in the pyrochlore phase are listed in the periodic table.	5
1.2	Rare earth pyrochlore oxide stability field.	7
1.3	Magnetic moments are arranged in (a) parallel arrangement (FM) and (b) antiparallel arrangement (AFM).	11
1.4	Diagram of Mn^{3+} - O^{2-} - Mn^{4+} super exchange interaction with a 180° bond angle.	12
1.5	Two-dimensional triangular lattice that is geometrically frustrated has (a) antiferromagnetic and (b) 120° aligned structure.	14
1.6	Spins aligned antiferromagnetically on a tetrahedron's vertices cause geometric frustration.	15
1.7	Spin configuration in the pyrochlore oxide with a two in two out ordering.	17
1.8	Pyrochlore phase diagram of Ising spin. The spin ice phase is constant above $\frac{J_{nn}}{D_{nn}} \sim -0.91$. It is anticipated that an all-out antiferromagnetic phase will occur below the critical point. The curve has markers for the recognized spin ices.	19
1.9	Spin glassy behavior of (a) $Y_2Ir_2O_7$ and (b) $Lu_2Ir_2O_7$ pyrochlore.	21
1.10	Spin glassy behavior of $Y_2Ir_{2-x}Fe_xO_7$ pyrochlore.	22
1.11	Temperature disparity of susceptibility (AC) at field of 0 K Oe (a & b) and 10 K Oe for $Eu_2Ti_2O_7$ for frequencies changed (c & d).	25
CHAPTER - 2:		
2.1	Schematic diagram of the solid-state sintering process.	45
2.2	Fundamental idea behind XRD (Braggs Law).	47
2.3	Photograph of the X-ray diffractometer system at the School of Physical Sciences, Jawaharlal Nehru university, New Delhi	50
2.4	Figure illustrates Stokes, anti-Stokes, and Rayleigh Raman scatter.	54

<i>Fig. No.</i>	<i>Page No.</i>
2.5	56
2.6	59
CHAPTER - 3:	
3.1	71
3.2	72
3.3	74
3.4	77
3.5	79
3.6	81
3.7	86

3.8	The variation of magnetization (M) vs magnetic field (H) of $\text{Ho}_2(\text{Ti}_{1-x}\text{Ge}_x)_2\text{O}_7$ at 2K.	87
CHAPTER - 4:		
4.1	Flowchart displays the detailed synthesis process of $\text{Ho}_{2-x}\text{La}_x\text{Ti}_2\text{O}_7$.	100
4.2	XRD pattern of $\text{Ho}_{2-x}\text{La}_x\text{Ti}_2\text{O}_7$ with $x = 0.3$ and 0.4 . Single phase is not observed for these compositions. Contaminated peaks are marked by asterisk.	102
4.3	Refined XRD profiles for (a) $\text{Ho}_2\text{Ti}_2\text{O}_7$, (b) $\text{Ho}_{1.9}\text{La}_{0.1}\text{Ti}_2\text{O}_7$, and (c) $\text{Ho}_{1.8}\text{La}_{0.2}\text{Ti}_2\text{O}_7$.	103
4.4	An enlarged view of (222) planes for a variation in (a) peak position, (b) peak intensity with x value, and (c) lattice constant as well as a parameter of O_{48f} as a doping concentration of La in $\text{Ho}_{2-x}\text{La}_x\text{Ti}_2\text{O}_7$.	104
4.5	W-H linear plots for (a) $x = 0.0$, (b) $x = 0.1$, and (c) $x = 0.2$. A representative for the variation in estimated (d) Crystallite size as well as microstrain.	107
4.6	(a) Raman spectra of $\text{Ho}_{2-x}\text{La}_x\text{Ti}_2\text{O}_7$ with $x = 0.0, 0.1$, and 0.2 compositions, (b) variation in Raman active modes as a function of La-doping concentration.	108
4.7	Deconvoluted Raman spectra for $x = 0.0, 0.1$, and 0.2 .	109
4.8	(a, c, and e) SEM images and (b, d and f) grain size distribution (a representation through histogram and size estimation through Gaussian fitting) of $\text{Ho}_{2-x}\text{La}_x\text{Ti}_2\text{O}_7$ ($x = 0.0, 0.1$ and 0.2) system.	112
4.9	Magnetic susceptibility vs temperature plots of $\text{Ho}_{2-x}\text{La}_x\text{Ti}_2\text{O}_7$ ($x = 0.0, 0.1$ and 0.2 figure a, b and c, respectively) compounds in the presence of 1000 Oe magnetic field (FC and ZFC). Inset: FC and ZFC curves recorded in the range of 2 – 50 K.	116
4.10	(a) Display the inverse susceptibility (χ^{-1}) vs. temperature of the $\text{Ho}_{2-x}\text{La}_x\text{Ti}_2\text{O}_7$ ($x = 0.0, 0.1$ and 0.2) specimens with functional field of 1000 Oe. (b) Effective magnetic moments were estimated from Curie Weiss (CW) law at temperature (100 – 300 K). The Curie Weiss temperatures were calculated from fitting at temperature range of (c) 100 – 300 K, and (d) 2 – 20 K.	117

<i>Fig. No.</i>		<i>Page No.</i>
4.11	M-H diagrams of $\text{Ho}_{2-x}\text{La}_x\text{Ti}_2\text{O}_7$ specimens recorded at 2 K.	120

CHAPTER - 5:

5.1	Schematic figure of method used in the synthesis of $(\text{Gd}_{1-y}\text{Ho}_y)_2\text{Ti}_2\text{O}_7$ samples.	134
5.2	A series of refined XRD patterns of $(\text{Gd}_{1-y}\text{Ho}_y)_2\text{Ti}_2\text{O}_7$ with concentration of Ho: (a) $y = 0.0$, (b) 0.2, (c) 0.4, and (d) 0.6.	136
5.3	(a) A shift in (111) diffraction maximum, (b) variation in lattice constant and x -parameter of O_{48f} as on increasing Ho concentration in $(\text{Gd}_{1-y}\text{Ho}_y)_2\text{Ti}_2\text{O}_7$.	138
5.4	Refined crystal structure for $\text{Gd}_2\text{Ti}_2\text{O}_7$. Violet polyhedron represents $[\text{GdO}_6^{48f}\text{O}_2^{8b}]$ hexagonal bipyramid and green polyhedron represents TiO_6^{48f} octahedra.	139
5.5	Williamson-Hall (W-H) plots of $(\text{Gd}_{1-y}\text{Ho}_y)_2\text{Ti}_2\text{O}_7$ with concentration of Ho: (a) $y = 0.0$, (b) 0.2, (c) 0.4, and (d) 0.6 and (e) a variation in crystallite size and microstrain as a function of Ho concentration.	140
5.6	(a) Raman spectrum of $(\text{Gd}_{1-y}\text{Ho}_y)_2\text{Ti}_2\text{O}_7$ with $y = 0.0, 0.2, 0.4$ and 0.6 (b-e) Raman spectra that have been deconvoluted for $y = 0.0, 0.2, 0.4$ and 0.6.	142
5.7	Raman active modes vary in relation to the amount of Ho doping.	143
5.8	Plots of $(\text{Gd}_{1-y}\text{Ho}_y)_2\text{Ti}_2\text{O}_7$ specimens magnetic susceptibility vs temperature (FC and ZFC) at operational field of 1 kOe for (a) $y = 0$ (b) $y = 0.2$ (c) $y = 0.4$ and (d) $y = 0.6$ Inset: FC and ZFC patterns recorded between 2 and 50 K.	146
5.9	(a) The temperature-dependent inverse susceptibility (χ^{-1}) curve for the GHTO ($y = 0, 0.2, 0.4$, and 0.6) compounds. The estimated Curie Weiss temperatures from fitting at temperature range of (b) 2 – 20 K and (c) 100 – 300 K (d) Estimated effective magnetic moments at temperature (100 – 300 K).	148
5.10	M-H graphs of samples of $(\text{Gd}_{1-y}\text{Ho}_y)_2\text{Ti}_2\text{O}_7$ taken at 2 K.	149

LIST OF TABLES

<i>Table No.</i>	<i>Page No.</i>
CHAPTER - 1:	
1.1 The cubic pyrochlore structure's crystallographic locations and Wyckoff Regularity for position coordinates.	6
CHAPTER - 3:	
3.1 Structural parameters calculated from Rietveld fitting and W-H plots of diffraction patterns for $\text{Ho}_2(\text{Ti}_{1-x}\text{Ge}_x)_2\text{O}_7$.	75
3.2 Experimental and nominal mass (%) of the $\text{Ho}_2(\text{Ti}_{1-x}\text{Ge}_x)_2\text{O}_7$ compounds.	80
3.3 The calculated values of theoretical density, experimental bulk density, and grain size for $\text{Ho}_2(\text{Ti}_{1-x}\text{Ge}_x)_2\text{O}_7$.	81
3.4 Magnetic parameters calculated (experimentally) from curie Weiss law fitting for $\text{Ho}_2(\text{Ti}_{1-x}\text{Ge}_x)_2\text{O}_7$.	85
CHAPTER - 4:	
4.1 Parameters (structural) estimated from W-H plots and Rietveld analysis for $\text{Ho}_{2-x}\text{La}_x\text{Ti}_2\text{O}_7$.	106
4.2 The position of deconvoluted Raman active modes for all three compositions.	109
4.3 Nominal and experimental mass (%) of $\text{Ho}_{2-x}\text{La}_x\text{Ti}_2\text{O}_7$ ($x = 0.0, 0.1, \text{ and } 0.2$).	111
4.4 The theoretical density, experimental density and grain size estimated for specimens ($x = 0.0, x = 0.1, \text{ and } x = 0.2$).	114
4.5 Experimentally observed magnetic parameters of the $\text{Ho}_{2-x}\text{La}_x\text{Ti}_2\text{O}_7$ ($x = 0.0, 0.1, 0.2$) system.	119

CHAPTER - 5:

- 5.1 The structural parameters for $(\text{Gd}_{1-y}\text{Ho}_y)_2\text{Ti}_2\text{O}_7$ that were calculated from W-H plots and Rietveld analyses. **137**
- 5.2 Deconvoluted Raman active mode locations for each of the three compositions. **143**
- 5.3 The $(\text{Gd}_{1-y}\text{Ho}_y)_2\text{Ti}_2\text{O}_7$ compounds' nominal and experimental mass (%) are displayed. **145**
- 5.4 The magnetic parameters of $(\text{Gd}_{1-y}\text{Ho}_y)_2\text{Ti}_2\text{O}_7$ as observed experimentally. **148**

List of Abbreviations

PPMS	Physical Properties Measurement System
SEM	Scanning Electron Microscope
XRD	X-Ray Diffraction
EDX	Energy Dispersive X-Ray
FM	Ferromagnetic
AFM	Antiferromagnetic
R_A/R_B	Ionic Radii Ratio
θ_{CW}	Curie Weiss Temperature
μ_{eff}	Effective Magnetic Moment
M_{sat}	Saturation Magnetization
FCC	Face Centred Cubic

Chapter 1

Introduction

The motivation for the current thesis work is explained in this chapter along with an introduction. Here is a short introduction to ceramics with pyrochlore structures that have a wide range of electrical and magnetic characteristics. This chapter briefly describes the background of magnetism in pyrochlore-structured ceramics. The basic concepts underlying magnetic interactions in spin systems and role played by the magnetic systems in frustration are discussed. Earlier findings pertaining to low-temperature magnetic phases of pyrochlore compounds that share the same rare earth in $R_2Ti_2O_7$ as the compounds examined in this work are also explained. Motivation, scope of proposed research work and objectives of the thesis are also included in this chapter. The chapter's conclusion provides the thesis organisational structure.

1.1 Background

The pyrochlore structured ceramic $A_2B_2O_7$ (A and B stand for rare earth elements and transition metal respectively) has fascinated an excessive deal of research interest over the last two decades. The two main ideas of proposed research work magnetism and geometric frustration are introduced in this chapter. A crucial aspect of focus for theorists and experimenters is geometrical frustration in pyrochlore oxides. First, examine the idea of a magnetic moment, interactions among magnetic moments, as well as how changes in a crystal environment affect magnetic assets is described. After that, merging of local moments and exchanges results in ordered states is discussed. We also introduce idea of geometric frustration and discuss how it relates to exotic magnetic phases before going on to describe the crystalline structure of frustrated experimental understandings. The results for the rare-earth frustrated systems that are subject to this work are then discussed. Such systems include pyrochlores long range ordered phases $Gd_2Ti_2O_7$ and $Er_2Ti_2O_7$, spin ices $Dy_2Ti_2O_7$ and $Ho_2Ti_2O_7$, and spin liquid $Tb_2Ti_2O_7$. Important potential titanates oxides have several uses including as materials for nuclear reactors, solid catalysts and electrolytes, etc.

1.2 Pyrochlore Structured Materials

The geometric frustration with the corner-sharing tetrahedron system in materials has drawn a lot of scientific concern to the magnetic pyrochlore oxides over the past 20 years [1-2]. Amongst the diverse multifaceted oxides, pyrochlore materials display widespread outstanding chemical and physical characteristics, greater acceptance of radiation damage, larger thermal constancy, higher melting point, high conduction, small stimulation energy, and small extension factor, for example [3-4]. These qualities of pyrochlore material brand them an

appropriate applicant for several high-tech applications, for example, high temperature thermal wall coating solid, nuclear excess environment substantial, catalysts, nuclear reactor materials, solid oxide fuel cells and electrolytes etc. [5-9]. Pyrochlore oxide research has grown significantly with a significant percentage of the work concentrating on specimens that have experienced magnetic frustration. Numerous cations that can occupy lattice spots have magnetic moments that are not zero. As a result, the pyrochlore lattice's extremely vast compositional solidity field has given rise to a wide range of magnetic materials [10]. Pyrochlores are actually among the materials that are generally recognized as being the best for the methodical research of magnetism. $A_2B_2O_7$ is the chemical formula for the family of chemicals known as pyrochlore oxides. The cubic pyrochlore frame is a member of the space group of $Fd\bar{3}m$. The A and B particles are said to each reside in the apogees of one such link in the pyrochlore frame, which is defined as two diffusing networks of tetrahedrons [11]. Abundance of ingredients that can reside in the A and B locations can help to partially explain why the pyrochlore lattice is so popular (**Fig. 1.1**). For the study of geometric frustration, pyrochlore is optimal structured material. A sizeable part of positive ions that can lodge the framework is the magnetic cations, they are usually encountered in the A site. The tetrahedra arrangement of sharing corners over both A and B spots causes high degrees of discontent. Investigating movements, like the impact of changing the magnetic moment or lattice constant, is made easier by the enormous stability field. These factors have led to the pyrochlore ceramics emergence as an inspiration for exotic and unusual magnetic features.

1																	2				
H																	He				
3	4															5	6	7	8	9	10
Li	Be															B	C	N	O	F	Ne
11	12															13	14	15	16	17	18
Na	Mg															Al	Si	P	S	Cl	Ar
19	20	21	22	23	24	25	26	27	28	29	30	31	32	33	34	35	36				
K	Ca	Sc	Ti	V	Cr	Mn	Fe	Co	Ni	Cu	Zn	Ga	Ge	As	Se	Br	Kr				
37	38	39	40	41	42	43	44	45	46	47	48	49	50	51	52	53	54				
Rb	Sr	Y	Zr	Nb	Mo	Tc	Ru	Rh	Pd	Ag	Cd	In	Sn	Sb	Te	I	Xe				
55	56	71	72	73	74	75	76	77	78	79	80	81	82	83	84	85	86				
Cs	Ba	Lu	Hf	Ta	W	Re	Os	Ir	Pt	Au	Hg	Tl	Pb	Bi	Po	At	Rn				
Lanthanides		57	58	59	60	61	62	63	64	65	66	67	68	69	70						
		La	Ce	Pr	Nd	Pm	Sm	Eu	Gd	Tb	Dy	Ho	Er	Tm	Yb						

Fig. 1.1 Elements that can be arranged in the pyrochlore phase are listed in the periodic table.

1.3 Pyrochlore Structure

The pyrochlore lattice $A_2B_2O_6O'$ has four crystallographically different atoms, as illustrated in **Table 1.1**. While the B site has octahedral coordination, eight-fold oxygen coordination exists at the A site. The oxygen x parameter, which accepts values in the range of 0.3125 to 0.375, is the only changeable lattice position [12]. The positioning parameter for oxygen x value controls the coordination of polyhedral form around the A and B sites. The BO_6 polyhedral is octahedral at $x = 0.3125$, whereas the AO_8 polyhedral is cubic at $x = 0.375$. However as both requirements cannot be met at once, the ideal cubic and octahedral polyhedra are distorted when x usually takes an intermediate value [13].

Table 1.1 The cubic pyrochlore structure's crystallographic locations and Wyckoff Regularity for position coordinates.

Atom	Position Coordinates	Wyckoff Regularity
A	$\frac{1}{2}, \frac{1}{2}$ and $\frac{1}{2}$	16d
B	0, 0 and 0	16c
O	x, $\frac{1}{8}$ and $\frac{1}{8}$	48f
O'	$\frac{3}{8}, \frac{3}{8}$ and $\frac{3}{8}$	8b

Trivalent (rare earth atoms) pyrochlore lattice members normally occupy the A site, while tetravalent (+4) p-block or d-block ions often occupy the B slot. Although it is also likely to find (2+, 5+) pyrochlores, these alleged (3+, 4+) pyrochlores are the most typical. With the development of high pressure and temperature synthesis methods, new pyrochlores could be created, and the known stability field could now be expanded [14]. All of the pyrochlore compounds addressed moving forward are of the (3+, 4+) variety. The radius ratio of A and B positions (Ionic Radii Ratio = R_A^{3+}/R_B^{4+}), which determines the solidity of pyrochlore structured ceramic is key element. **Fig. 1.2** displays the radius of each element of A and B slots. The stability of ceramics with pyrochlore structures is strongly influenced by the ionic radius ratio. Maximum pyrochlore oxide lies within the range of 1.43-1.76. If the radii ratio is between ($1.43 \leq RR \leq 1.76$) stable pyrochlore structure is produced. When R is less than or equal to 1.43, the resulting structure is a fluorite structure with deficiency of anion and when R is larger than or equal to 1.76, it becomes a monoclinic structure [15].

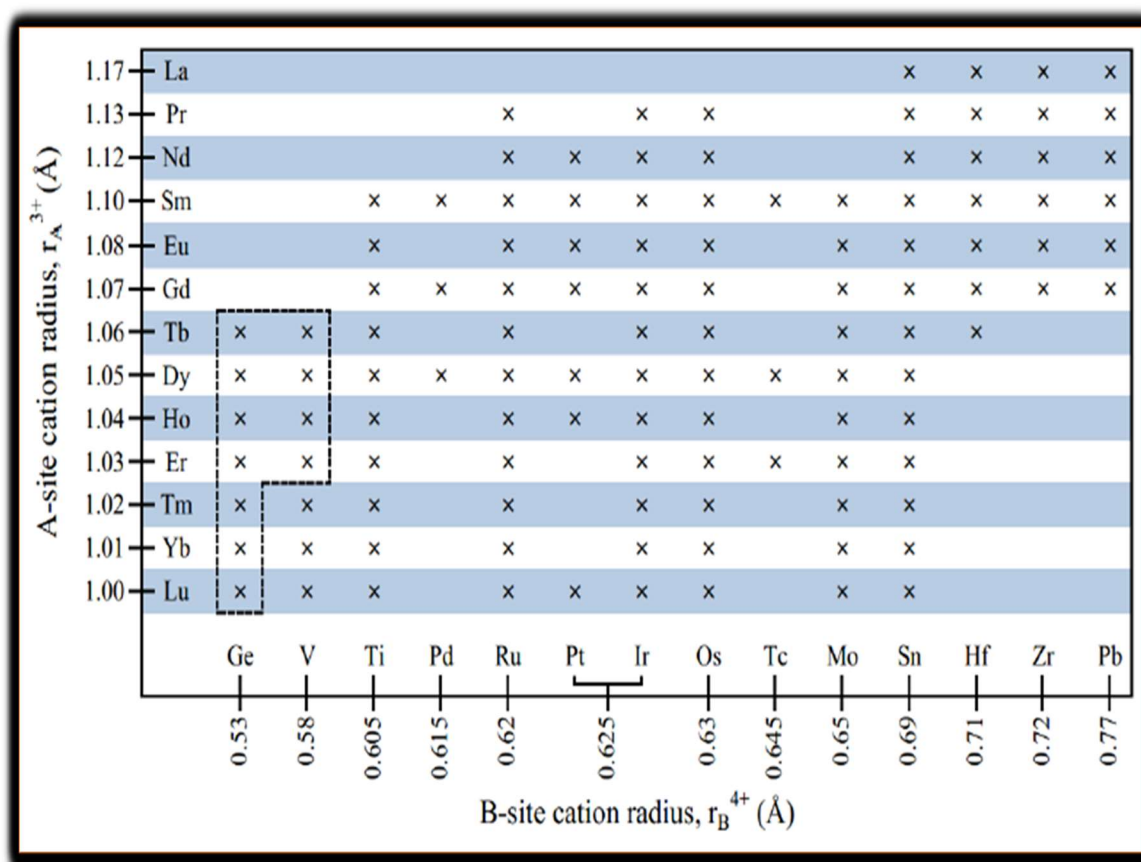


Fig. 1.2 Rare earth pyrochlore oxide stability field.

High-pressure techniques can be used to create pyrochlores with ionic radii ratio values as high as 2.30. Though while many cations groupings that lie instability range occur, some do not form at all. For the study of geometric frustration, the pyrochlore lattice is the suitable structure [16]. High levels of frustration are caused by the A and B positions together arranged as a tetrahedron corner sharing pattern. The huge stability field makes it easier to investigate patterns, such as how changing the cell parameter or magnetic moment affects the system.

Because of these factors, pyrochlore structured ceramics have emerged as spotlight for uncommon and exotic characteristics of magnetization.

1.4 Electron Magnetic Moment

The unpaired valence electron serves as the primary source of magnetism in solids. It is understood by Maxwell's relations that electrically charged body in motion generates a magnetic moment. An atoms nucleus is orbited by a negatively charged electron with angular momentum \mathbf{L} producing a magnetic moment $\boldsymbol{\mu}_L$:

$$\boldsymbol{\mu}_L = - \frac{e}{2m_e} \mathbf{L} \quad (1.1)$$

$$L = \sqrt{l(l+1)} \frac{h}{2\pi} \quad \text{and} \quad l = 0, 1, \dots, n-1 \quad (1.2)$$

As a result of rotating about their axis, Spin S is a second source of angular momentum for electrons. A magnetic moment $\boldsymbol{\mu}_S$ arises from this.

$$\boldsymbol{\mu}_S = - \frac{e}{2m_e} \mathbf{S} \quad (1.3)$$

$$S = \sqrt{s(s+1)} \frac{h}{2\pi} \quad \text{and} \quad s = \frac{1}{2} \quad (1.4)$$

Quantum numbers of two electrons may not be identical, which are n , l , m_l , and m_s , in accordance with the Pauli principle. So, in order for two electrons to be coupled, their orbital spins must be in opposition to one another. Furthermore, as per Hund's rule, an electron can occupy every open orbital in a given subshell before an electron occupying any orbital with two electrons. Due to the cancellation of the magnetic moments of each spin when pairing of all electrons, there will be no net magnetic moment, as can be seen from these two rules. It is important to remember that nuclei also have a spin, which might result in a magnetic moment

that is non-zero. Electron magnetism is 1800 times stronger than nuclear magnetism because of the relatively enormous mass of the proton and in solids, it is normally acceptable.

1.5 Atomic Magnetic Moment

The estimation of atom magnetic moment is made simple with accounting for quantum number (J), known as entire angular momentum of the atoms.

$$J = L \pm S \quad (1.5)$$

$$\text{here } L = \sum m_l \text{ and } S = \sum m_s \quad (1.6)$$

Valence shell is less than half full, J equals the variance among L and S, and when the subshell is more than halfway full, J becomes the total of L and S. In terms of Bohr magnetons μ_B magnetic moment (effective) μ_{eff} for a certain molecule can be computed by:

$$\mu_{eff} = g\sqrt{J(J+1)}\mu_B \quad (1.7)$$

$$\mu_B = \frac{eh}{4\pi m} \quad (1.8)$$

$$g = 1 + \frac{J(J+1)+S(S+1)-L(L+1)}{2J(J+1)} \quad (1.9)$$

Lande g-factor (g) which is a constant of proportionality, connects angular momentum and observable magnetic moment.

1.6 Magnetic Interaction

The propensity for a system to order to rise as temperature decreases are required by thermodynamics 3rd law. As a result, a paramagnetic substance will adopt an ordered spin arrangement as it cools, transitioning into its magnetic ground state. However, it is not simple

to predict the ground state (magnetic) for a specific compound or to interpret an observed magnetic state. A macroscopic material's magnetic behaviour cannot be fully explained by scaling an atom's magnetic behaviour. Rather, interactions between electrons control magnetism in materials. Despite weak interaction among dipoles (magnetic), it is crucial for understanding magnetic behaviour. Following equation provides the dipolar interaction energy (U).

$$U = \frac{\mu_0}{4\pi r_{ij}^3} \left\{ m_i \cdot m_j - \frac{3}{r_{ij}^2} (m_i \cdot r_{ij})(m_j \cdot r_{ij}) \right\} \quad (1.10)$$

Where m_i and m_j are magnetic dipole components and r_{ij} is location vector providing shortest path between two dipoles. The fact that interaction (dipolar) is comparatively feeble but extremely long range is not surprising given that energy of interaction is related to inverse of the dipole - dipole distance $\frac{1}{r_{ij}^3}$.

Classical physics can describe dipolar interactions, but the more important exchange interaction is entirely governed by quantum mechanics. Magnetically ordered substances, like the naturally occurring lodestone, would not exist at room temperature without exchange interaction. The detection of any magnetic ordering would need temperatures of 1 K if dipolar exchange is the major source [17]. Exchange interaction results from the two electron wave functions anti-symmetry when particles are exchanged. On the basis of Pauli's exclusion opinion, two electrons with equal spin don't share same spatial location when there is an antisymmetric wavefunction. This demands that electrons with similar spins be kept apart. Due to this, antiparallel spins exhibit less Coulomb repulsion than parallel spins [18]. Thus, the interaction energy can be provided by:

$$E = -2 J_{ex} (S_i \cdot S_j) \quad (1.11)$$

This illustrates the difference between parallel and antiparallel spins in the $2J_{\text{ex}}$ Coulomb energy E where J_{ex} is the exchange integral:

$$J_{\text{ex}} = \frac{e^2}{4\pi\epsilon_0} \int \psi_A^*(r_i) \psi_B^*(r_j) \left(\frac{1}{r_{AB}} + \frac{1}{r_{ij}} - \frac{1}{r_{Aj}} - \frac{1}{r_{Bi}} \right) \psi_A(r_j) \psi_B(r_i) dr_i dr_j \quad (1.12)$$

Parallel spin alignment is energetically advantageous when J is positive, leading to ferromagnetic orientation (**Fig. 1.3a**). Antiferromagnetic configuration results from antiparallel spin alignment, which is energetically advantageous when J is negative (**Fig. 1.3b**).

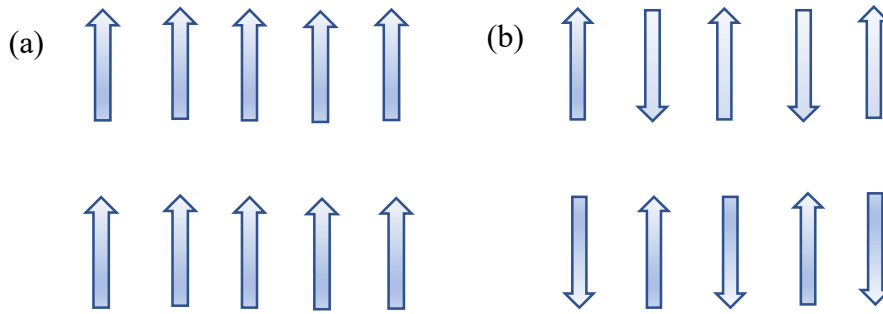


Fig. 1.3 Magnetic moments are arranged in (a) parallel arrangement (FM) and (b) antiparallel arrangement (AFM).

Direct exchange refers to this fundamental exchange communication of two magnetic classes with coinciding orbitals of atom. The categories of exchange regulating a system nevertheless, hinge on components elaborate in their bond angle, and orbital overlaps (denote by Good enough Kanamori guidelines) [19]. Only the appropriate interactions for the items in this work will be discussed further in terms of exchange. The super exchange interaction is typically present in composites covering transition metals that have extremely localized d-orbitals of

atoms. Direct exchange is prevented by absence of overlap among nearby d-orbitals. The exchange can be facilitated by an intermediary oxygen atom though, owing to its p-orbital [20]. The electron of dual oxygen (p orbitals) can each interchange with one of nearby metallic element if electrons are associated in an antiparallel manner (**Fig. 1.4**) P-orbital electrons are all singlet on might assist in exchange if the metal electrons were arranged in a parallel alignment. Thus, having antiferromagnetic alignment is advantageous energetically because it increases exchange. In situations when the bond angle is 180° degree, this super exchange interaction predominates [21]. The fact that ferromagnetic ordering would be more beneficial if the bond angle were 90° instead illustrates the complexities of exchange even further.

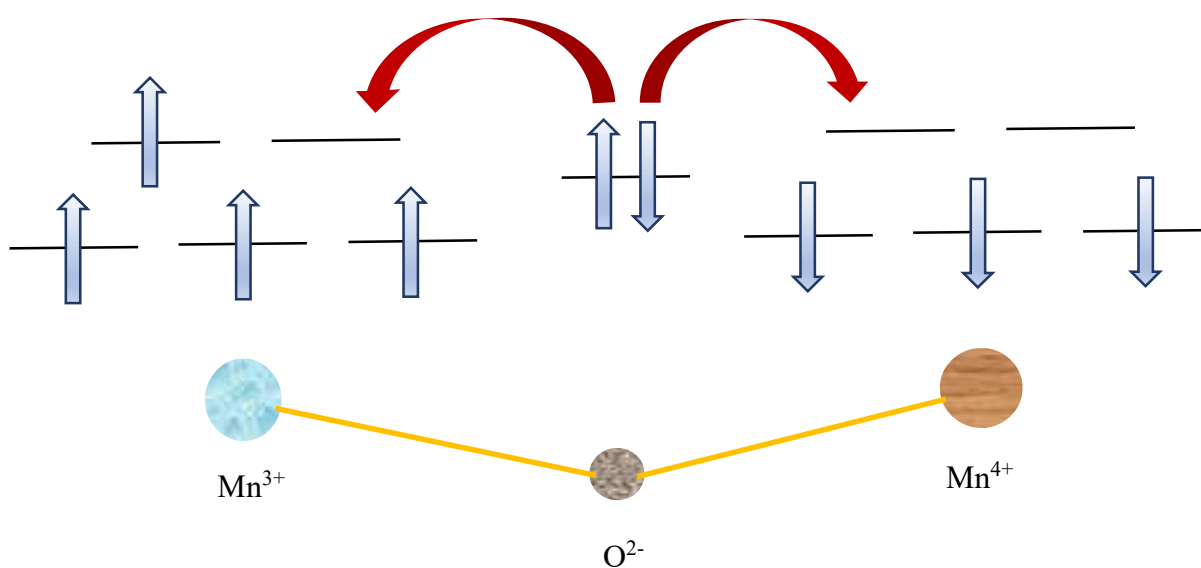


Fig. 1.4 Diagram of Mn^{3+} - O^{2-} - Mn^{4+} super exchange interaction with a 180° bond angle.

In addition to dipolar and exchange connections, temperature also affects a material's capacity to organize. Surprisingly, some ferromagnets, including metallic cobalt, continue to be magnetically ordered at temperatures above 1100° C. However, many magnetic materials are disordered even at room temperature. However, as temperature decreases, energy level of magnetic connection's beats that of entropic mechanisms, leading to impulsive magnetic ordering.

$$\chi = \frac{C}{T - \theta_{CW}} \quad (1.13)$$

The Curie-Weiss constant, abbreviated θ_{CW} can be calculated using mean field theory as total exchange connections over all neighbours [22].

$$\theta_{CW} = \frac{2S(S+1)}{3k_B} \sum_{n=1} z_n J_{ex,n} \quad (1.14)$$

where $J_{ex,n}$ denotes the appropriate exchange interaction and n symbolizes the n^{th} nearest neighbour (z_n neighbours). By providing energy levels for all magnetic connections, the CW constant can be utilized to determine transition temperature [23]. θ_{CW} is referred to be Curie temperature in ferromagnetic ordering scenarios. The Neel temperature (θ_{CW}) is employed to describe antiferromagnetic transitions.

1.7 Geometrical Frustration

In simple ferromagnetic (FM) or antiferromagnetic (AFM) materials, the CW law is a reasonable transition temperature predictor but it is much less reliable in frustrated materials [24]. A high percentage of magnetic sites are typically frustrated when they are subject to opposing or conflicting constraints. In a particular instance, the lattice geometry of the material

causes frustration, which is known as geometric magnetic frustration [25]. Geometric frustration frequently leads to an odd or innovative ground state in addition to impeding ordering. The AFM alignment of spins positioned on symmetrical triangle vertices is the classic illustration of geometric frustration (**Fig. 1.5 a**). When two spins are aligned antiparallel, the 3rd spin is unable to satisfy both of its pairwise interactions by aligning in either direction. If the spins are Ising-like, then only one of the two states of three pair-wise interactions can be met concurrently (up or down). When spin can be somewhere in plane instead (XY), arrangement can use a so-called 120° structure to lower its energy (**Fig. 1.5 b**). Lattices based on the equilateral triangle are frequently found in real materials that display geometric frustration. For instance, many materials, like the Kagome lattice, have 2-dimensional layers made of equilateral triangles that share their corners or edges.

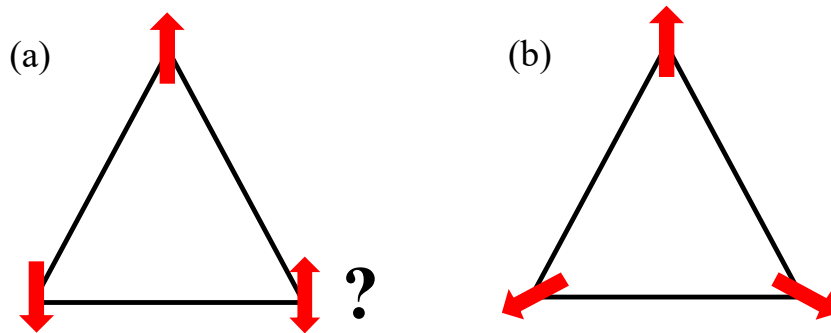


Fig. 1.5 Two-dimensional triangular lattice that is geometrically frustrated has (a) antiferromagnetic and (b) 120° aligned structure.

The dynamics in three dimensions are significantly more complex, which frequently leads to extreme frustration [26]. Many three-dimensional frustrated systems are based on the

tetrahedron, a polyhedron with four sides that are adjoined and equilateral triangles on all four sides (**Fig. 1.6**). About half of pairwise connections can be met when spins occupying a tetrahedron's vertices are aligned antiferromagnetically. Pyrochlore and spinel lattices are examples of actual lattices based on tetrahedral configurations. Systems with geometric frustrated frequently order at temperatures far lower than those expected by the CW law. A system degree of frustration can be determined using dividing the CW temperature (θ_{CW}) by Neel temperature (T_N).

$$f = \frac{\theta_{CW}}{T_N} \quad (1.15)$$

When a materials frustration index f is higher than 10 it can be said to be frustrated. This threshold is rather arbitrary because in the situation of an exceedingly frustrated compounds, index of frustration will turn low when θ_{CW} is negligible, especially in the occurrence of numerous interaction types [24].

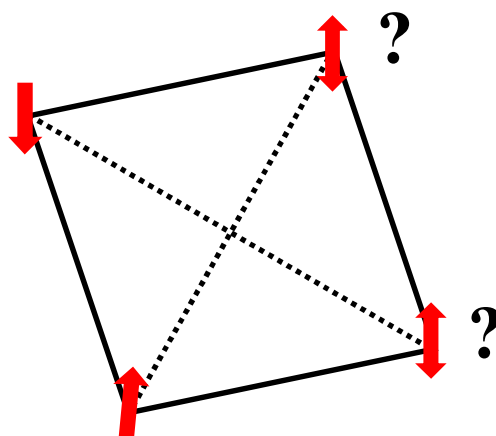


Fig. 1.6 Spins aligned antiferromagnetically on a tetrahedron's vertices cause geometric frustration.

Owing to the unusual ground states that many of these compounds assume highly frustrated materials have long captivated scientists. Since such systems are unable to simultaneously lessen all of their pairwise connections an active trade-off is necessary which frequently leads to an unusual ground state [27]. Numerous compounds, in particular, those with three dimensional lattices are incapable of achieving ordered long range and instead advocate for ordered short range ground state. Spins with ordered long range, such as simple ferromagnetism and antiferromagnetism are correlated over any distance within magnetic domains. Conversely, short-range order is limited to ordering between spins that are close to one another but spins that are more spaced out will have an uncorrelated arrangement. Because no distinct long range magnetic ordering can form in short range (ordered) states, there is frequently a significant degeneracy of ground state. These highly degenerate states have been generally referred to as cooperating paramagnets to represent their dynamic nature [28]. Pair spins into singlets in $S=1/2$ in Anderson quantum spin liquid, which is dynamic at the temperature limit of 0 K, is a well-known example of cooperative paramagnetism [29]. Spin glassy phase where changeable spins freeze out in arbitrary angles to cause stationary disorder is another ground state seen in frustrated materials.

1.8 Spin Ice Phase

One of the most extensively researched pyrochlore ground states is spin ice phase, which is only found in pyrochlores (magnetic) and is extremely occasional [4]. Named after behaviour that is similar to that of water ice, this short range ordered ground state. In same way as two chemical bonds and two hydrogen bonds formed by four tetrahedron organised hydrogen around individually oxygen each tetrahedron's spins are ordered in a two in two out pattern

(Fig. 1.7). A powerful electric field of crystal acting on magnetic particles in spin ices produces a nearly faultless Ising spin. Quantization axis is in the direction of the quantization due to the pyrochlore's cubic regularity. Thus, only spins that are directed inside toward the tetrahedron centre or outward are permitted resulting in the two in two out configurations also known as the ice law.

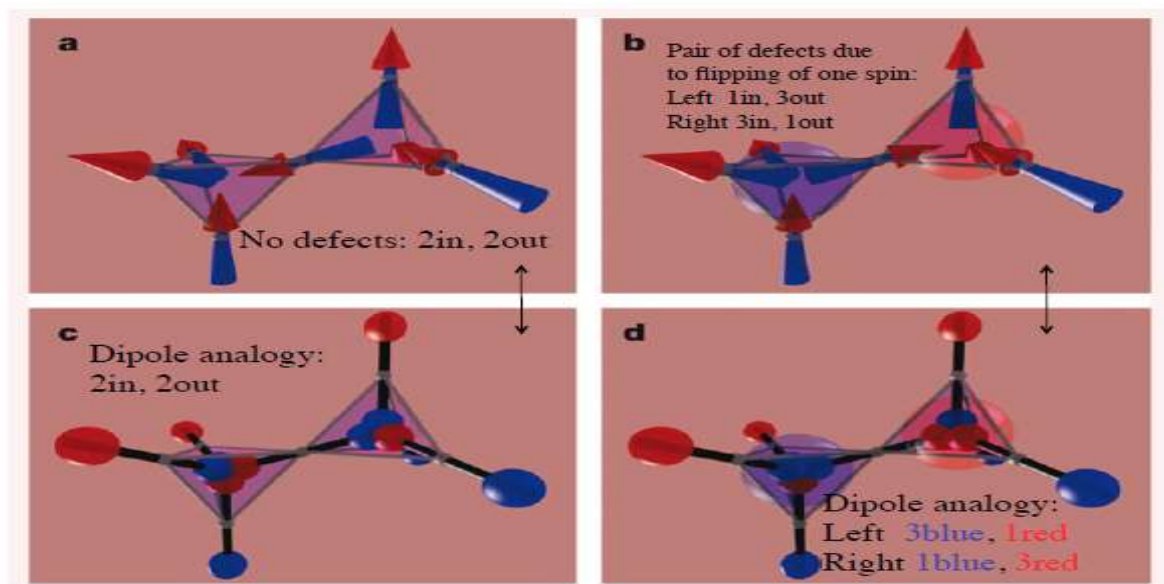


Fig. 1.7 Spin configuration in the pyrochlore oxide with a two in two out ordering.

The large ground state degeneracy is another resemblance among water and spin ice. Macroscopic number of tetrahedra can be arranged in a two in two out configuration in an almost unlimited number of ways. Six of the sixteen possible spin configurations on individual tetrahedrons obey the ice law [30]. Meanwhile, two tetrahedra share each spin, tetrahedra are not genuinely independent and as a result, there are only four potential states for each tetrahedron. It is evident that ground state (non-degenerate) has zero residual entropy (S) and W is the total number of ways using a statistical mechanics approach.

$$S = k_B \log W \quad (1.16)$$

The multiplicity is as follows for spin ice with N spins and $\frac{N}{2}$ tetrahedra, where $\frac{6}{16}$ of the four possible states per tetrahedron meet the ordering with two in two out.

$$W = \left[4 \left(\frac{6}{16} \right) \right]^{\frac{N}{2}} = \left(\frac{3}{2} \right)^{\frac{N}{2}} \quad (1.17)$$

The residual entropy that results match Pauling's original prediction for water ice [31].

$$S = \frac{Nk_B}{2} \log \frac{3}{2} \quad (1.18)$$

A very specific set of criteria must be satisfied for spin ice phase to exist. Spin ice phase is an unusual instance of frustrated ferromagnetism, even though geometric frustration is typically linked with anti-ferromagnetism. In spin ice phases, there exist net FM interactions among magnetic particles, which makes it necessary for dipolar (D_{nn}) and exchange interaction (J_{nn}) to be of equal gauge. The ordinarily weak dipolar interactions must be on a par in size through exchange interaction, which requires either very huge magnetic moment or an extremely weak exchange. Traditional spin ices, such as holmium or dysprosium, only develop when the greatest moments of a periodic element occupy the A-site. Furthermore, the B-site cation's atomic radius must be sufficiently small to constrain the lattice parameters size since dipolar interactions scale with $\frac{1}{r_{ij}^3}$. The criteria under which the spin ice state as depicted in **Fig. 1.8** is stable are given by Ising phase diagram published by Gingras and den Hertog [32].

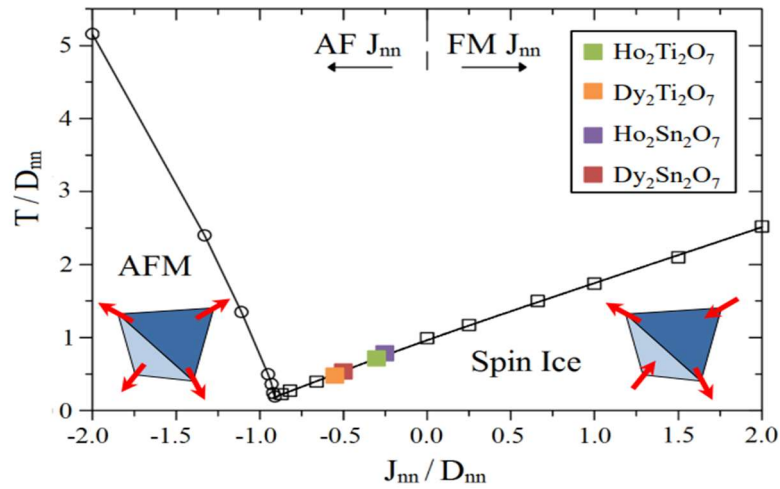


Fig. 1.8 Pyrochlore phase diagram of Ising spin. The spin ice phase is constant above $\frac{J_{nn}}{D_{nn}} \sim -0.91$. It is anticipated that an all-out antiferromagnetic phase will occur below the critical point. The curve has markers for the recognized spin ices [32] (Reprinted with the permission © American Physical Society).

The exchange interaction is on the border of being ferromagnetic while the nearest neighbour dipole interaction is antiferromagnetic. Though ferromagnetic exchange might theoretically also lead to the spin ice state, all known spin ices contain antiferromagnetic exchange. When the J_{nn}/D_{nn} ratio is higher than -0.91, then the spin ice phase forms. Net antiferromagnetic interactions occur when J_{nn}/D_{nn} is smaller than -0.91. This results in an all-in, all-out spin configuration when paired with the $\langle 111 \rangle$ Ising anisotropy. This antiferromagnetic state would not be frustrated, which is contrary to the usual and has not been experimentally realized.

$\text{Ho}_2\text{Ti}_2\text{O}_7$, the first known example of a spin ice phase was found in 1997 by Harris *et al.* [33]. Only a few more spin ice materials have been discovered since then because of the stringent conditions mentioned above: $\text{Dy}_2\text{Ti}_2\text{O}_7$ in 1999 [34], $\text{Dy}_2\text{Sn}_2\text{O}_7$ in 2002 [35], and $\text{Ho}_2\text{Sn}_2\text{O}_7$ in

2002 [36]. The characteristics of these four compounds' have numerous similarities such as (a) both holmium and dysprosium can occupy the A-site and their moments of $10.4 \mu_B$ and $10.6 \mu_B$ respectively, produce very strong ferromagnetic dipolar interactions, (b) J_{nn}/D_{nn} values range from -0.26 to -0.49 as a result of antiferromagnetic exchange interactions (**Fig. 1.8**), (c) long range order is missing temperature lower to 50 mK and (d) defining the residual entropy (Pauling).

More focus has been placed on spin ices as homes of quasiparticles that mimic monopoles (magnetic). A single ion with a non-zero magnetic moment is entitled monopole. It is magnetic analogue of proton and the electron the two fundamental charge-carrying particles. But Maxwell's equations strictly forbid the existence of monopoles. Thermal changes in spin ice can cause individual spins to flip. The two in two out configurations of one tetrahedron are disrupted as a result. A neighbouring spin will flip to fulfil the ice laws, amplifying the defect and resulting in creation of so-called Dirac string [37]. The magnetic moments on either end are detached by string of overturned spins. In reality, magnetic moments are single tetrahedra with spin configurations of three in, one out, or one in, three out. To examine the theoretical concept of magnetic monopoles, these excitations have given researchers a useful tool [38-39].

1.9 Spin Glassy Phase

A phase in which magnetic spin of its constituent atoms nearly equals the probability value of either FM or AFM interactions, making it the magnetically disordered analogy of regular glass with positional disorder known as the glassy phase. The glassy state has no challenging order phase in contrast to regular glass, which needs to cool fast to avoid the crystalline phase. If there is no thermodynamic phase transition, the low temperature stage would justly be an optimal condensed disorder phase, novel stage of matter. The word "glass" emerges from a

similarity between the positional chaos of a conservative, chemical glass and the magnetic disturbance in a spin glass. In amorphous material, the microscopic bond structure is extremely unstable, in contrary to a crystal, where atomic bonds are arranged uniformly. As with a crystal's-based structure, magnetic spins in ferromagnetic materials all line up in the similar direction. In spin-glass, occurrence of traditional long-range ordering, represented by delta function is suppressed by the interaction of randomness and frustration [40]. The author Taira *et al.* reported spin glassy behavior in $Y_2Ir_2O_7$ and $Lu_2Ir_2O_7$ pyrochlore. The magnetic conversion has been detected by nearly 150K and 120K for $Y_2Ir_2O_7$ and $Lu_2Ir_2O_7$ correspondingly [41]. Below this conversion temperature found a huge variance among FC and ZFC magnetic susceptibilities (**Fig. 1.9**). Since the Y^{3+} and Lu^{3+} ions in the specimens are both diamagnetic, this magnetic behavior has been attributed to the Ir^{4+} ions.

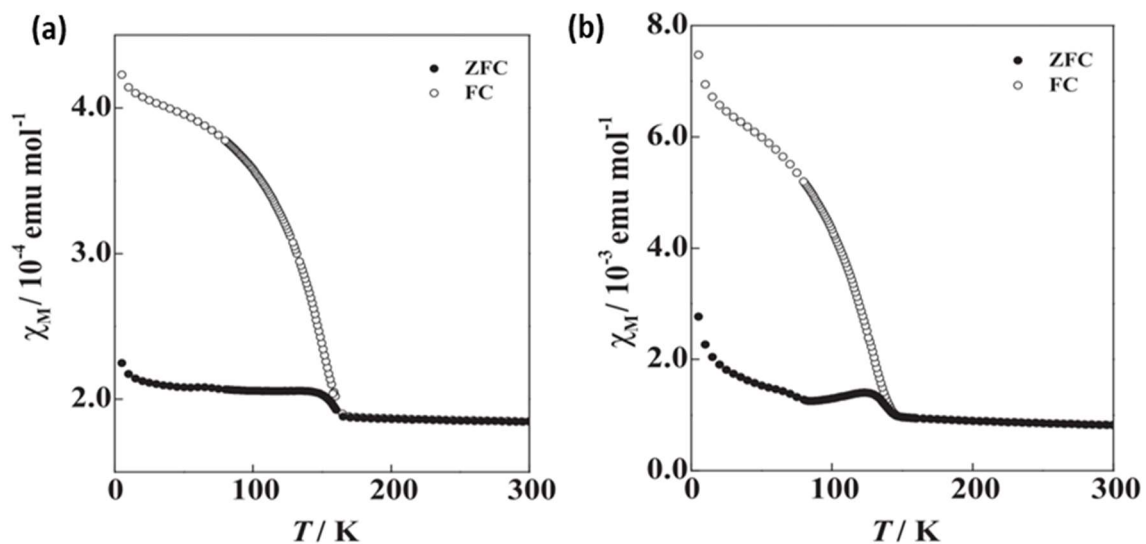


Fig. 1.9 Spin glassy behavior of (a) $Y_2Ir_2O_7$ and (b) $Lu_2Ir_2O_7$ pyrochlore [41] (Reprinted with the permission © Institute of Physics).

Hui Liu *et al.* also published spin glassy outcomes for $Y_2Ir_{2-x}Fe_xO_7$ pyrochlores such data is presented in **Fig. 1.10**. The magnetic transition seemed at 150 K for the parent compound [42]. A magnetic transition occurred due to B site Ir ions. It was found conversion temperatures increases owing to the enlarged substituting of Fe ions. The frustration index depends upon the inversion temperature. It was detected that frustration levels weakened with a rising concentration of B site elements. Also contributing to the frustration in the compound are Curie Weiss and inversion temperature.

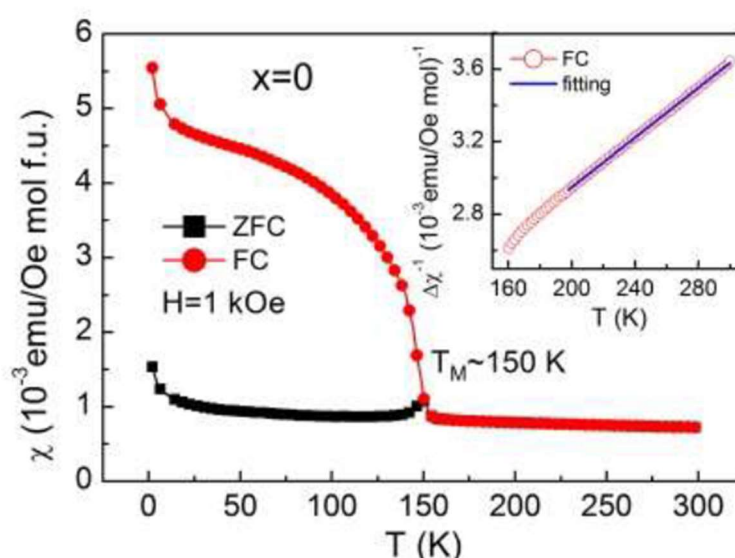


Fig. 1.10 Spin glassy behavior of $Y_2Ir_{2-x}Fe_xO_7$ pyrochlore [42] (Reprinted with the permission © Elsevier).

1.10 Literature Review

In terms of physical characteristics, the magnetic assets of pyrochlore have received the most attention; geometrical spin frustration has a direct impact on these characteristics. Pyrochlore structured ceramics have involved highly devotion as of geometric frustration on the system of corner sharing tetrahedron in materials. Owing to innovative and striking magnetic ground

states, such as spin liquid, spin glass, and spin ice, geometrical frustration of spin-spin interaction has generated renewed study interest in recent years [30, 43]. An amusing spectrum of magnetic behaviour's has been detected in rare-earth pyrochlores. Like, $\text{Ho}_2\text{Ti}_2\text{O}_7$ displays spin ice phase (classical) and monopole excitations created from Ising anisotropy and operative FM spin communications [33, 44]. Amongst the entrants for quantum spin ice, Nd holding pyrochlores are relatively different owing to the unusual regularity of dipolar interaction in Nd^{3+} atoms [45]. There are numerous instances of rare earth pyrochlores incoming ordered (long range) states as a result of single ion anisotropy, spin-spin coupling, and neighbour interchange connections. Samples of such pyrochlore include $\text{Gd}_2\text{Ti}_2\text{O}_7$ and $\text{Gd}_2\text{Sn}_2\text{O}_7$. The susceptibilities of the two pyrochlores obey the Curie Weiss law, with effective moments comparable to hypothetical results of $7.94 \mu_B$ for free ions and $\theta_{CW} \sim -10$ K for the Weiss temperatures, and magnetically ordered phase at 1K [46-47]. The Kramer doublet with effective moments (0.12 and $3.8 \mu_B$) parallel and perpendicular to axis and a significant temperature of $\theta_{CW} \sim -22$ K was studied by Champion *et al.* [48] in crystal field ground state of $\text{Er}_2\text{Ti}_2\text{O}_7$. The large frustration parameter was found 18.7 in $\text{Er}_2\text{Ti}_2\text{O}_7$ such data published by Gardner *et al.* [4]. They also investigated magnetic properties of the magnesium pyrochlores $\text{Ho}_2\text{Mn}_2\text{O}_7$ and $\text{Yb}_2\text{Mn}_2\text{O}_7$ [49]. Both exhibit positive CW temperatures, which demonstrates a ferromagnetic instead of a ferrimagnetic correlation among the two surfaces. Ruthenates pyrochlore ($\text{Y}_2\text{Ru}_2\text{O}_7$ and $\text{Lu}_2\text{Ru}_2\text{O}_7$) provide indication of magnetic behavior of the Ru^{4+} ions and specify a magnetic conversion at ~ 75 K, leading to lot of frustration level ~ 17 [50].

Hantean *et al.* described the temperature dependency of susceptibility displays no magnetic alignment at low temperatures [51]. The data has been fitted using Curie-Weiss law and interpretation a ferromagnetism interaction between the Nd atoms. Magnetization against field

diagram displays Ising anisotropy lengthways (111) battle-axes of Nd particles in lowest level. Specific heat data against temperature dependence without field specify occurrence of a thermal irregularity under 7 K, but no indication of order is detected at temperature lower to 0.5 K. Pramod *et al.* reported that effect of B site Fe doped with varied composition (0 - 0.15) in $\text{Ho}_2\text{Ti}_2\text{O}_7$ at low temperature [52]. To additionally approve this spin edge of iron Fe^{3+} , they estimated the magnetization as against magnetic field at 5 K in the field series beginning 0 to 10 Tesla for $\text{Ho}_2\text{Ti}_{2-x}\text{Fe}_x\text{O}_7$. It was originated that excluding the composite ($x = 0.15$), there is no substantial modification in M-H curve, whereas in the sample ($x = 0.15$), a reduction in the coercivity happens. Thus, reduction in coercivity could rise antiferro-magnetic collaboration between holmium and iron atoms. The magnetic investigation more approves that up to ($x = 0.1$) utmost of Fe^{3+} ion is existing in high (spin) state, however for x is greater than 0.1, the iron ion is existing in low (spin) state.

Shukla *et al.* examined the role of chemical pressure on the magnetic pyrochlore oxide $\text{Ho}_2\text{Ti}_2\text{O}_7$ [53]. They varied the B site composition by substituting titanium with germanium. Impact of pressure on spin forces at work of $\text{Ho}_2\text{Ti}_2\text{Ge}_{2-x}\text{O}_7$ has been analysed through the learning of static magnetization contrary to magnetization against magnetic field (M-H). Magnetic study specifies that the tender of enlarged pressure in $\text{Ho}_2\text{Ti}_2\text{O}_7$ matrix pushes the system to reduced ferro-magnetic communication. Coupling constant (Dipolar) remnants are nearly unaffected but temperature θ decreases to -0.03 K as of 0.32 K by increasing x in $\text{Ho}_2\text{Ge}_x\text{Ti}_{2-x}\text{O}_7$. Positive pressure launches the domination of holmium antiferro interaction over dipolar correlation. Singh *et al.* observed the high spin-freezing temperature shift in pyrochlore $\text{Eu}_2\text{Ti}_2\text{O}_7$ [54]. Further the magnetization (AC and DC) of pyrochlore $\text{Eu}_2\text{Ti}_2\text{O}_7$ have been examined. To approve the transition of spin freezing, the outcome of dilution of non-magnetic structure is inspected. They changed the Eu^{3+} particles with nonmagnetic Y^{3+} particles to transform limited

atmosphere of europium ions efficiently. From now, this dilution of non-magnetic reasons rises in operative detachment between Eu ions thus letting down the limited spin connections. It is noticeable that if detected freezing temperature (35 K) involves spin connection, then dilution of nonmagnetic must overturn the spin. Temperature difference of susceptibility for $\text{Eu}_2\text{Ti}_2\text{O}_7$ for changed frequencies is shown in **Fig. 1.11**. On the basis of the literature, it is clear that 35 K is the maximum freeze temperature, but earlier reported value is 16 K in $\text{Dy}_2\text{Ti}_2\text{O}_7$ [4, 55]. The source of freezing was accredited basically to an only ion development which is connected to europium spin slackening. Nonmagnetic doping by Y^{3+} atoms also approve single phasic freeze.

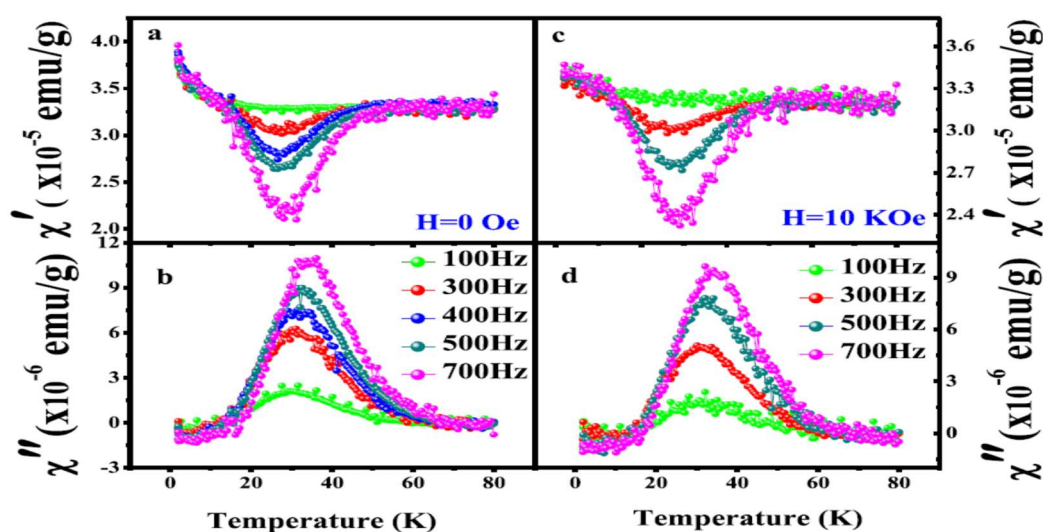


Fig. 1.11 Temperature disparity of susceptibility (AC) at field of 0 K Oe (a & b) and 10 K Oe for $\text{Eu}_2\text{Ti}_2\text{O}_7$ for frequencies changed (c & d) [54] (Reprinted with the permission © Elsevier).

The ability to see the complexity of the magnetic correlation and the spin relaxation system through dilution dependency makes it a crucial tool for probing this system [56]. Most dilution compounds have magnetic ions that are swapped out for smaller non-magnetic ones like La,

Lu and Y. Raman, dc and ac susceptibility measurements were used by Liu *et al.* to examine the physical characteristics of the doped spin ice $\text{Dy}_{2-x}\text{La}_x\text{Ti}_2\text{O}_7$ [57]. It was discovered that nonmagnetic (La^{3+}) substitution weakens the ferromagnetic connection and causes the spin ice phase to disappear. It is demonstrated that in the diluted system (DLTO), a circulation of relaxation time and hastening of spin dynamics arise towards 16 K. $\text{Dy}_2\text{Ti}_{2-x}\text{V}_x\text{O}_7$ single crystals from the spin-frustrated compound were the subject of a study by Liu *et al.* [58]. According to statistics on bulk magnetization, the ferromagnetic connections among Dy^{3+} and V^{4+} elements lead to an increase in ferromagnetic interaction as V^{4+} content rises. The desertion of spin ice and emergence of a spin glassy conversion would result from greater disorder on the B site and inner field allied with V^{4+} atoms when the doped concentration rises to 0.5. This would also alter the degeneracy of ground state and release the frustration. $\text{Dy}_{2-x}\text{Yb}_x\text{Ti}_2\text{O}_7$ spin frustrated magnet has been investigated for their magnetic order and dynamical characteristics using dc and ac measurements [59]. The reported spin freezing temperature (T_f) is observed less than 3 K. The spin freezing temperature was found to alter due to an increase in concentration of Yb ions. The changed crystalline electric field and spin interactions of Dy^{3+} and Yb^{3+} dominate the $\text{Dy}_{2-x}\text{Yb}_x\text{Ti}_2\text{O}_7$ low-temperature dynamical behavior. Secondly, crystal field-phonon coupling could influence spin dynamics. Marques *et al.* [60] reported Curie temperatures -11.7 K and +1.12 K for $\text{Gd}_2\text{Ru}_2\text{O}_7$ and $\text{Ho}_2\text{Ru}_2\text{O}_7$ correspondingly. It was also publicized that Ho^{3+} substitution change the magnetic ordering from antiferromagnet to ferromagnet.

In contrast to the FM spin phase, the spin liquid state is disordered. In comparison to other muddled states, spin liquid (quantum) maintains its disorder down to lower temperatures. $\text{Tb}_2\text{Ti}_2\text{O}_7$, $\text{Yb}_2\text{Ti}_2\text{O}_7$, and $\text{Pr}_2\text{Ir}_2\text{O}_7$ are the only rare earth pyrochlore compounds that have been

found as spin liquids. As per Gingras *et al.* [61] the Curie Weiss accurately defines the temperature-dependent magnetic susceptibility of $Tb_2Ti_2O_7$ down to 50 K with a θ_{CW} of -19 K and a moment (effective) of $9.6 \mu_B/Tb$ ions. The first excited and ground state are both doublets, through two singlets at significantly higher energies, according to crystal field simulation of measured specific heat and susceptibility (dc). Machida *et al.* researched at whether $Pr_2Ir_2O_7$ in metallic materials maintains its paramagnetic properties at 0.3 K [62]. The ground state of $Pr_2Ir_2O_7$ is isolated doublet by an Ising moment along the limited axis, according to investigations on the specific heat, and neutron scattering of compound. There was no evidence of freezing in antiferromagnetically coupled spin, which has an energy of 20 K [63-64]. Although there is a spin (liquid phase) in Pr moment, no investigations of dynamics (spin) have yet been published. At the Curie temperatures of 7.5 K and 7.6 K for Ho_2TiMnO_7 and Dy_2TiMnO_7 , respectively, Zhang *et al.* observed a reversible magnetocaloric effect near the second order ferro-para phase transition (Fm-Pm) [65]. With the functional magnetic field of 0–7 tesla, the maximum magnetic entropy changes for Dy_2TiMnO_7 and Ho_2TiMnO_7 were measured to be 12.52 and 13.94 Jule/Kg K, accordingly. Morosan *et al.* reported on the anisotropic magnetic characteristics of $Ho_2Ge_2O_7$ derived from dc and ac magnetization [66]. They didn't find any indication of intense frustration in magnetization, but the susceptibility (ac) suggests two potential processes for spin relaxation that are comparable to those seen in $Ho_2Ti_2O_7$ [67]. Singh *et al.* investigated the spin freezing effect and field induced transition in $Tb_{2-x}Eu_xTi_2O_7$ ceramics [68]. Dc magnetic studies show a substantial role for exchange and dipolar interactions in samples rich in Eu. According to ac measurements, the $Tb_{2-x}Eu_xTi_2O_7$ compound exhibits partial single ion spin freezing at a temperature of 33 K with no magnetic field. All specimens exhibit a field tempted transition that swings to higher temperatures by rise in Eu concentration when a field of 10 KOe is applied.

1.11 Motivation and Scope of Work

- ❖ Rare earth titanates ($\text{RE}_2\text{Ti}_2\text{O}_7$) one of the most researched quantum materials exhibit unusual magnetic properties (low-temperature) including spin ice ($\text{RE} = \text{Ho}, \text{Dy}$), spin liquid ($\text{RE} = \text{Tb}$), and anti-ferromagnetic ordering ($\text{RE} = \text{Er}, \text{Gd}$). Due to their large magnetic moments $\text{Ho}_2\text{Ti}_2\text{O}_7$ and $\text{Dy}_2\text{Ti}_2\text{O}_7$ are excellent candidates for magnetic investigation. It is very fascinating to compare outcomes of both A and B site substitution in terms of controlling the magnetic properties.
- ❖ Electronic structures of $\text{Ho}_2\text{Ti}_2\text{O}_7$ and $\text{Ho}_2\text{Ge}_2\text{O}_7$ pyrochlore have already been studied in detail. However, $\text{Ho}_2\text{Ge}_x\text{Ti}_{2-x}\text{O}_7$ lacks information about how chemical pressure affects the structural and magnetic characteristics. The investigation of the influence of chemical pressure on the pyrochlore's magnetic characteristics is terribly challenging.
- ❖ Exotic magnetic features were observed to originate from single ion anisotropy in coupled with exchange and dipolar interactions. The probing of this thorough AC and DC magnetic investigation is what inspires me to do my research. Furthermore, these materials have also been considered for their probable use as solid catalysts, electrolytes and faraday rotators.
- ❖ An interesting area of research to explore the magnetic monopole similarity is the quest for novel spin ice with significant monopole density at low temperatures. Understanding the degeneracy of ground state of spin ice at low temperatures is incredibly fascinating that can be investigated by local defect/distortion caused by doping and to regulate the spin dynamics by switching the A and B site.
- ❖ Ionic radii ratio of pyro titanates ($\text{Gd}_2\text{Ti}_2\text{O}_7$, $\text{Ho}_2\text{Ti}_2\text{O}_7$ and $\text{Dy}_2\text{Ti}_2\text{O}_7$) lies in the range of $1.46 \leq \text{RR} \leq 1.78$ which shows the stable pyrochlore structure is formed. Because of this, one take into account these materials for magnetic and structural research. It has

been well recognized that magnetic and dipolar bonding among the adjacent neighbouring spins adopts the low T magnetic behaviour.

1.12 Objectives of the Thesis

The objectives of the thesis are as follows:

- ❖ Understanding the phenomenon of geometrical frustration in pyrochlore structured ceramic at low temperatures. Study the chemical pressure role on magnetic and structural characteristics of pyrochlore.
- ❖ To control spin dynamics by substitution at the A & B site and understand the local defect/distortion generated by doping of nonmagnetic and magnetic elements.
- ❖ Understand the role of chemical pressure on spin ice freezing. To evaluate the spin ice magnetic monopole analogue at low temperatures further and measure DC magnetic features when A site of $\text{Ho}_2\text{Ti}_2\text{O}_7$ ceramics is diluted by nonmagnetic (La^{3+}) ion.
- ❖ Compare the outcomes of both A and B site substitution in terms of regulating the magnetic properties.

1.13 Arrangement of Thesis

The current thesis is arranged as follows to address the aforementioned scope:

Chapter 1: This chapter briefly describes the background of magnetism in pyrochlore-structured ceramics. The basic concepts underlying magnetic interactions in spin systems and role played by the magnetic systems in frustration are discussed. Earlier findings pertaining to low-temperature magnetic phases of pyrochlore compounds that share the same rare earth in $\text{R}_2\text{Ti}_2\text{O}_7$ as the compounds examined in this work is also explained. Motivation, scope of proposed research work and objectives of the thesis are also included in this chapter.

Chapter 2: This chapter emphasizes physical operations and phenomena concerning the experiments employed in this work. It explains the standard solid state method used in the preparation of single phase polycrystalline samples. This chapter also described several advanced materials characterization techniques such as X-ray diffraction (XRD), scanning electron microscopy (SEM), Raman spectroscopy, and PPMS used to probe the structural, micro-structural and magnetic properties of the pyrochlore structured ceramics.

Chapter 3: This chapter mainly attention to the correlation of structural and magnetic properties of frustrated $\text{Ho}_2\text{Ti}_{2-x}\text{Ge}_x\text{O}_7$ ($x = 0.0, 0.4, \text{ and } 0.8$) compounds by partial doping Ge by Ti (B-site). The excellent spin-ice features and conspicuous quantum character of holmium titanates ($\text{Ho}_2\text{Ti}_2\text{O}_7$) are widely known. X-ray diffraction along with Raman spectroscopic investigations confirmed the formation of the cubic pyrochlore structure with cell parameters varying linearly and follow Vegard's rule. Raman spectroscopy studies also exhibited a blue shift and hardening of phonon mode due to anharmonic interaction. Low-temperature magnetic experiments have shown that the ferromagnetic connection is lessening because the chemical pressure in $\text{Ho}_2\text{Ti}_2\text{O}_7$ is increasing. No spin glassy conversion was traced at any temperature.

Chapter 4: This chapter explores the La^{3+} substitution effect on structural and magnetic behavior of spin ice $\text{Ho}_{2-x}\text{La}_x\text{Ti}_2\text{O}_7$ ($x = 0.0, 0.1, \text{ and } 0.2$) pyrochlore. It also describes how A-site nonmagnetic doping affected the structural and magnetic results. The recognized quantum material $\text{Ho}_2\text{Ti}_2\text{O}_7$, which demonstrates coupled structural and magnetic properties, can be identified by its peculiar spin freeze state. It was observed that values of effective magnetic moment (μ_{eff}) and CW temperature (θ_{CW}) lessening with rising La^{3+} amounts lead to weakening of ferromagnetic (FM) nature of the materials. In terms of regulating the magnetism, it was discovered that B site doping is more effective than A site.

Chapter 5: This chapter analyses the probing the influence of Ho^{3+} substitution at A-site on structural and magnetic properties of $(\text{Gd}_{1-y}\text{Ho}_y)_2\text{Ti}_2\text{O}_7$ ($y = 0.0, 0.2, 0.4,$ and 0.6) ceramics. Magnetic studies have demonstrated the system becomes less antiferromagnetic (AFM) character as a result of the increased chemical pressure in $\text{Gd}_2\text{Ti}_2\text{O}_7$. Antiferromagnetically (AFM) linked Heisenberg spins are predicted to be extremely frustrating in the $\text{Gd}_2\text{Ti}_2\text{O}_7$ pyrochlore lattice because there are numerous ways to minimize the exchange energy. Moreover, a larger increment in θ_{CW} was observed with a similar amount of doping linked to the earlier studies. This might be brought on by the Gd-Ho cation's strong crystal field splitting.

Chapter 6: The most significant findings of this thesis are summarised in the conclusion section, where we will also include the research on potential future directions of the existing work. The two main ideas of my work magnetism and geometric frustration are summarized in this chapter.

References:

1. Harris, Mark J., S. T. Bramwell, D. F. McMorrow, T. H. Zeiske, and K. W. Godfrey. "Geometrical frustration in the ferromagnetic pyrochlore $\text{Ho}_2\text{Ti}_2\text{O}_7$." *Physical Review Letters* 79, no. 13 (1997): 2554.
2. Morris, David Jonathan Pryce, D. A. Tennant, S. A. Grigera, B. Klemke, C. Castelnovo, R. Moessner, C. Czternasty et al. "Dirac strings and magnetic monopoles in the spin ice $\text{Dy}_2\text{Ti}_2\text{O}_7$." *Science* 326, no. 5951 (2009): 411-414.
3. Subramanian, M. A., G. Aravamudan, and GV Subba Rao. "Oxide pyrochlores—a review." *Progress in Solid State Chemistry* 15, no. 2 (1983): 55-143.
4. Gardner, Jason S., Michel JP Gingras, and John E. Greedan. "Magnetic pyrochlore oxides." *Reviews of Modern Physics* 82, no. 1 (2010): 53.
5. Shlyakhtina, A. V., and L. G. Shcherbakova. "New solid electrolytes of the pyrochlore family." *Russian Journal of Electrochemistry* 48, no. 1 (2012): 1-25.
6. Sharma, Saurabh Kumar, V. Grover, A. K. Tyagi, D. K. Avasthi, U. B. Singh, and P. K. Kulriya. "Probing the temperature effects in the radiation stability of $\text{Nd}_2\text{Zr}_2\text{O}_7$ pyrochlore under swift ion irradiation." *Materialia* 6 (2019): 100317.
7. Sharma, S. K., V. Grover, R. Shukla, A. Hussain, A. Mishra, R. C. Meena, and P. K. Kulriya. "Evidence of improved tolerance to electronic excitation in nanostructured $\text{Nd}_2\text{Zr}_2\text{O}_7$." *Journal of Applied Physics* 129, no. 11 (2021): 115902.
8. Kumar, A., P. K. Kulriya, S. K. Sharma, V. Grover, A. K. Tyagi, and V. K. Shukla. "Structural and compositional effects on the electronic excitation induced phase transformations in $\text{Gd}_2\text{Ti}_{2-y}\text{Zr}_y\text{O}_7$ pyrochlore." *Journal of Nuclear Materials* 539 (2020): 152278.

9. Kumari, Renu, P. K. Kulriya, V. Grover, R. Shukla, K. Saravanan, S. Mohapatra, A. K. Tyagi, and D. K. Avasthi. "Radiation stability of Gd₂Zr₂O₇: effect of stoichiometry and structure." *Ceramics International* 42, no. 1 (2016): 103-109.
10. Chang, L. J., W. Schweika, Y-J. Kao, Y. Z. Chou, J. Perbon, Th Brückel, Hong-Chang Yang, Y. Y. Chen, and J. S. Gardner. "Magnetic correlations in Ho_xTb_{2-x}Ti₂O₇." *Physical Review B* 83, no. 14 (2011): 144413.
11. Glerup, Marianne, Ole Faurskov Nielsen, and Finn Willy Poulsen. "The structural transformation from the pyrochlore structure, A₂B₂O₇, to the fluorite structure, AO₂, studied by Raman spectroscopy and defect chemistry modeling." *Journal of Solid-State Chemistry* 160, no. 1 (2001): 25-32.
12. Shukla, Manjari, Soma Banik, Rajan K. Pandey, and Chandan Upadhyay. "Role of chemical pressure on optical and electronic structure of Ho₂Ge_xTi_{2-x}O₇." *Journal of Physics: Condensed Matter* 32, no. 11 (2019): 115501.
13. Panghal, Asha, Yogendra Kumar, P. K. Kulriya, Parasharam M. Shirage, and N. L. Singh. "Structural assessment and irradiation response of La₂Zr₂O₇ pyrochlore: impact of irradiation temperature and ion fluence." *Journal of Alloys and Compounds* 862 (2021): 158556.
14. Panghal, Asha, Pawan K. Kulriya, Yogendra Kumar, Fouran Singh, and N. L. Singh. "Investigations of atomic disorder and grain growth kinetics in polycrystalline La₂Zr₂O₇." *Applied Physics A* 125, no. 6 (2019): 1-11.
15. Kumar, Harish, R. S. Dhaka, and A. K. Pramanik. "Evolution of structure, magnetism, and electronic transport in the doped pyrochlore iridate Y₂Ir_{2-x}Ru_xO₇." *Physical Review B* 95, no. 5 (2017): 054415.

16. Harris, Mark J., S. T. Bramwell, D. F. McMorrow, T. H. Zeiske, and K. W. Godfrey. "Geometrical frustration in the ferromagnetic pyrochlore $\text{Ho}_2\text{Ti}_2\text{O}_7$." *Physical Review Letters* 79, no. 13 (1997): 2554.
17. Kobrak, Mark N. "The chemical environment of ionic liquids: links between liquid structure, dynamics, and solvation." *Advances in Chemical Physics* 139 (2008): 85-138.
18. Hook, John R., and Henry Edgar Hall. *Solid state physics*. John Wiley & Sons, 2013.
19. Goodenough, John B. *Magnetism and the chemical bond*. Vol. 1. Hassell Street Press, 1963.
20. Anderson, Po W. "Antiferromagnetism. Theory of super exchange interaction." *Physical Review* 79, no. 2 (1950): 350.
21. Powell, Annie K. "A bridge to higher ground." *Nature Chemistry* 2, no. 5 (2010): 351-352.
22. Smart, James Samuel. *Effective field theories of magnetism*. Saunders, 1966.
23. Greedan, John E. "Geometrically frustrated magnetic materialsBasis of a presentation given at Materials Discussion No. 3, 26–29 September, 2000, University of Cambridge, UK." *Journal of Materials Chemistry* 11, no. 1 (2001): 37-53.
24. Greedan, John E. "Geometrically frustrated magnetic materials Basis of a presentation given at Materials Discussion No. 3, 26–29 September, 2000, University of Cambridge, UK." *Journal of Materials Chemistry* 11, no. 1 (2001): 37-53.
25. Vannimenus, J., and G. Toulouse. "Theory of the frustration effect. II. Ising spins on a square lattice." *Journal of Physics C: Solid State Physics* 10, no. 18 (1977): L537.

26. Lacorre, P. "The constraint functions: an attempt to evaluate the constraint rate inside structures that undergo ordered magnetic frustration." *Journal of Physics C: Solid State Physics* 20, no. 29 (1987): L775.
27. Harris, Mark J., S. T. Bramwell, D. F. McMorrow, T. H. Zeiske, and K. W. Godfrey. "Geometrical frustration in the ferromagnetic pyrochlore $\text{Ho}_2\text{Ti}_2\text{O}_7$." *Physical Review Letters* 79, no. 13 (1997): 2554.
28. Villain, Jacques. "Insulating spin glasses." *Zeitschrift für Physik B Condensed Matter* 33, no. 1 (1979): 31-42.
29. Anderson, Philip W. "Resonating valence bonds: A new kind of insulator. "Materials Research Bulletin 8, no. 2 (1973): 153-160.
30. Bramwell, Steven T., and Michel JP Gingras. "Spin ice state in frustrated magnetic pyrochlore materials." *Science* 294, no. 5546 (2001): 1495-1501.
31. Pauling, Linus. "The structure and entropy of ice and of other crystals with some randomness of atomic arrangement." *Journal of the American Chemical Society* 57, no. 12 (1935): 2680-2684.
32. den Hertog, Byron C., and Michel JP Gingras. "Dipolar interactions and origin of spin ice in Ising pyrochlore magnets." *Physical review letters* 84, no. 15 (2000): 3430.
33. Harris, Mark J., S. T. Bramwell, D. F. McMorrow, T. H. Zeiske, and K. W. Godfrey. "Geometrical frustration in the ferromagnetic pyrochlore $\text{Ho}_2\text{Ti}_2\text{O}_7$." *Physical Review Letters* 79, no. 13 (1997): 2554.
34. Ramirez, Arthur P., A. Hayashi, Robert Joseph Cava, R. Siddharthan, and B. S. Shastry. "Zero-point entropy in 'spin ice'." *Nature* 399, no. 6734 (1999): 333-335.

35. Matsuhira, Kazuyuki, Yukio Hinatsu, Kenichi Tenya, Hiroshi Amitsuka, and Toshiro Sakakibara. "Low-temperature magnetic properties of pyrochlore stannates." *Journal of the Physical Society of Japan* 71, no. 6 (2002): 1576-1582.
36. Kadowaki, Hiroaki, Yoshinobu Ishii, Kazuyuki Matsuhira, and Yukio Hinatsu. "Neutron scattering study of dipolar spin ice $\text{Ho}_2\text{Sn}_2\text{O}_7$: frustrated pyrochlore magnet." *Physical Review B* 65, no. 14 (2002): 144421.
37. Castelnovo, Claudio, Roderich Moessner, and Shivaji L. Sondhi. "Magnetic monopoles in spin ice." *Nature* 451, no. 7174 (2008): 42-45.
38. Bramwell, S. Tetal, S. R. Giblin, S. Calder, R. Aldus, D. Prabhakaran, and T. Fennell. "Measurement of the charge and current of magnetic monopoles in spin ice." *Nature* 461, no. 7266 (2009): 956-959.
39. Fennell, Tom, P. P. Deen, A. R. Wildes, K. Schmalzl, D. Prabhakaran, A. T. Boothroyd, R. J. Aldus, D. F. McMorrow, and S. T. Bramwell. "Magnetic Coulomb phase in the spin ice $\text{Ho}_2\text{Ti}_2\text{O}_7$." *Science* 326, no. 5951 (2009): 415-417.
40. Binder, Kurt, and A. Peter Young. "Spin glasses: Experimental facts, theoretical concepts, and open questions." *Reviews of Modern physics* 58, no. 4 (1986): 801.
41. Taira, Nobuyuki, Makoto Wakeshima, and Yukio Hinatsu. "Magnetic properties of iridium pyrochlores $\text{R}_2\text{Ir}_2\text{O}_7$ (R= Y, Sm, Eu and Lu)." *Journal of Physics: Condensed Matter* 13, no. 23 (2001): 5527.
42. Liu, Hui, Jian Bian, Shiyun Chen, Junjie Wang, Yuan Feng, Wei Tong, Yu Xie, and Baolong Fang. "Evolution of magnetism and electrical properties in the doped pyrochlore iridate $\text{Y}_2\text{Ir}_{2-x}\text{Fe}_x\text{O}_7$." *Journal of Magnetism and Magnetic Materials* 498 (2020): 166214.

43. Balents, Leon. "Spin liquids in frustrated magnets." *Nature* 464, no. 7286 (2010): 199-208.
44. Petrenko, O. A., M. R. Lees, and G. Balakrishnan. "Magnetization process in the spin-ice compound $\text{Ho}_2\text{Ti}_2\text{O}_7$." *Physical Review B* 68, no. 1 (2003): 012406.
45. Anithakumari, P., V. Grover, C. Nandi, K. Bhattacharyya, and A. K. Tyagi. "Utilizing non-stoichiometry in $\text{Nd}_2\text{Zr}_2\text{O}_7$ pyrochlore: exploring superior ionic conductors." *RSC advances* 6, no. 100 (2016): 97566-97579.
46. Gardner, J. S., S. R. Dunsiger, B. D. Gaulin, M. J. P. Gingras, J. E. Greedan, R. F. Kiefl, M. D. Lumsden et al. "Cooperative paramagnetism in the geometrically frustrated pyrochlore antiferromagnet $\text{Tb}_2\text{Ti}_2\text{O}_7$." *Physical review letters* 82, no. 5 (1999): 1012.
47. Bondah-Jagalu, V., and S. T. Bramwell. "Magnetic susceptibility study of the heavy rare-earth stannate pyrochlores." *Canadian journal of physics* 79, no. 11-12 (2001): 1381-1385.
48. Champion, J. D. M., M. J. Harris, P. C. W. Holdsworth, A. S. Wills, G. Balakrishnan, S. T. Bramwell, E. Čížmár et al. " $\text{Er}_2\text{Ti}_2\text{O}_7$: Evidence of quantum order by disorder in a frustrated antiferromagnet." *Physical Review B* 68, no. 2 (2003): 020401.
49. Greedan, J. E., N. P. Raju, A. Maignan, Ch Simon, J. S. Pedersen, A. M. Niraimathi, E. Gmelin, and M. A. Subramanian. "Frustrated pyrochlore oxides, $\text{Y}_2\text{Mn}_2\text{O}_7$, $\text{Ho}_2\text{Mn}_2\text{O}_7$, and $\text{Yb}_2\text{Mn}_2\text{O}_7$: Bulk magnetism and magnetic microstructure." *Physical Review B* 54, no. 10 (1996): 7189.
50. Lee, J. S., T. W. Noh, J. S. Bae, In-Sang Yang, T. Takeda, and R. Kanno. "Strong spin-phonon coupling in the geometrically frustrated pyrochlore $\text{Y}_2\text{Ru}_2\text{O}_7$." *Physical Review B* 69, no. 21 (2004): 214428.

51. Hatnean, M. Ciomaga, M. R. Lees, O. A. Petrenko, D. S. Keeble, G. Balakrishnan, M. J. Gutmann, V. V. Klekovkina, and B. Z. Malkin. "Structural and magnetic investigations of single-crystalline neodymium zirconate pyrochlore $\text{Nd}_2\text{Zr}_2\text{O}_7$." *Physical Review B* 91, no. 17 (2015): 174416.
52. Yadav, Pramod K., Pinki Singh, Manjari Shukla, Soma Banik, and Chandan Upadhyay. "Effect of B-site substitution on structural, magnetic and optical properties of $\text{Ho}_2\text{Ti}_2\text{O}_7$ pyrochlore oxide." *Journal of Physics and Chemistry of Solids* 138 (2020): 109267.
53. Shukla, Manjari, Rajnikant Upadhyay, Martin Tolkiehn, and Chandan Upadhyay. "Robust spin-ice freezing in magnetically frustrated $\text{Ho}_2\text{Ge}_x\text{Ti}_{2-x}\text{O}_7$ pyrochlore." *Journal of Physics: Condensed Matter* 32, no. 46 (2020): 465804.
54. Pal, Arkadeb, Abhishek Singh, A. K. Ghosh, and Sandip Chatterjee. "High temperature spin-freezing transition in pyrochlore $\text{Eu}_2\text{Ti}_2\text{O}_7$: A new observation from ac-susceptibility." *Journal of Magnetism and Magnetic Materials* 462 (2018): 1-7.
55. Snyder, J., J. S. Slusky, R. J. Cava, and P. Schiffer. "How 'spin ice' freezes." *Nature* 413, no. 6851 (2001): 48-51.
56. Snyder, J., B. G. Ueland, Ari Mizel, J. S. Slusky, H. Karunadasa, R. J. Cava, and P. Schiffer. "Quantum and thermal spin relaxation in the diluted spin ice $\text{Dy}_{2-x}\text{M}_x\text{Ti}_2\text{O}_7$ (M= Lu, Y)." *Physical Review B* 70, no. 18 (2004): 184431.
57. Liu, Hui, Jian Bian, Shiyun Chen, Yuan Feng, Yu Xie, and Baolong Fang. "Magnetic and dynamical properties in the diluted spin ice $\text{Dy}_{2-x}\text{La}_x\text{Ti}_2\text{O}_7$." *Journal of Magnetism and Magnetic Materials* 465 (2018): 316-322.
58. Liu, Hui, Youming Zou, Langsheng Ling, Lei Zhang, Changjin Zhang, and Yuheng Zhang. "Enhanced ferromagnetism and emergence of spin-glass-like transition in

- pyrochlore compound $\text{Dy}_2\text{Ti}_{2-x}\text{V}_x\text{O}_7$." *Journal of Magnetism and Magnetic Materials* 388 (2015): 135-142.
59. Liu, Hui, Youming Zou, Lei Zhang, Langsheng Ling, Hongyan Yu, Lei He, Changjin Zhang, and Yuheng Zhang. "Magnetic order and dynamical properties of the spin-frustrated magnet $\text{Dy}_{2-x}\text{Yb}_x\text{Ti}_2\text{O}_7$." *Journal of magnetism and magnetic materials* 349 (2014): 173-179.
60. Marques, M. D. R., F. S. Portela, A. A. M. Oliveira, Petrucio Barrozo, N. O. Moreno, P. C. A. Brito, and J. Albino Aguiar. "Structural and magnetic properties of pyrochlores $\text{Gd}_{2-x}\text{M}_x\text{Ru}_2\text{O}_7$ (M= Ho, Y)." *Physica B: Condensed Matter* 407, no. 16 (2012): 3106-3108.
61. Gingras, M. J. P., B. C. Den Hertog, M. Faucher, J. S. Gardner, S. R. Dunsiger, L. J. Chang, B. D. Gaulin, N. P. Raju, and J. E. Greedan. "Thermodynamic and single-ion properties of Tb^{3+} within the collective paramagnetic-spin liquid state of the frustrated pyrochlore antiferromagnet $\text{Tb}_2\text{Ti}_2\text{O}_7$." *Physical Review B* 62, no. 10 (2000): 6496.
62. Nakatsuji, S., Y. Machida, Y. Maeno, T. Tayama, T. Sakakibara, J. Van Duijn, L. Balicas, J. N. Millican, R. T. Macaluso, and Julia Y. Chan. "Metallic spin-liquid behavior of the geometrically frustrated Kondo lattice $\text{Pr}_2\text{Ir}_2\text{O}_7$." *Physical review letters* 96, no. 8 (2006): 087204.
63. Millican, Jasmine N., Robin T. Macaluso, Satoru Nakatsuji, Yo Machida, Yoshiteru Maeno, and Julia Y. Chan. "Crystal growth and structure of $\text{R}_2\text{Ir}_2\text{O}_7$ (R= Pr, Eu) using molten KF." *Materials research bulletin* 42, no. 5 (2007): 928-934.
64. MacLaughlin, D. E., O. O. Bernal, Lei Shu, Jun Ishikawa, Yosuke Matsumoto, J-J. Wen, M. Mourigal et al. "Unstable spin-ice order in the stuffed metallic pyrochlore $\text{Pr}_{2+x}\text{Ir}_{2-x}\text{O}_{7-\delta}$." *Physical Review B* 92, no. 5 (2015): 054432.

65. Zhang, Yikun, Huadong Li, Dan Guo, Zhongming Ren, and Gerhard Wilde. "Cryogenic magnetic properties in the pyrochlore RE_2TiMnO_7 ($RE=Dy$ and Ho) compounds." *Ceramics International* 44, no. 13 (2018): 15681-15685.
66. Morosan, E., J. A. Fleitman, Q. Huang, J. W. Lynn, Y. Chen, X. Ke, M. L. Dahlberg, P. Schiffer, C. R. Craley, and R. J. Cava. "Structure and magnetic properties of the $Ho_2Ge_2O_7$ pyrogermanate." *Physical Review B* 77, no. 22 (2008): 224423.
67. Ehlers, G., A. L. Cornelius, T. Fennell, M. Koza, S. T. Bramwell, and J. S. Gardner. "Evidence for two distinct spin relaxation mechanisms in 'hot' spin ice $Ho_2Ti_2O_7$." *Journal of Physics: Condensed Matter* 16, no. 11 (2004): S635.
68. Singh, Prajyoti, Arkadeb Pal, Vinod K. Gangwar, Surajit Ghosh, Ranjan K. Singh, A. K. Ghosh, and Sandip Chatterjee. "Spin freezing and field induced transition in $(Tb_{1-x}Eu_x)_2Ti_2O_7$: A magnetic property study." *Journal of Magnetism and Magnetic Materials* 490 (2019): 165512.

Chapter 2

Techniques for Synthesis and Characterization

In this chapter, synthesis and characterization techniques which have been employed in the present thesis are described. A brief description of sample synthesis by conventional solid-state method is presented. A brief discussion about structural characterization techniques such as X-ray diffraction (XRD), Raman spectroscopy, and Scanning electron microscopy (SEM) is presented. Physical properties measurement systems (PPMS) which are used for the investigation of magnetic properties are also discussed here.

2.1 Introduction

The fundamentals of the experimental methods employed in this thesis to explore the structure and magnetic characteristics of the pyrochlores $R_2Ti_2O_7$ ($R = Ho, Gd, \text{ and } La$) are presented in this chapter. The traditional solid reaction routes were largely used to synthesize ceramic with pyrochlore structures ($A_2B_2O_7$). The specific qualities of the prepared samples were further investigated using a variety of experimental approaches and tools. Subsequently, we discuss the fundamentals of the X-ray methods (Rigaku Miniflex 600) used to figure out the crystalline structure of as-prepared materials. Surface morphology of as-prepared specimens was considered using electron microscopy techniques. The JSM-IT 200 model of JEOL-SEM setup, which has a tungsten-based electron gun operated at 30 kV, was used to conduct the SEM experiments. Magnetic measurements have been performed at low temperatures using physical properties measurement system (cryogenics limited factory-made). Raman spectroscopy was used to examine the phonon anharmonicity and structural ordering in range ($100 - 1000 \text{ cm}^{-1}$) at room temperature.

2.2 Solid State Sintering Synthesis Method

The approach for forming polycrystalline materials from variety of solid starting elements most frequently utilized is the solid-state reaction route. Solid-state reactions are those that take place without the use of solvents and are initiated by melting, grinding, or heating the materials together before the reaction begins. To create the polycrystalline solid from the solid reagents, the solid-state reaction is carried out. For the reaction to proceed at a relevant rate, solids must be warmed to much higher temperatures, often between 1000°C and 1500°C . Ordinarily, solids do not interact with each other at ambient temperature or during usually long time periods. The

feasibility and rate of a solid state reaction are dependent on a variety of factors, as well as the reaction conditions, the structural characteristics of the reactants, the surface areas, the reactivity, and the variation in thermodynamic free energy that the reaction generates. In fact, it aids in our understanding of the substance from the molecular to the crystallographic levels. Nonstoichiometric substances in solid-state chemistry are classified as exclusive solid-state compounds because of their structure and thermodynamic properties. The solid state reaction process is a low-cost, environmentally friendly, and solvent-free method of manufacture. Due to the absence of solvent, more products are created, and waste disposal is not necessary at the end of the process.

Pyrochlore structure ceramics were produced by traditional solid-state sintering techniques [1-4]. A schematic diagram of this method is depicted in **Fig. 2.1**. We have synthesized different pyrochlore structured compounds such as $\text{Ho}_2\text{Ti}_2\text{O}_7$, $\text{Ho}_2\text{Ti}_{2-x}\text{Ge}_x\text{O}_7$ ($x = 0.0, 0.4$ and 0.8), $\text{Ho}_{2-x}\text{La}_x\text{Ti}_2\text{O}_7$ ($x = 0.0, 0.1$ and 0.2) and $\text{Gd}_{2-y}\text{Ho}_y\text{Ti}_2\text{O}_7$ ($y = 0.0, 0.4, 0.8$ and 1.2) *etc* via solid state route. High purity (99.999%) ingredients were procured by Sigma Aldrich. The choice of reactant compounds depends on the circumstances of the reaction and the anticipated composition of the final product. The moisture and contaminants in these ingredients were removed by preheating them for 3 hours. Before weighing the reactants, they are completely dried. After taking the stoichiometric amount all precursors were assorted homogeneously using mortar-pistal. Following complete mixing, the powders were grinded for 8 hours. Using a hydraulic press and polyvinyl alcohol as a binder, the powdered materials were formed into a pellet with thickness and diameter of 2 mm and 8 mm correspondingly. Obtained pellets were heated for 24 hours at 1300°C in an ambient atmosphere. It underwent a second round of regrinding and pelletizing before being heated for 36 hours at 1350°C to improve consistency.

For the purpose of achieving high density, further high temperature heating (1400°C) and slow cooling ($2^{\circ}/\text{minute}$) are needed. It is crucial to choose a suitable substance for the subsequent high-temperature reaction that under the current heating settings is chemically inert to the reactants. Form and reactivity of the reactants have a significant effect on heating protocol that would be applied. Heat treatment is done in an efficient furnace. By initiating a chemical reaction from solid starting components, solid-state synthesis is frequently utilized to create new solids with clearly specified structures.

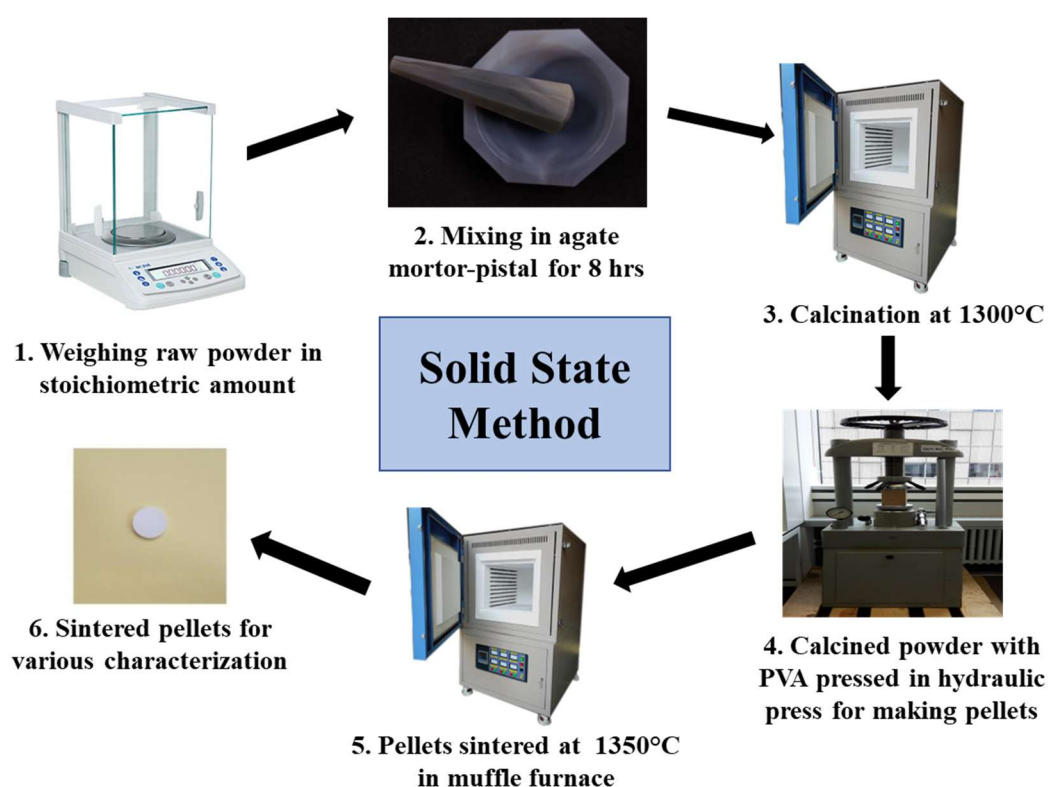


Fig. 2.1 Schematic diagram of the solid-state sintering process.

2.2.1 Application of Solid State Sintering Method

1. Fine powders must be used, and high temperatures are necessary to allow for enough atom diffusion to cause consolidation in a timely manner.
2. These techniques are easy to perform, frequently involve inexpensive starting materials that are easily available, and are "clean" meaning no additional chemical elements are involved.
3. High-quality technical ceramics like ferrite magnetic ceramics and alumina lamp envelopes are produced using this method.
4. Without the need for machining, sintering method enables the creation of complex structures including frontal geometries, splines, profiles, and teeth directly from the compacting tools.
5. It is a brand-new synthetic technique for creating organic compounds, with clear benefits like decreased emissions, low costs, and ease of use. Additionally, these essentials are particularly significant in the industry (sectors).

2.3 Techniques for Structural Analysis

The X-ray diffraction along with Raman spectroscopy techniques were used to probe the crystal structure of the as-prepared pyrochlore structured ceramic materials.

2.3.1 X-ray Diffraction Technique

An Italian mathematician named Francesco Maria Grimaldi performed the first known observations of diffraction, which were later published in 1665 [5]. His investigations showed an apparent bending of light behaviour that the optics that were understood at the time could not account for. It wasn't until 1912 that father and son W. L. and W. H. Bragg began using

diffraction to analyse materials. M. Laue had carried out 1st effective X-ray experiment earlier that year employing a copper sulphate crystal as the diffraction grating. But the Braggs were the ones to point out that a crystalline sample's X-ray diffraction pattern was particular to that material [6]. Places of the high intensity reflections were found to be connected to the X-ray beam wavelength and incident angle. Crystalline materials make up about 90% of all solid substances. Diffraction patterns result from X-ray interactions with crystalline materials. The electromagnetic radiation known as X-rays has a wavelength of 1.5 \AA , which is roughly equal to the inter planner spacing of crystalline solid. In the electromagnetic spectrum, they can be found amid gamma rays and ultraviolet. Researchers were able to examine structures at microscopic level with the discovery of X-rays in 1895. X-rays are exceptional and effective tools for analysing crystalline materials at the atomic level because of their systematic nature. This is conceivable because the interplanar spacing d , distance upright among two neighbouring planes of atom and the X-ray wavelength λ are similar (**Fig. 2.2**).

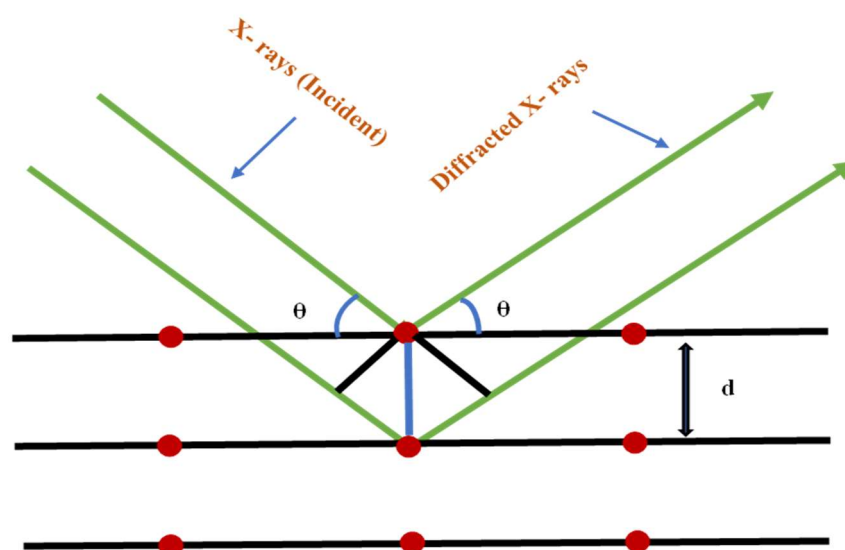


Fig. 2.2 Fundamental idea behind XRD (Bragg's Law).

Consequently, XRD method is class of non-destructive investigative methods that provide details on the chemical composition, physical characteristics and crystallographic structure of ingredients. This method is founded on the observation of intensity of the scattered beam interacting with a specimen as depends on scattered and incident angle, wavelength and polarisation. XRD is a significant investigational method cast-off address a variety of problems, including

1. Measuring the lattice constant and recognizing crystal-like phases that are existing in compounds.
2. Identifying unknown compounds.
3. Location of single crystals is specified.
4. The desired orientation of polycrystal materials is determined.
5. Evaluation of stresses and imperfections in the fabricated specimens that cause lattice disorder.

Each substance has a distinctive pattern of XRD that can be accustomed to identify fingerprints. After the identification of materials, they may be cast-off to ascertain their crystal structure, which includes angle and interatomic distance as well as show atoms are arranged in different forms. The easiest way to find size and cell parameters for any substance is through X-ray diffraction. An XRD instrument determines the radiation intensity diffracted as a function of scan angle 2θ . Using the well-known Bragg's equation, these 2θ values can be used to calculate interplanar separation.

$$2d \sin \theta = n\lambda \dots\dots\dots(2.1)$$

here, order of reflection (n), λ is wavelength of used source ($\text{Cu K}\alpha$), and θ is the angle (Bragg) for diffraction.

Scherer equation (2.2) is used to compute average crystallite size of the materials under investigation. In the 2θ scales, here β is full width and half maximum, d is crystallite size, and $\lambda_{\alpha}=1.5404 \text{ \AA}$ is utilized wavelength, showing strongest X-ray diffraction.

$$d = \frac{(0.89 \lambda)}{\beta \cos \theta} \dots\dots\dots (2.2)$$

The utmost typical design for a laboratory X-ray experiment has a fixed wavelength and rotates through 2θ to measure the intensities and angles of the reflections (**Fig. 2.3**). An electrically heated filament commonly made of tungsten releases electrons that are driven transversely potential difference and impact anode creating an X-ray. Owing to the two different ways that X-rays are formed, two mechanisms make up an X-ray beam. Quick slowdown of the electrons as they come in the metal target causes X-ray radiation to have a continuous or so-called white spectrum. As the electrons approach the nuclei, the attractive force leads them to slow down, which results in an energy reduction and the release of matching X-ray photons of various wavelengths. Bremsstrahlung is the name given to the energy circulation resulting as of this mechanism, which has a circulation of wavelengths proportional to the occurrence energy of electrons. A metal atom's core electron may become loose due to the bombardment of electrons hitting the anode. The hole will be filled by an electron from the outer shell by lowering its energy and releasing a photon (X-ray). Element employed as the anode and level (energy) of the electronic conversion will dictate the distinctive wavelengths of the X-rays produced by this mechanism [8-9]. Each transition is given a name that includes the numeral of midway

energy levels for conversion as well as its concluding energy level ($n = 1, 2,$ or 3 for K, L, or M individually).



Fig. 2.3 Photograph of the X-ray diffractometer system at the School of Physical Sciences, Jawaharlal Nehru University, New Delhi.

In the present thesis, all the samples have been characterized using a Rigaku Miniflex 600 XRD system avail at the School of Physical Sciences, Jawaharlal Nehru University New Delhi. The diffraction pattern is recorded in the range of 10° and 80° with a step size of 0.02° at the slow scan of 0.05° sec. Pseudo Voigt software was used to fitting the measured XRD peak to identify their location, width and intensity. After utilizing the second derivative approach to locate the

peaks in the pattern of XRD, it was also used for determination of phase. The assembled peaks are compared to the JCPDS file.

Rietveld Refinement

Rietveld refinement, a highly effective technique for verifying the structure to which a compound belongs was employed in the structural analysis [10]. Rietveld technique is an improvement procedure that necessitates a preliminary analysis of the crystal structure. The model includes precise information about the chemistry and structure, including lattice constant, space group atom positions, and thermal parameters. The investigation was carried out by applying the programme FULLPROF and its graphical user WINPLOTR [11-12]. The refinement uses a set of rules that reduces discrepancy between investigational data and model that has been assessed using a least-squares method. A set of incorporated points can be used in the analysis to account for the backdrop. It is also possible to provide additional factors, such as peak anisotropic temperature variables, broadening, absorption and geometry. The variables χ^2 , R_{wp} , and R_{exp} control how well the fitting fits. χ^2 is the product of the squares of R_{wp} and R_{exp} , where R_{wp} is the residual weighted by the intensity and R_{exp} is the predicted residual value. Once convergence is attained and the goodness of fit χ^2 value is getting closer to one, the refinement process is complete. Here is a definition of the following factors:

$$R_{wp} = \sqrt{\frac{\sum W_i (y_i - y_{c,i})^2}{\sum W_i y_i^2}} \quad i = 1 \text{ to } n \quad \dots\dots\dots (2.3)$$

$$R_{exp} = \sqrt{\frac{n-p}{\sum W_i y_i^2}} \quad i = 1 \text{ to } n \quad \dots\dots\dots (2.4)$$

$$\chi^2 = \left(\frac{R_{wp}}{R_{exp}} \right)^2 \quad \dots\dots\dots (2.5)$$

Here, the sum of all the data points (n), the number of specific constraints (p), W_i is variance of the intensity restrained y_i , $y_{c,i}$ is computed worth of y at the i^{th} position.

The pseudo-Voigt, Lorentzian, and Gaussian, peak shape functions are frequently used to simulate the intensity of the Bragg reflection. The profile software employed in current work is pseudo-Voigt $V(x)$, which is described as addition of Lorentzian peak $L(x)$ and the Gaussian peak $G(x)$, subjective by the constraint η , which ranges in value from zero to one.

$$V(x) = (1 - \eta)G(x) + \eta L(x) \quad (2.6)$$

It is possible to perform a wide variety of complex functions, including those that enable asymmetric widening at small dispersion angles. Micro-strain or crystallite size causes the broadening of peaks, which can also be accounted for in refinement model.

2.3.2 Raman Spectroscopic Technique

Raman spectroscopy delivers comprehensive data on phase, organic structure, and polymorphic behavior, molecular interactions and crystallinity. It uses scattered light to evaluate the energy modes (vibrational) of a material. It bears the name of C. V. Raman an Indian physicist who joint with K. S. Krishnan, made first observation of Raman scattering in 1928 [13-14]. Raman spectroscopy offers structural evidence as well as the ability to recognize substances using their distinctive Raman fingerprints. It gathers this kind of information by characterizing the material's scattering (Raman).

Raman Scattering

The molecular electron cloud follows the varying electromagnetic field of the photons to become polarised when it is scattered by a molecule. As a result, the molecule moves into a

state with higher energy and absorbs the photon. This is from time to time described as the molecule's virtual state and can be visualized as the formation of a very transitory reaction among molecule and photon [15]. Photon is immediately reemitted as diffused light because the virtual state is unstable. In the mainstream of scattering trials, energy of atoms is unaffected by the photon's interaction and hence the wavelength of scattered photon is same to incoming photons. Rayleigh scattering (elastic) is the primary process, and it occurs here.

Details process of scattering is depicted in **Fig. 2.4**. A somewhat less frequent occurrence is an inelastic scattering mechanism that contains an energy allocation between atoms and scattered photons [16]. When a photon is scattered by atoms that have acquired energy by photon, the phenomenon is known as Stokes scattering, which happens in a photon that drops energy and grows in wavelength. The converse occurs in a process called anti-Stokes scattering, where energy of dispersed photons increases and its wavelength lowers if the atoms acquire energy by relaxing to a higher level. Both anti-Stokes and Stokes processes are equally plausible according to quantum physics. Raman spectroscopy usually detects Stokes Raman scatter because it is almost always stronger than the anti-Stokes scatter.

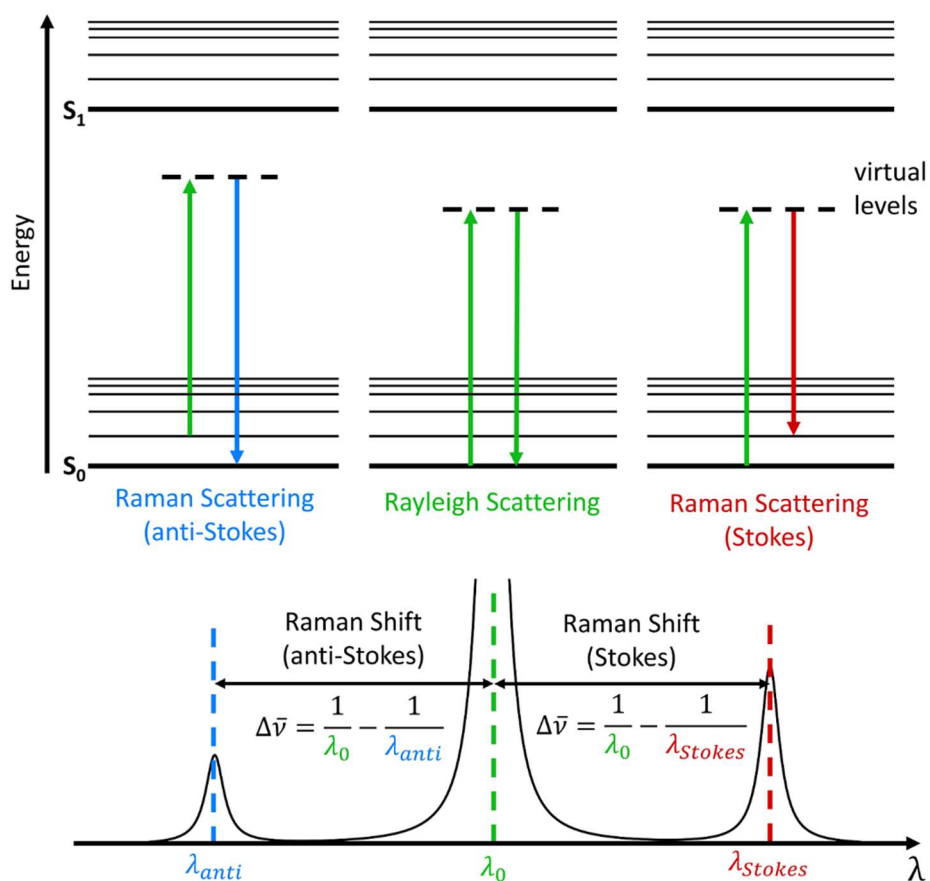


Fig. 2.4 Figure illustrates Stokes, anti-Stokes, and Rayleigh Raman scatter.

Application of Raman Spectroscopy

1. Raman spectroscopy is used in a variety of disciplines, including chemistry to analyze the structure of molecules and their bonds, biology, and medicine to examine low-frequency DNAs and proteins, and nanotechnology to learn about the structure of nanowires.
2. Planetary exploration and remote sensing
3. To detect the minerals on Mars

4. Raman amplification is based on Raman scattering and involves pumping high-frequency photons with extra energy from a low-frequency domain. This approach can be used in telecommunications.
5. Raman spectra are used in optics to create supercontinuum, which produces smooth spectra since the initial spectra are produced spontaneously and are later magnified to higher energies.

2.4 Scanning Electron Microscopy (SEM) Technique

Scanning electron microscope produces a wide assortment of signs at superficial of materials by confined beam of electrons (high energy). Interactions between electrons and samples provide signals that expose data about the material's peripheral texture, chemical configuration, and crystal-like structure and alignment of its composite ingredients. Bulk applications include collecting measurements over a selected part of surface of material and creating a 2D image to display longitudinal alterations in these characteristics [17]. Using traditional SEM methods, areas and widths ranging from 1.0 cm to 5.0 micron can be examined in a scrutinising approach. SEM can also analyse particular positions (pointwise) on material. Use of EDS to estimate composition variation, crystal-like structure, and crystal alignments using this approach is extremely useful (using EBSD). In terms of structure and role, the SEM and EPMA are analogous, and they both have a broad variety of capabilities.

2.4.1 Fundamentals of SEM

When contacting a sample in an SEM, accelerated electrons carry a lot of kinetic energy that is released as a variability of signals through interactions with the sample [18]. These signals are utilized to recognize mineral inclinations and crystal geometries. They consist of secondary,

backscattered, and diffracted backscattered electrons which are used to generate SEM images. Both backscattered and secondary electrons can be used to scan samples, although secondary electrons are finest for depicting morphology and geometry of the compound and backscattered electrons are also superlative for emphasizing elemental variances in interfacial specimens.

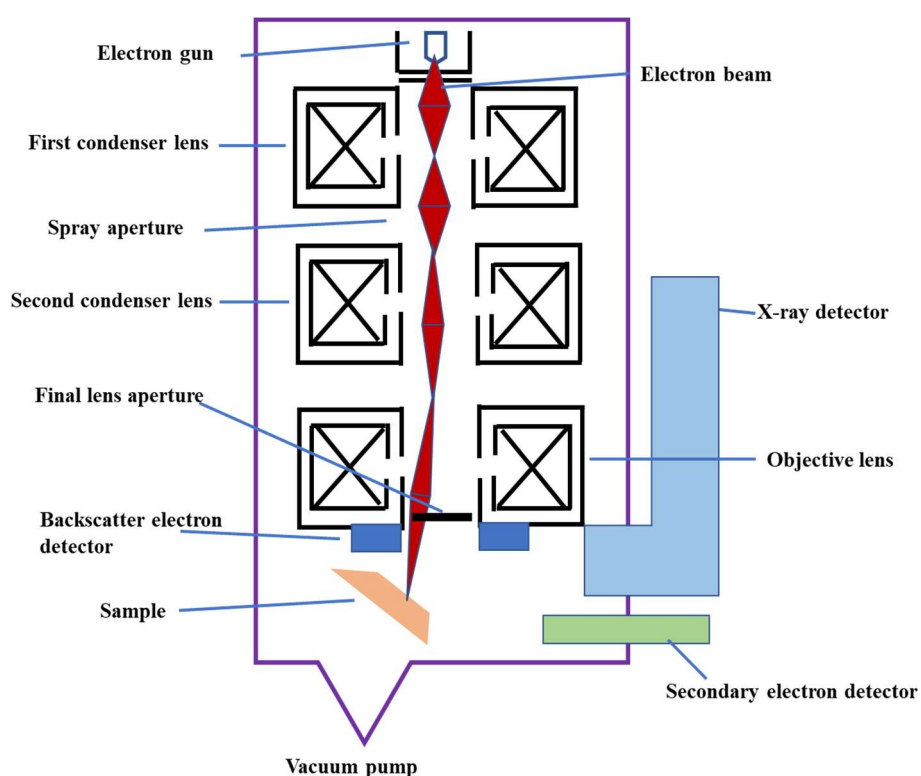


Fig. 2.5 Diagrammatic illustration of a scanning electron microscope.

Accelerated electrons coming back to a lower level, they emit radiations with a particular wavelength (it is associated with variation in energy levels in several shell for a certain component). Therefore, when an inorganic component is "stimulated" by beam of electron, distinct X-rays is released. Diagrammatic illustration of the scanning electron microscope is

displayed in **Fig. 2.5**. It is possible to create a confined beam of electrons by creating electrons at the tip of the column, accelerating them as they descend, and guiding them via a series of lenses and apertures. Then, the restricted electron beam has an impact on the sample's surface. The specimen is set up on a platform in the chamber area, and a series of pumps are used to empty the tower and the container. Scan coils are positioned above the objective lens and control where the electron beam lands on the sample. These coils permit the beam to be moved across surface of the specimen. This beam rastering can be used to obtain data around a precise part of specimens. Collaboration between electrons and material results in a variety of signals being produced. Following that, proper detectors pick up these signals.

2.4.2 Applications of SEM

1. SEM is routinely utilized to produce images with higher resolution of object figures (SEI) and presentations of altitudinal distinctions in organic arrangements [19].
2. Employing EDS to acquire fundamental maps or perform advert chemical tests
3. Utilizing BSE to distinguish between phases relying on the average atomic number, which frequently concerns relative density
4. Compositional charts utilizing CL that take into account differences in element "activators" (usually conversion metals and rare earth gradients)
5. Additionally, SEM is routinely utilized to pinpoint segments using qualitatively chemical analyses and crystal-like structures.

2.5 Physical Property Measurement System (PPMS)

The PPMS is an adaptable measuring platform that offers turnkey and programmable capabilities to monitor a variety of material and device parameters concerning temperature and

magnetic field [20]. It is a computerized low-temperature and magnet system for measuring material characteristics such as DC and AC magnetic susceptibility, specific heat, and both thermal transport and electrical qualities (like Seebeck and Hall effect). With its automated field and temperature control capabilities, the PPMS can incorporate magnetometry applications. The outcome is a robust magnetic workstation for various sample characterization needs. An efficient measurement technique for magnetic sample characterization is vibrating sample magnetometer. PPMS becomes a sensitive DC magnetometer with the VSM option which enables quick data collection [21]. A particular specimen transport, which has a lined characteristic and is therefore extremely precise and adaptable moves sample. The wide bore modification and optional oven help the VSM's capabilities grow. The most interesting feature of the PPMS is that you can do measurements of extraction DC magnetization and AC susceptibility using the AC measurement equipment without altering hardware. Both AC and DC magnetization measurements can be made using a single automated measurement sequence.

In the current research work, DC magnetic measurements of each composition were carried out using a physical properties measurement device made by Cryogenics Limited which is depicted in **Fig. 2.6**. The functional magnetic field varied across the entire measurement between -7 and +7 Tesla. The current work investigated the magnetization behavior with zero field cooling (ZFC) and field-cooled (FC) situations. At various fixed temperatures, additional magnetic field-dependent magnetization is also detected. For the ZFC condition, sample must be cooled in the first stage to the chosen temperature without application of any functional fields, and data must be taken in the second stage while the sample is being heated with the application of DC magnetic field. For FC measurements, there are two possible modes: in the 1st mode data should be collected through the cooling (field cooled cooling) and data must be

obtained during the heating in 2nd mode (field cooled warming). Magnetization versus magnetic field (hysteresis curve) data was also recorded at different low temperatures in the larger field up to seven Tesla.



Fig. 2.6 Physical property measurement system (PPMS) at the Advanced Instrumentation Research Facility (AIRF), Jawaharlal Nehru University, New Delhi.

Following is technical specification of the PPMS used in this research work:

- Completely automatic measurements are made
- The modular architecture provides an extensive range of applications

- Range of temperature (1.9 to 300 K)
- Magnetic field range (-7 Tesla to +7 Tesla).
- Optional cryogen-free function

2.5.1 Applications of PPMS

1. Measurement of dc magnetic hysteresis using vibrating sample magnetometry (VSM) and a magnetic moment sensitivity. Samples with a diameter of up to 6.3 mm can be handled on specimen rods for thin films, powder, liquid samples, and bulk.
2. Determine the Hall effect, AC electrical resistivity, I-V characteristics, and magnetic field and temperature-dependent differential resistance using an AC electrical transport measurement.
3. Thermal conductivity and the Seebeck coefficient are determined through thermal transport measurement.
4. Measurements of the resistance on the four wires of a dc circuit or the van der Pauw method for calculating sheet resistance.
5. Magnetic anisotropy of materials can be assessed using torque magnetometry. The magnetometer's magnetic moment sensitivity is 10^{-11} Am² (10^{-8} emu) at a 14T functional field.

References:

1. Sharma, Saurabh K., Hari S. Mohanty, Dillip K. Pradhan, Ajay Kumar, Vivek K. Shukla, Fouran Singh, and Pawan K. Kulriya. "Structural, dielectric and electrical properties of pyrochlore-type $Gd_2Zr_2O_7$ ceramic." *Journal of Materials Science: Materials in Electronics* 31, no. 24 (2020): 21959-21970.
2. Yadav, Pramod Kumar, Pappu Kumar Harijan, Abhishek Tripathi, and Chandan Upadhyay. "Effect of A-site Fe substitution on the magnetic behavior of $Dy_2Ti_2O_7$ spin ice." *Journal of Magnetism and Magnetic Materials* 481 (2019): 221-226.
3. Sharma, S. K., V. Grover, R. Shukla, A. Hussain, A. Mishra, R. C. Meena, and P. K. Kulriya. "Evidence of improved tolerance to electronic excitation in nanostructured $Nd_2Zr_2O_7$." *Journal of Applied Physics* 129, no. 11 (2021): 115902.
4. Kumar, A., P. K. Kulriya, S. K. Sharma, V. Grover, A. K. Tyagi, and V. K. Shukla. "Structural and compositional effects on the electronic excitation induced phase transformations in $Gd_2Ti_2-yZr_yO_7$ pyrochlore." *Journal of Nuclear Materials* 539 (2020): 152278.
5. F. M. Grimaldi. *Physico-mathesis de lumine, coloribus, et iride, aliisque ad nexis libri duo*. Bologna, Italy, (1665)
6. Bragg, William H. "X-rays and crystalline structure." *Science* 40, no. 1040 (1914): 795-802.
7. Smart, L. E., and E. A. Moore. "An Introduction to Solid State Chemistry." (2005).
8. Gaston, Kevin J. *The structure and dynamics of geographic ranges*. Oxford University Press on Demand, (2003).

9. Panghal, Asha, Yogendra Kumar, P. K. Kulriya, Parasharam M. Shirage, and N. L. Singh. "Atomic order-disorder engineering in the $\text{La}_2\text{Zr}_2\text{O}_7$ pyrochlore under low energy ion irradiation." *Ceramics International* 47, no. 14 (2021): 20248-20259.
10. Radhakrishnan, A. N., P. Prabhakar Rao, KS Mary Linsa, M. Deepa, and Peter Koshy. "Influence of disorder-to-order transition on lattice thermal expansion and oxide ion conductivity in $(\text{Ca}_x\text{Gd}_{1-x})_2(\text{Zr}_{1-x}\text{M}_x)_2\text{O}_7$ pyrochlore solid solutions." *Dalton Transactions* 40, no. 15 (2011): 3839-3848.
11. Rietveld, Hugo M. "A profile refinement method for nuclear and magnetic structures." *Journal of applied Crystallography* 2, no. 2 (1969): 65-71.
12. Rodríguez-Carvajal, Juan. "Recent advances in magnetic structure determination by neutron powder diffraction." *Physica B: Condensed Matter* 192, no. 1-2 (1993): 55-69.
13. Raman, Chandrasekhara Venkata, and Kariamanikkam Srinivasa Krishnan. "A new type of secondary radiation." *Nature* 121, no. 3048 (1928): 501-502.
14. Graves, P. R. G. D. J., and D. Gardiner. "Practical raman spectroscopy." *Springer* 10 (1989): 978-3.
15. Chou, Kuo-Cheng, and Nian-Yi Chen. "The biological functions of low-frequency phonons." *Scientia Sinica* 20, no. 4 (1977): 447-457.
16. Smith, E., and G. Dent. "Wiley Ed." *Modern Raman Spectroscopy: A Practical Approach* 1 (2005): 224.
17. McMullan, D. "Scanning electron microscopy 1928–1965." *Scanning* 17, no. 3 (1995): 175-185.
18. Pease, R. F. W. "Significant advances in scanning electron microscopes (1965–2007)." *Advances in Imaging and Electron Physics* 150 (2008): 53-86.

19. Smith, K. C. A., and C. W. Oatley. "The scanning electron microscope and its fields of application." *British Journal of Applied Physics* 6, no. 11 (1955): 391.
20. Foner, Simon. "Versatile and sensitive vibrating-sample magnetometer." *Review of Scientific Instruments* 30, no. 7 (1959): 548-557.
21. Smith, D. O. "Development of a vibrating-coil magnetometer." *Review of Scientific Instruments* 27, no. 5 (1956): 261-268.

Chapter 3

Structural Magnetic Properties Correlation in B Site Ge Doped Frustrated $\text{Ho}_2\text{Ti}_2\text{O}_7$ Pyrochlore

This chapter mainly attention to the correlation of Structural and magnetic properties of frustrated $\text{Ho}_2\text{Ti}_{2-x}\text{Ge}_x\text{O}_7$ ($x = 0.0, 0.4, \text{ and } 0.8$) compounds by partial doping Ge by Ti (B-site). The excellent spin-ice features and conspicuous quantum character of holmium titanates ($\text{Ho}_2\text{Ti}_2\text{O}_7$) are widely known. X-ray diffraction along with Raman spectroscopic investigations confirmed the formation of the cubic pyrochlore structure with cell parameters vary linearly and follow Vegard's rule. Raman spectroscopy also exhibits a blue shift and hardening of phonon mode due to anharmonic interaction. Low-temperature magnetic experiments have shown that the ferromagnetic connection is lessening because the chemical pressure in $\text{Ho}_2\text{Ti}_2\text{O}_7$ is increasing. No spin glassy conversion was traced at any temperature.

3.1 Introduction

Holmium titanate ($\text{Ho}_2\text{Ti}_2\text{O}_7$) is familiar for its outstanding spin-ice features as well as for prominent quantum character. Geometrically frustrated magnets have been a field of interest for the last two decades because of their rich assortment of eccentric degenerate ground states [1, 2] and its interesting magnetic behaviour like spin liquids [3], spin glass [4], and spin ice [5, 6]. Rare-earth ions with unpaired electrons in 4f configuration show large magnetic moments that result in their strong magnetic properties. Recently, pyrochlore structured oxides with rare-earth ions at one cationic site have been explored to draw interesting magnetic properties driven by geometrical frustration of spin-spin interactions. These materials have also been used as electrolytes [7], nuclear reactor materials [8, 10], and solid catalysts [11]. In these constituents, the nature of spin fluctuations is linked by different spin configurations. The rare-earth ion based pyrochlore oxides are a family of composites with the chemical formula $\text{A}_2\text{B}_2\text{O}_7$. The pyrochlore frame is considered as two diffusive grids of the tetrahedron in which A and B atoms each be present in the apogees of one such association. The pyrochlore is cubic structure belongs to the $Fd\bar{3}m$ space group. In pyrochlore, 16d and 16c sites are occupied by A and B atoms respectively, likewise, 48f and 8b positions are resided by oxygen atoms with different cationic environment [12-14]. Titanate pyrochlore ($\text{A}_2\text{Ti}_2\text{O}_7$ where A = Ho, Dy, Gd, and Tb *etc.*) are recognized as geometrically frustrated magnetic ingredients, where Ti atoms occupy 16c Wyckoff position of the crystal structure [15-17]. In the view of structural analysis, ratio of cationic radii, R ($1.46 \leq R_A/R_B \leq 1.78$) is considered as structural stability parameter. The titanate pyrochlore is the stable composition with value of $R \geq 1.75$. There is another factor, x parameter of 48f oxygen (O_{48f}) having the structural stability range from 0.3125 to 0.3750 [18]. $\text{Tb}_2\text{Ti}_2\text{O}_7$ spins are of dynamic nature till the lower most possible temperature whereas paramagnetic (dynamic) and ordered spins exist simultaneously in $\text{Gd}_2\text{Ti}_2\text{O}_7$ [19-22]. In the

literature, $\text{Ho}_2\text{Ti}_2\text{O}_7$ pyrochlore has been confirmed as spin ice [23]. Ferromagnetic exchange interactions are produced due to strong crystal-field induced Ising-type anisotropy which causes a “two-in/two-out” arrangement in the spin configuration as per spin ice rule [8, 24]. Ferromagnetic dipolar interaction coupled with antiferromagnetic exchange interaction amongst neighbouring spins leads to 6-fold degenerate ground state in spin ice material. Owing to this degeneracy factor, such material shows computable residual entropy $S=R/2 \ln(3/2)$ where R is the gas constant [8, 25]. In titanates pyrochlore, low-temperature magnetic properties are determined by dipolar interaction (D_{nn}) and exchange interaction (J_{nn}) between adjacent neighbouring spins. The ratio of exchange (J_{nn}) and dipolar (D_{nn}) constants decides the stability of spin ice. In case of $J_{nn}/D_{nn} > -0.91$ spin ice is found to be stable whereas the system experiences a lower temperature antiferromagnetic ordered state for $J_{nn}/D_{nn} < -0.91$ as elucidated by Gingras and den Hertog [26]. $\text{Ho}_2\text{Ti}_2\text{O}_7$ is a strong spin ice candidate that possesses ferromagnetic Curie Weiss temperature $\theta_{cw} \sim 1$ K. But it does not develop long-range ordering when the temperature was lowered to 50 mK [27]. Titanate pyrochlore also exhibits composition dependent Curie Weiss temperature such as $\theta_{cw} \sim 1$ K, ~ -1.35 K and -0.8 K for $\text{Dy}_2\text{Ti}_2\text{O}_7$ [28], $\text{Eu}_2\text{Ti}_2\text{O}_7$ [13], and $\text{Yb}_2\text{Ti}_2\text{O}_7$ [29], respectively.

There is similarity of structure and crystal-chemical appeal among pyrogermanates ($\text{R}_2\text{Ge}_2\text{O}_7$) and titanates ($\text{R}_2\text{Ti}_2\text{O}_7$), which have been extensively studied due to their spin-spin interaction. Therefore, complete investigation of magnetic and structural properties of this family is required. Though, in earlier reports, the structure and magnetic behavior of $\text{Ho}_2\text{Ti}_2\text{O}_7$ and $\text{Ho}_2\text{Ge}_2\text{O}_7$ have been attempted individually [30-32]. It is very challenging to learn chemical pressure effect on the magnetic behavior of $\text{Ho}_2(\text{Ti}_{1-x}\text{Ge}_x)_2\text{O}_7$ (HTGO) binary solid-solution of pyrochlore. In this chapter, an effort made to explore the relation between magnetic and structural properties of HTGO pyrochlore oxide. Single phase pyrochlore structure in the

germanium doped holmium titanate pyrochlore HTGO is prepared via solid-state route. The availability of superior material is specifically vital for understanding the physical properties and behaviour of this group of frustrated magnets and predominantly, for studying the character of the magnetic ground state. The increment in R_A/R_B ratio or variation in O_{48f} oxygen with increase in the Ge content over Ti shows that the pyrochlore superstructural ordering enhances on increasing x-value in $Ho_2(Ti_{1-x}Ge_x)_2O_7$. On the other hand, magnetic investigation of frustrated magnet $Ho_2(Ti_{1-x}Ge_x)_2O_7$ pyrochlore showed a reduction in magnetization due to weakening of ferromagnetic interaction and non-magnetic 16c site contributed by increase in chemical pressure. Thus, a more stable pyrochlore structured composition displays a lesser ferromagnetic nature. Further, spin glass-like transition was not detected even after lowering the temperature up to 2 K.

3.2 Synthesis and Characterization

$Ho_2(Ti_{1-x}Ge_x)_2O_7$ ($x = 0, 0.2$ and 0.4) were synthesized using standard solid-state technique [33]. The high purity (>99.99%) analytical reagent (AR) grade powders of Ho_2O_3 , TiO_2 , and GeO_2 procured from Sigma Aldrich, were used as precursors materials. In the beginning of synthesis, the rough weighed raw powders were heated at $600\text{ }^\circ\text{C}$ in air atmosphere for 10 hours to eliminate moisture and impurities. The stoichiometric amounts of powders were weighed immediately after pre-heating treatment. These materials were crushed homogeneously and ground for 10 hours using mortar and pestle, followed by pelletized into a cylindrical shape having thickness 1.5 mm and diameter 8 mm with the help of hydraulic press at a pressure of 3.0 tons. The cylindrical pellets were calcined at $1350\text{ }^\circ\text{C}$ for 24 hours in air atmosphere using muffle furnace. In the next step, regrinding and repelletizing was done which is followed by

sintering at 1400 °C for 36 hours. During heat treatment, the heating and cooling rate was kept at 2 °C/min for better stabilization of pyrochlore superstructure in the synthesized oxide.

Rigaku Miniflex 600 (X-ray diffractometer) set up was used for the structural characterization of samples. The XRD data were collected for $2\theta = 10^\circ$ to 70° with the rate of scanning of $2^\circ/\text{min}$ and analysed by the Rietveld refinement Fullprof program [34]. The surface morphology of the as-prepared materials was studied by field emission scanning electron microscope (FESEM). Raman spectroscopic measurement was performed to investigate the short-range structural ordering and phonon anharmonicity in the range of 100 cm^{-1} to 800 cm^{-1} at room temperature. The chemical composition of the as-prepared compounds was determined by energy-dispersive X-ray spectrometer (EDX). The DC magnetic measurement of each sample was performed using cryogenics limited factory-made physical properties measurement system (PPMS) at low temperatures. The applied magnetic field was varying between -70 kOe to +70 kOe during characterization. Density was measured using an auto calibrated and integrated electronic balance based on Archimedes' principle (AC-CY224C, ACZET PVT LTD). The instrument has the maximum weighing capacity of 220 g with precision/readability of 0.001 g.

3.3 Results and Discussions

3.3.1 Structural Investigation using XRD

The X-ray diffraction studies were used to investigate the structural analysis of the $\text{Ho}_2(\text{Ti}_{1-x}\text{Ge}_x)_2\text{O}_7$ solid solution. The values of ionic radius used in the present investigation for Ho^{3+} , Ti^{4+} , and Ge^{4+} ions are 1.015 Å, 0.605 Å, and 0.530 Å, respectively. The stability factor (R) of HTGO samples is determined using the following equation [35].

$$\frac{R(Ho^{3+})}{R(B^{4+})} = \frac{R(Ho^{3+})}{(1-x)R(Ti^{4+}) + xR(Ge^{4+})} \dots \dots \dots (3.1)$$

The estimated values of ionic radii ratio of HTGO compounds come out as 1.68 (Ho₂Ti₂O₇), 1.72 (Ho₂Ti_{1.6}Ge_{0.4}O₇), and 1.77 (Ho₂Ti_{1.2}Ge_{0.8}O₇) which lie in the range of 1.46 to 1.78. It is a strong hint of attained pyrochlore structure by all compositions. It is plausible that all three compositions would contain pyrochlore super-structural ordering which should increase on the replacement of Ti-content by Ge ion. For R ≤ 1.46, the obtained structure is anion-deficient fluorite structure. This pyrochlore superstructural ordering increases on increasing R-value and cubic structure transforms into monoclinic structure for R>1.78 [36]. Thus, all compositions have single pyrochlore phase without any impurity phase. Though, few impurities were found when x > 0.4 (depicted in **Fig. 3.1**).

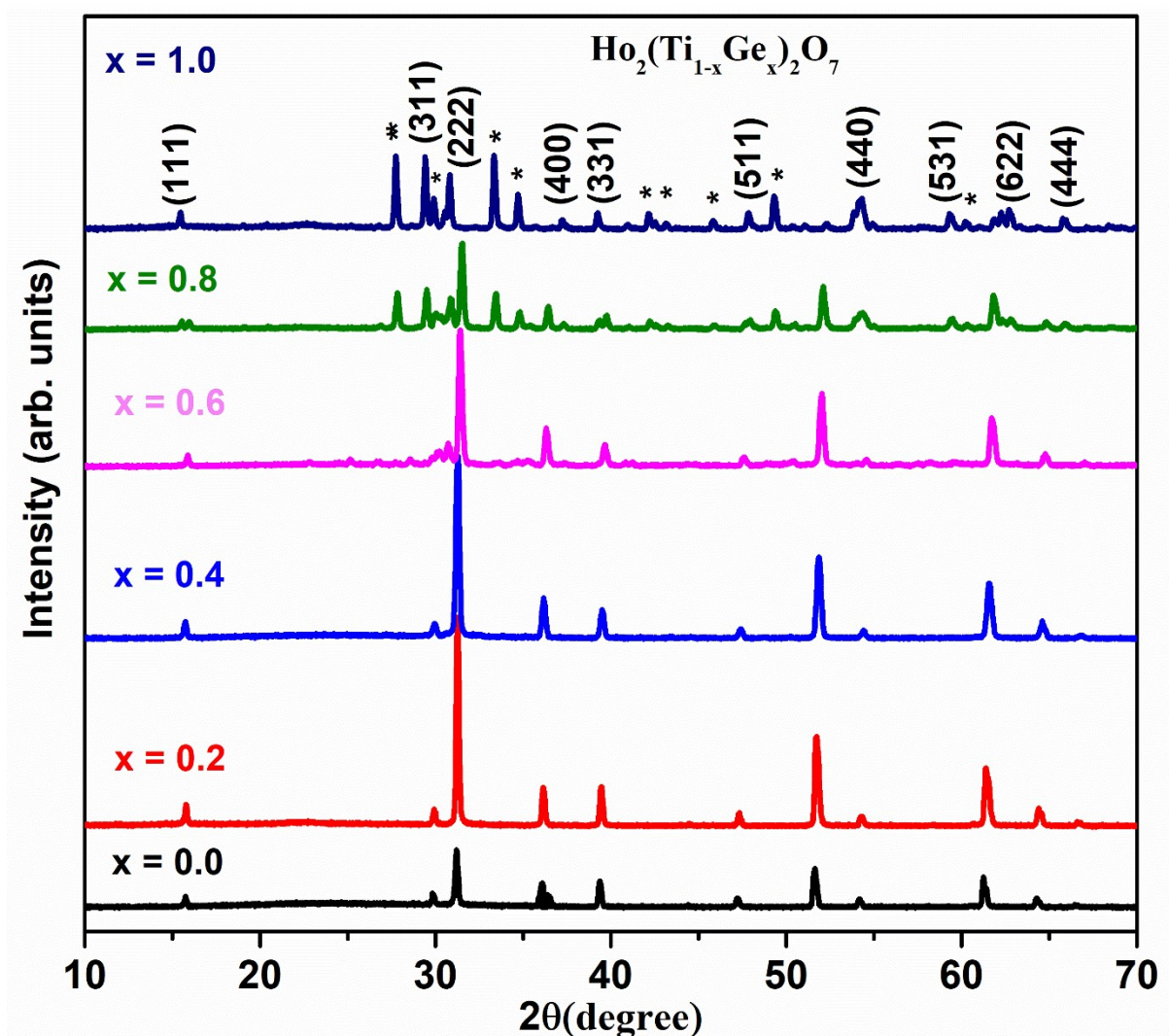


Fig. 3.1 X-ray diffraction pattern of $\text{Ho}_2(\text{Ti}_{1-x}\text{Ge}_x)_2\text{O}_7$ system at RT (300 K).

$\text{Ho}_2(\text{Ti}_{1-x}\text{Ge}_x)_2\text{O}_7$ ($x = 0.6, 0.8,$ and 1.0) compositions with ionic radii ratio that are beyond the stability region. For $\text{Ho}_2\text{Ti}_{0.8}\text{Ge}_{1.2}\text{O}_7$, $\text{Ho}_2\text{Ti}_{0.4}\text{Ge}_{1.6}\text{O}_7$ and $\text{Ho}_2\text{Ge}_2\text{O}_7$ the corresponding computed radius ratios are 1.81, 1.86, and 1.92. XRD data of all compounds XRD (shown in **Fig. 3.1**) failed to reveal the single phase pyrochlore structure. These compositions show few impurities peaks. An asterisk denotes each of these impurity-based peaks. These contaminated samples ($x = 0.6, 0.8,$ and 1.0) weren't considered for Rietveld refinement or other magnetic characterizations.

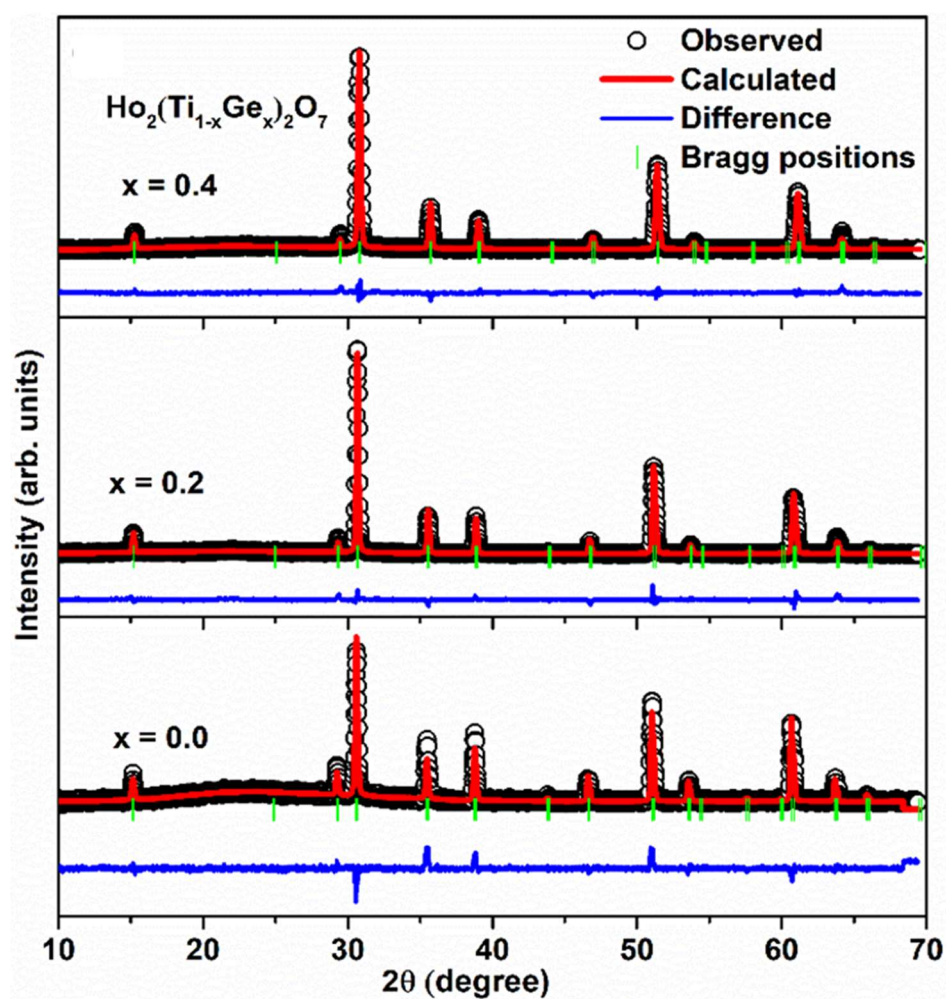


Fig. 3.2 Rietveld refinement fitted X-ray diffraction pattern of $\text{Ho}_2(\text{Ti}_{1-x}\text{Ge}_x)_2\text{O}_7$ system recorded at room temperature.

A series of XRD patterns recorded for HTGO ($x = 0, 0.2,$ and 0.4) compounds to confirm the single pyrochlore structure, are shown in **Fig. 3.2**. Basically, XRD data of pyrochlore oxides consists of strong maxima belonging to a set of planes with even miller indices, namely (222), (400), (440), (622), and (444), positioned at $2\theta = 31.21^\circ, 36.08^\circ, 51.63^\circ, 61.33^\circ,$ and 64.31° , respectively. Another set of planes are having relatively lesser intensity with odd miller indices namely, (111), (311), (331), (511), and (531) positioned at $2\theta = 15.75^\circ, 29.88^\circ, 39.38^\circ, 47.23^\circ,$

and 54.19° , respectively. The presence of these planes with odd miller indices shows whether synthesized samples endue with pyrochlore structure ($Fd\bar{3}m$) or fluorite structure ($Fm\bar{3}m$). The above-mentioned positions of XRD peaks are estimated for $\text{Ho}_2\text{Ti}_2\text{O}_7$ and other compositions have similar diffraction pattern except slight variation in the peak positions. Diffraction patterns were further analysed through Rietveld refinement for detailed structural investigation. The lattice parameter, x-parameter of O_{48f} , and bond-length of all specimen were calculated through refinement. In the refinement process, the data were fitted using the linear interpolation method and pseudo-Voigt function for describing the background and diffraction peaks. The obtained values of reliable parameters (R_p , R_{wp} , and χ^2) and lattice constants of HTGO compounds are presented in **Table 3.1**. These parameters suggest good match between estimated and experimental results. The estimated lattice constants of all samples are in decent agreement with prior reports [37]. The Wyckoff positions of cations and O_{8b} oxygen are kept fixed while x parameter of O_{48f} is left free to stabilize according to structure during refinement. The structural refinement of all three compositions was performed with the help of free factors like cell parameter, temperature coefficient, full width at half maxima (FWHM) parameters, scale factors, and B_{overall} parameter.

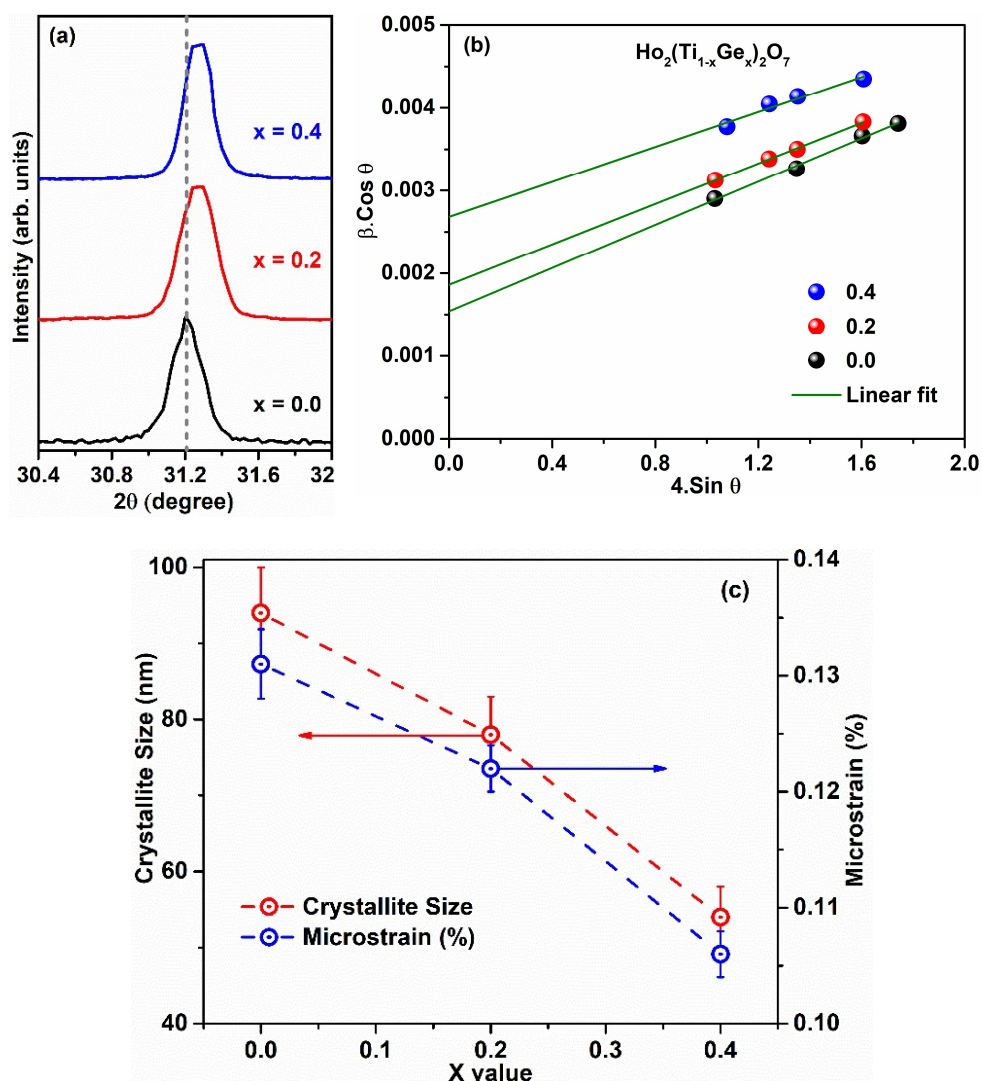


Fig. 3.3 (a) Magnified view of (222) planes in XRD data, (b) W-H plots, and (c) variation in grain size as well as micro-strain (%) for $\text{Ho}_2(\text{Ti}_{1-x}\text{Ge}_x)_2\text{O}_7$ system.

The Rietveld refined of all three diffraction patterns endorse the cubic structure with the atomic arrangement belonging to $Fd\bar{3}m$ space group. The refined values of Bragg's factors; R_p , R_{wp} , and R_{exp} , and goodness of fit (χ^2) show the figure of merit of the Rietveld refinement. It must be noted that a decreasing trend in lattice constant came out on increasing doping of Ge. The diffraction patterns with shifting in all XRD peaks towards higher 2θ values indicates reduction

in unit cell on increasing Ge content over Ti [Fig. 3.3 (a)]. The lattice parameter decreases on the doping of Ge ion at B-site leading to shift in the peak towards the higher Bragg angle because the ionic radius of Ge (0.530 Å) is smaller than that of Ti (0.605 Å). Thus, incorporation of a relatively larger ion in the cationic lattice is obeying Vegard's rule [17].

Table 3.1 Structural parameters calculated from Rietveld fitting and W-H plots of diffraction patterns for $\text{Ho}_2(\text{Ti}_{1-x}\text{Ge}_x)_2\text{O}_7$.

$\text{Ho}_2(\text{Ti}_{1-x}\text{Ge}_x)_2\text{O}_7$	$x = 0.0$	$x = 0.2$	$x = 0.4$
a (Å)	10.1184(5)	10.0965(3)	10.0551(3)
48f (x, 0, 0)	0.3106(11)	0.3213(5)	0.3246(5)
Ho–O_{48f} bond distance (Å)	2.621(9)	2.537(4)	2.504(3)
Ho–O_{8b} bond distance(Å)	2.1770 (0)	2.1860 (1)	2.1907 (0)
Ti/Ge–O_{48f} bond distance(Å)	1.929(4)	1.925(3)	1.891(2)
R_p, R_{wp}, R_{exp}, and χ^2	22.9, 21.8, 15.8, and 3.85	18.1, 18.5, 12.0, and 2.39	19.2, 18.9, 12.6, and 2.24
Crystallite size (nm)	94 (6)	78 (5)	54 (4)
Micro-strain (%)	0.131 (3)	0.122 (2)	0.106 (2)

The W-H formalism was used to determine crystallite size and micro-strain according to the following relation

$$\beta_{hkl} \cdot \text{Cos}(\theta_{hkl}) = \frac{k \cdot \lambda}{D} + 4 \cdot \epsilon \cdot \text{Sin}(\theta_{hkl}) \dots \dots \dots (3.2)$$

Where β_{hkl} and θ_{hkl} stand for FWHM and XRD peak position, respectively. The structural parameter 'k' is kept 0.94 for spherical crystals in this cubic symmetry and the wavelength of used X-rays source of copper K_{α} -line is 1.54056 Å. The derived parameters are crystallite size (D) and micro-strain (ϵ). The linear plots between $\beta_{hkl} \cdot \cos(\theta_{hkl})$ and $4 \cdot \sin(\theta_{hkl})$ are shown in **Fig. 3.3 (b)**. The crystallite size and micro-strain estimated from the y-intercept and slope respectively are plotted with respect to Ge-content [**Fig. 3.3 (c)**] showing decrease in the crystallite size on increasing Ge^{4+} ion concentration. Along with that, micro-strain also decreases monotonically as a function of increasing Ge-concentration shows the lattice relaxation on merger of smaller sized ion in the cationic lattice. Thus, comprehensive structural investigation exhibits the perfectly single phasic nature in all three synthesized samples with complete dissolution of Ge-ion at the place of Ti^{4+} .

3.3.2 Raman Spectroscopy Investigation

Raman spectroscopy is an important technique for structural examination to explore the short-range structural ordering, distortions, local imperfection, and phonon-anharmonicity in a specimen. It also delivers information about electron-phonon, phonon-phonon, and phonon-spin interactions. The Raman spectra of the HTGO series are revealed in **Fig. 3.4**. The pyrochlore complex oxide depiction phonons modes such as $\Gamma = 4F_{2g} + E_g + A_{1g} + 7F_{1u}$, where $4F_{2g}$, E_g and A_{1g} are Raman active modes and $7F_{1u}$ is infrared active mode, as recommended by factor group theory [38, 39]. All Raman modes in **Fig. 3.4** assigned on the basis of prior reports [40]. **Fig. 3.4** shows the perfectly deconvolution of Raman spectra into seven Raman modes. The peak with maximum intensity which lies at the wavenumber of $\sim 310.1 \text{ cm}^{-1}$ holds F_{2g} and E_g Raman modes in which F_{2g} mode corresponds to $\text{O}_{48f}\text{-Ho-O}_{48f}$ bending modes whereas E_g mode links to O_{48f} sublattice modes. The second most intense peak appearing at the

wavenumber $\sim 519.7 \text{ cm}^{-1}$ holds A_{1g} mode which is associated with extending of Ho-O_{48f} stretching bond. The peak with lowermost frequency lying at the wavenumber of $\sim 200.9 \text{ cm}^{-1}$ corresponds F_{2g} mode which is allied to O_{8b} sublattice vibration. Among the remaining two F_{2g} Raman modes, one lies at the wavenumber of $\sim 401.4 \text{ cm}^{-1}$ and the other one at the wavenumber of $\sim 552.9 \text{ cm}^{-1}$ in the present case. There are extra two modes signified by an asterisk above 600 cm^{-1} are assigned to the mix mode as a replacement for the forbidden IR mode [41]. The pyrochlore phase in HTGO is confirmed by the presence of A_g and E_g modes which is in accordance with XRD data.

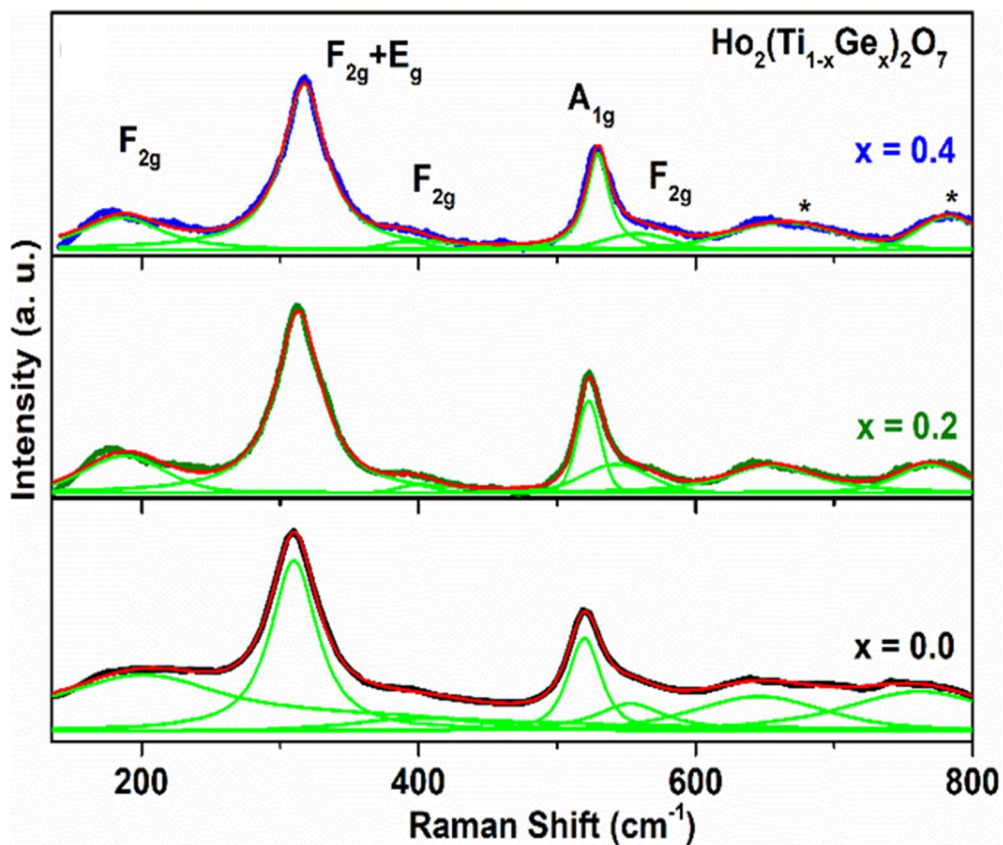


Fig. 3.4 Raman spectra of $\text{Ho}_2(\text{Ti}_{1-x}\text{Ge}_x)_2\text{O}_7$ pyrochlore recorded at room temperature.

Relation between Raman modes with concentration of Ge^{4+} has been presented in Fig. 3.5. Based on data, it can be clearly observed that four modes ($F_{2g} \sim 200.9 \text{ cm}^{-1}$, $F_{2g}+E_g \sim 310.1 \text{ cm}^{-1}$, and $A_{1g} \sim 519.7 \text{ cm}^{-1}$) expressed hardening behaviour with increasing Ge ions. Normally, the position of Raman active modes provides an information about the bond length and ionic mass. In the present case, the lattice parameters are decreasing with increasing Ge concentration which leads to the shifting of phonon modes (F_{2g} , A_{1g} , and $F_{2g}+E_g$) towards higher frequency.

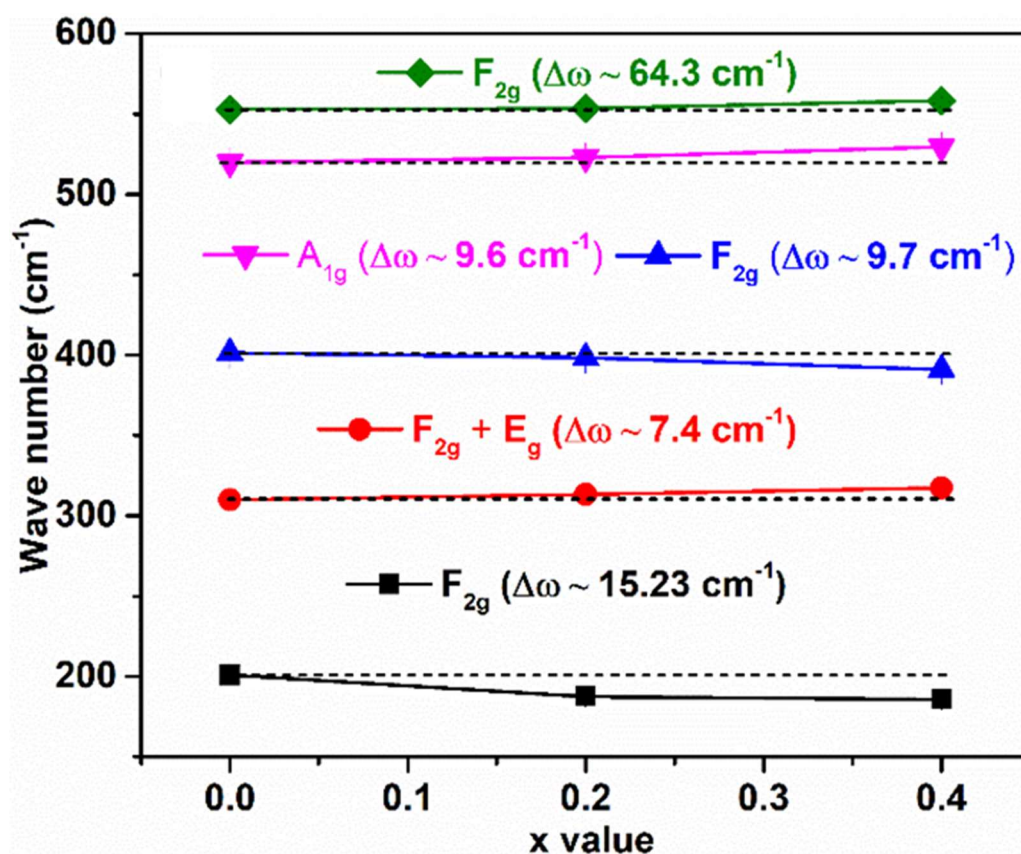


Fig. 3.5 Variation of all Raman active modes with respect to Ge concentration (dotted lines for reference).

In vibrational spectroscopic analysis, blue shifting in Raman active modes is attributed to the decreasing bond-length or increasing force constant which, in turn, linked with atomic lattice shrinkage. This hardening behaviour of the phonon mode appears due to robust anharmonic

interaction among phonons in the system [35]. This blue shift in the frequency of phonons can be validated with the decreasing bond length of O_{48f} sublattice as noted by Rietveld-refinement of diffraction patterns. This reduction in bond-length shows the increasing force constant or decreasing unit cell by the accommodation of larger sized cation (Ge^{4+}) over the smaller one (Ti^{4+}) in HTGO series. Moreover, as concentration of Ge^{4+} ions start increasing, there is decrease in the peak intensities. The red-shift in both F_{2g} vibrational modes can be associated with the increasing bond-length of O_{8b} sublattice as reported by Rietveld-refinement in **Table 3.1**. It is noteworthy that both XRD and Raman spectroscopy confirms single pyrochlore structure in HTGO series with the substitution of Ti ions by Ge ions.

3.3.3 Compositions and Microstructure Analysis

Energy-dispersive X-ray measurement was performed to determine the elemental composition in the as-synthesized samples. The compositions of B site elements are smaller than nominal composition in all compounds as shown in **Table 3.2**. This indicates that HTGO system has additional Ho^{3+} ions on the Ti^{4+} (B site). This phenomenon is known as stuffing, which was also detected in other titanates such as $Yb_2Ti_2O_7$ [42]. On the other hand, EDX results regarding Ge/Ti ions at B-cationic site endorses the doping of Ge at the place of Ti-cation.

Table 3.2 Experimental and nominal mass (%) of the $\text{Ho}_2(\text{Ti}_{1-x}\text{Ge}_x)_2\text{O}_7$ compounds.

$\text{Ho}_2(\text{Ti}_{1-x}\text{Ge}_x)_2\text{O}_7$	Nominal mass (%)				Experimental mass (%)		
	Ho	Ti	Ge	O	Ho	Ti	Ge
$x = 0.0$	61.36	17.81	0.00	20.83	61.69	17.76	0.00
$x = 0.2$	60.25	13.99	5.31	20.46	62.92	11.92	5.42
$x = 0.4$	59.18	10.31	10.42	20.09	62.02	8.52	10.07

The surface morphology of the synthesized compound was analysed by scanning electron microscope (SEM). The SEM images of HTGO samples having compositions $x = 0.0, 0.2$ and 0.4 are presented in **Fig. 3.6 (a, c & d, respectively)**. Obtained image displays the surface morphology, porosity, and grain size in HTGO pyrochlore. Sintering of the samples at the elevated temperature leads to grain growth which is shown by the formation of compact microstructure. The defined crystal grain boundaries are evidently visible and simply distinct with no tiny imperfections. To determine the average grain size, size distribution histogram was plotted by measuring the diameter of 100 grains from various SEM micrographs. These histograms were fitted with Gaussian function to extract average grain size. The Gaussian fit size distribution histogram is shown in **Fig. 3.6 (b)** which corresponds to $x = 0.0$. The average grain size as calculated from SEM images are ~ 6.2 (2) μm , ~ 4.9 (6) μm and 3.8 (9) μm for the samples $x = 0.0, 0.2$ and 0.4 . It is observed that the average grain size decreases with an increasing amount of Ge at the B site. The result obtained from the SEM micrographs is in good agreement with the XRD data.

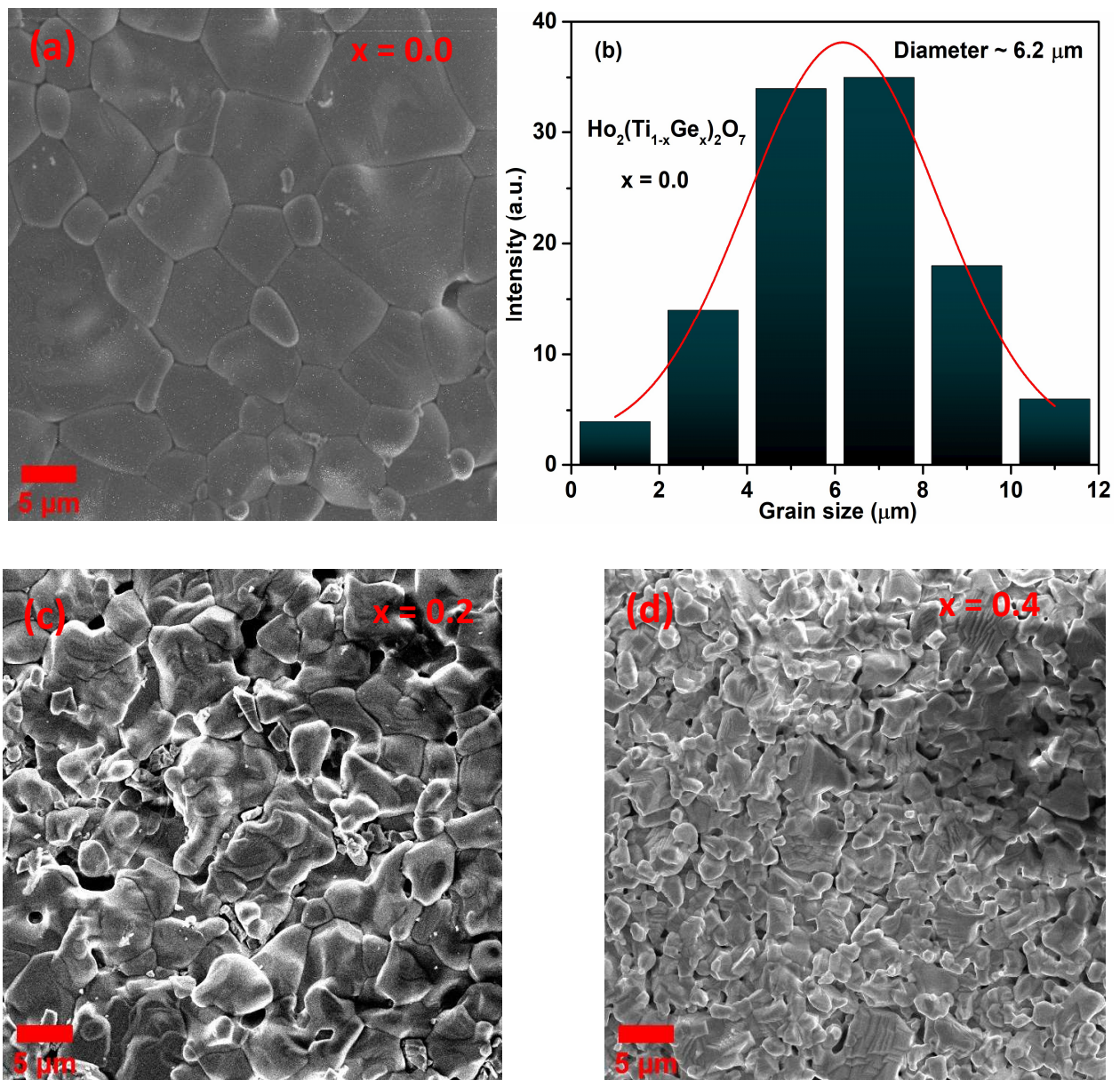


Fig. 3.6 SEM images of $\text{Ho}_2(\text{Ti}_{1-x}\text{Ge}_x)_2\text{O}_7$ samples (a) $x = 0.0$, (b) Grain size distribution (c) $x = 0.2$, and (d) $x = 0.4$.

This increasing value of average grain size or compact morphology depicts the increasing porosity of as-prepared samples on increasing x-value. The porosity of these samples was determined from the theoretical and experimental density as mentioned in following relation,

$$Porosity = \left[\frac{\text{theoretical density } (\rho_{th}) - \text{experimental density } (\rho_{ex})}{\text{theoretical density } (\rho_{th})} \times 100 \right] \% \dots \dots \dots (3.3)$$

and theoretical density was calculated through the following relation,

$$\begin{aligned} \text{Theoretical density } (\rho_{th}) \\ = \frac{8 \times 10^{18} \times M}{N_A(6.02 \times 10^{23}) \times a^3} \dots \dots \dots (3.4) \end{aligned}$$

Where M is the molecular weight in gram/mole and ‘a’ is the lattice parameter as reported in **Table 3.1**. The bulk density of all three as-prepared pellets were experimentally determined through density measurement kit coupled with electronic balance which is based on Archimedes’ principle. The obtained values of porosity, experimental bulk density, and grain size were reported in **Table 3.3**.

Table 3.3 The calculated values of theoretical density, experimental bulk density, and grain size for $Ho_2(Ti_{1-x}Ge_x)_2O_7$.

$Ho_2(Ti_{1-x}Ge_x)_2O_7$	Theoretical density (g/cm ³)	Experimental density (g/cm ³)	Porosity (%)	Grain size (μm)
x = 0.0	6.896	6.494	5.83	6.2 (2)
x = 0.2	7.069	6.587	6.82	4.9 (6)
x = 0.4	7.286	6.758	7.25	3.8 (9)

The decreasing trend in relative density or increasing porosity validates the decreasing values of grain size with increasing x value in $\text{Ho}_2(\text{Ti}_{1-x}\text{Ge}_x)_2\text{O}_7$. These results conclude that the composition majorly decides the surface morphology or grain evolving mechanism irrespective of sintering time and temperature.

3.3.4 Magnetization Investigations

To investigate the magnetic properties of HTGO compounds, temperature-dependent DC magnetic characterization has been carried out of all specimens using a vibrating sample magnetometer. **Fig. 3.7 (a)** shows the temperature dependent magnetic susceptibility of HTGO ($x = 0.4$) specimen in the temperature range of 2 K to 300 K recorded in the applied field of 1000 Oe. The Zero field cooled (ZFC) and field cooled (FC) exhibits overlapping of both curves and follow the paramagnetic behaviour in all specimens. This indicates that neither magnetic order nor spin glass type behaviour occurs in HTGO even on cooling down to 2 K. The temperature dependence of inverse magnetic susceptibility ($1/\chi$) of HTGO compounds are presented in the inset of **Fig. 3.7 (a)**. The observed graph shows the linear behaviour for all specimens and also follows the Curie Weiss law between 2 K to 300 K temperature range.

$$\chi = \frac{C}{T - \theta_{\text{CW}}} \dots \dots \dots (3.5)$$

where θ_{CW} is Curie-Weiss temperature and C is Curie-constant. The values of effective magnetic moment (μ_{eff}) are estimated using $C = \frac{N\mu_{\text{eff}}^2}{3K}$, where K is Boltzmann constant and N is Avogadro number [16]. The values of Curie-Weiss temperature (θ_{CW}) are derived using Curie Weiss constant C as shown in **Fig 3.7 (b)**. Parent and all doped compounds were found to have negative curie Weiss temperature. Also, it is observed that θ_{CW} decreases on increasing chemical pressure. Such data suggest that a dominating antiferromagnetic interaction between

the Ho-Ho spins. The experimentally calculated value of effective magnetic moment (μ_{eff}) fitted by equation (3.5) is recorded in **Fig. 3.7 (d)** which is consistent with the data earlier reported for this compound. The theoretical effective magnetic moment can be estimated using equation (3.6).

$$\text{Magnetic moment} = g\sqrt{J(J+1)}\mu_B \dots \dots \dots (3.6)$$

Here, g is Lande splitting factor which can be calculated using the relation:

$$g = 1 + \frac{J(J+1) + S(S+1) - L(L+1)}{2J(J+1)} \dots \dots \dots (3.7)$$

Here, J is the total quantum number which is the sum of the spin (S) and orbital quantum number (L). The values of L , S , and J for Ho^{3+} are 6, 2, and 8, respectively [43]. For Ho^{3+} the value of Lande g factor is 1.25 and the corresponding theoretical magnetic moment is $1.25\sqrt{8(8+1)}\mu_B = 10.6 \mu_B$. We observed that the theoretical value of $\mu_{\text{eff}}/\text{Ho}$ is greater than the experimental value calculated using Curie Weiss law, this indicates that robust correlation among the spins is apparently due to frustration [44]. Thus, used temperature range has a marked effect on the result obtained from Curie Weiss fitting. So, the data were also fitted between temperature range (2-20 K). The observed Curie Weiss temperatures (θ_{CW}) are shown in **Fig. 3.7 (c)**. Experimentally measured values of all magnetic parameters are shown in **Table 3.4**.

Table 3.4 Magnetic parameters calculated (experimentally) from curie Weiss law fitting for $\text{Ho}_2(\text{Ti}_{1-x}\text{Ge}_x)_2\text{O}_7$.

$\text{Ho}_2(\text{Ti}_{1-x}\text{Ge}_x)_2\text{O}_7$	Effective magnetic moment ($\mu_{\text{B/f.u}}$)	Curie Weiss (CW) temperature (2 - 20 K)	Curie Weiss (CW) temperature (100 - 300 K)
x = 0.0	4.31 ± 0.125	0.8519 ± 0.016	-6.875 ± 0.172
x = 0.2	4.14 ± 0.117	0.6535 ± 0.032	-7.698 ± 0.214
x = 0.4	3.43 ± 0.098	0.567 ± 0.012	-9.98 ± 0.145

Although effective magnetic moments are found almost the same in these two fittings (data from low-temperature fitting not shown) but positive value of θ_{CW} indicates ferromagnetic character which goes on decreasing with doping. In both (low and high temperature) fitted data, it was found that values of θ_{CW} are reduced with rise in the chemical pressure which is a clear indication of weakening of ferromagnetic interaction in all samples. The change in exchange and dipolar interaction between the Ho spins may result in such type of behavior. The energy barrier is shifted due to changes of crystal field level in the doped compounds [28]. Large crystal field splitting of the Ho^{3+} multiplets, which was not taken into consideration in the fitting procedure is associated with dependency of θ_{CW} on the fitting temperature. Based on the literature study, the reported Curie-Weiss temperature was found 1.0 K for $\text{Ho}_2\text{Ti}_2\text{O}_7$ [12, 27]. Hallas *et al.* reported the values of saturation magnetization ($5.0 \mu_{\text{B}}$) and Curie-Weiss temperature ($\theta_{\text{CW}} \sim 0.06$ K) for the $\text{Ho}_2\text{Ge}_2\text{O}_7$ compound [45]. Meanwhile, the values obtained in the current investigation lie in the range of 1.0 K to 0.06 K for $\text{Ho}_2(\text{Ti}_{1-x}\text{Ge}_x)_2\text{O}_7$ ($x = 0.0, 0.2, \text{ and } 0.4$), which indicates a good agreement with the published results.

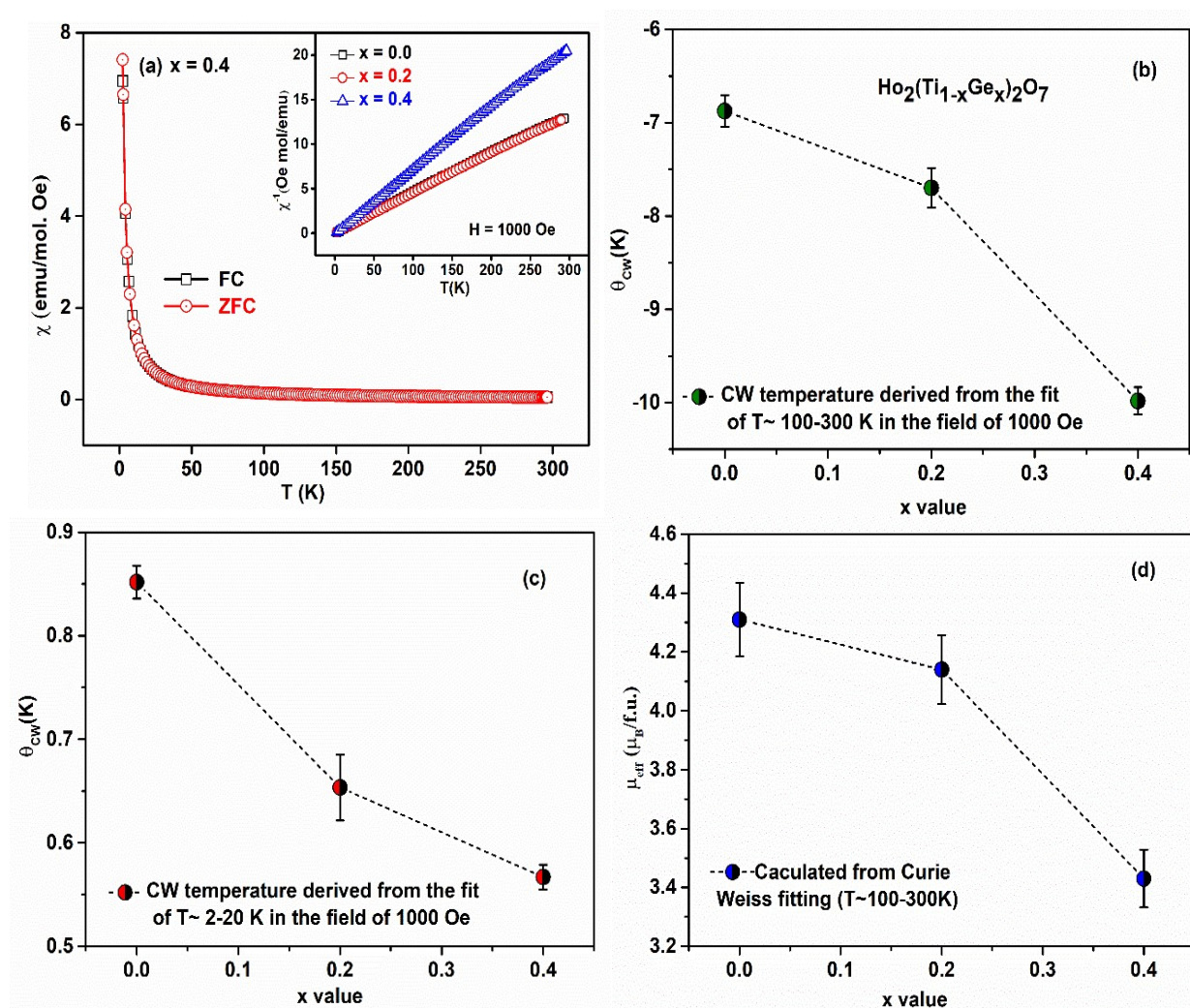


Fig. 3.7 (a) Variation of magnetic susceptibility (χ) vs temperature (T) of $\text{Ho}_2(\text{Ti}_{1-x}\text{Ge}_x)_2\text{O}_7$ ($x = 0.4$) sample (FC and ZFC curve). **Inset:** shows inverse DC magnetic susceptibility vs temperature of the $\text{HO}_2(\text{Ti}_{1-x}\text{Ge}_x)_2\text{O}_7$ ($x = 0.0, 0.2$ and 0.4) samples in the field of 1000 Oe. **(b)** Curie Weiss (CW) temperature obtained from the fitting at high temperature (100 – 300 K) range. **(c)** Curie Weiss (CW) temperature obtained from the fitting at low temperature (2 – 20 K) range. **(d)** The effective magnetic moment was calculated from Curie Weiss (CW) law at temperature range (100 – 300 K).

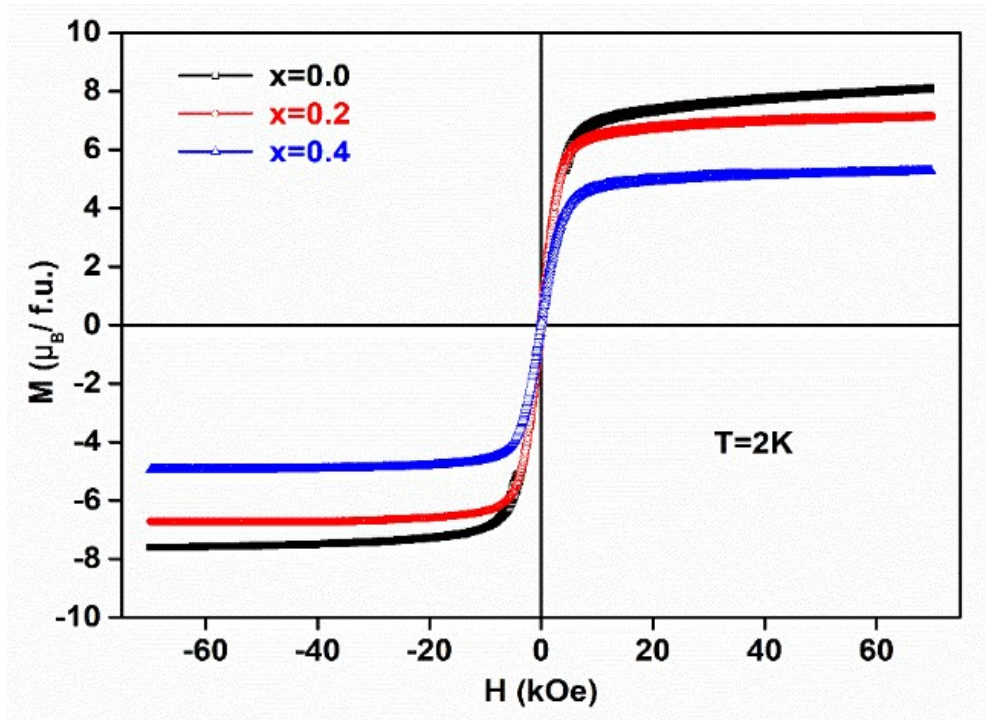


Fig. 3.8 The variation of magnetization (M) vs magnetic field (H) of $\text{Ho}_2(\text{Ti}_{1-x}\text{Ge}_x)_2\text{O}_7$ at 2K.

The M-H curves of $\text{HO}_2(\text{Ti}_{1-x}\text{Ge}_x)_2\text{O}_7$ samples recorded at 2 K are presented in **Fig. 3.8**. It can be seen that magnetization decrease with increasing Ge concentration. In these compounds, the 16d magnetic site is mainly responsible for magnetization, while 16c non-magnetic site is also contributing to magnetization. As the number of Ho (magnetic) ions are fixed at the 16d site for each compound, this indicates that nonmagnetic 16c Wyckoff sites are the main reason behind decrease in saturation magnetization [46]. The experimentally calculated value of saturation magnetization (M_{sat}) for the parent compound was found to be $7.84 \mu_{\text{B}/\text{Ho}^{3+}}$ which decreases to $7.06 \mu_{\text{B}/\text{Ho}^{3+}}$ and $5.11 \mu_{\text{B}/\text{Ho}^{3+}}$ after doping the sample with germanium for $x=0.2$ and 0.4 , respectively. This confirms that doping tends to weaken the ferromagnetic interaction, which is consistent with the data of χ^{-1} versus temperature curve. The obtained values of the

magnetic moment are lesser than theoretical values of holmium ($10\mu_B$) due to the single-ion anisotropy and powder angular averaging effect [35].

3.4 Conclusion

In this chapter, structural and magnetic properties of Ge doped pyrochlore titanate $\text{Ho}_2(\text{Ti}_{1-x}\text{Ge}_x)_2\text{O}_7$ prepared using solid state reaction route is described. Structural analysis confirmed formation of impurity free cubic type pyrochlore crystal structure with lattice constant decreases constantly and follows Vegard's law. Raman spectroscopy study further confirmed pyrochlore phase with hardening of phonon mode due to phonon-phonon anharmonic interaction. Crystallite size is being reduced from 94 nm to 54 nm as on increasing x value. The SEM micrographs shows a compact nature of spherical grains having grain size of the order of $\sim 6.2 \mu\text{m}$, $\sim 4.9 \mu\text{m}$ and $\sim 3.8 \mu\text{m}$ with increasing Ge- concentration. With x value this decreasing trend of grain size is correlated with decreasing relative density or increasing porosity of the as-prepared samples. The magnetic studies conclude ferromagnetic (FM) interaction in the doped compound is smaller than of pure $\text{Ho}_2\text{Ti}_2\text{O}_7$, resulting in change of exchange and dipolar interaction. The result also reveals a shift in the energy barrier due to changes of crystal field level in the doped compounds. The nonmagnetic 16c site was found to be responsible for decrease in magnetization. On the other hand, an increment in radii ratio (R_A/R_B) or variation in O_{48f} oxygen with increase in Ge content over Ti confirmed the enhancement in the pyrochlore superstructural ordering with increase in the x-value of $\text{Ho}_2(\text{Ti}_{1-x}\text{Ge}_x)_2\text{O}_7$. Thus, highly stable pyrochlore structured compositions exhibit less ferromagnetic tendency. Furthermore, spin glass-like behaviour in $\text{Ho}_2(\text{Ti}_{1-x}\text{Ge}_x)_2\text{O}_7$ was not detected even on cooling down to 2 K in all compositions.

References

1. Fritsch, K., K. A. Ross, Y. Qiu, J. R. D. Copley, T. Guidi, R. I. Bewley, H. A. Dabkowska, and B. D. Gaulin. "Antiferromagnetic spin ice correlations at $(1/2, 1/2, 1/2)$ in the ground state of the pyrochlore magnet $Tb_2Ti_2O_7$." *Physical Review B* 87, no. 9 (2013): 094410.
2. Morris, David Jonathan Pryce, D. A. Tennant, S. A. Grigera, B. Klemke, C. Castelnovo, R. Moessner, C. Czternasty et al. "Dirac strings and magnetic monopoles in the spin ice $Dy_2Ti_2O_7$." *Science* 326, no. 5951 (2009): 411-414.
3. Balents, Leon. "Spin liquids in frustrated magnets." *Nature* 464, no. 7286 (2010): 199-208.
4. Binder, Kurt, and A. Peter Young. "Spin glasses: Experimental facts, theoretical concepts, and open questions." *Reviews of Modern physics* 58, no. 4 (1986): 801.
5. Bramwell, Steven T., and Michel JP Gingras. "Spin ice state in frustrated magnetic pyrochlore materials." *Science* 294, no. 5546 (2001): 1495-1501.
6. Snyder, J., J. S. Slusky, R. J. Cava, and P. Schiffer. "How 'spin ice' freezes." *Nature* 413, no. 6851 (2001): 48-51.
7. Shlyakhtina, A. V., and L. G. Shcherbakova. "New solid electrolytes of the pyrochlore family." *Russian Journal of Electrochemistry* 48, no. 1 (2012): 1-25.
8. Sharma, Saurabh Kumar, V. Grover, A. K. Tyagi, D. K. Avasthi, U. B. Singh, and P. K. Kulriya. "Probing the temperature effects in the radiation stability of $Nd_2Zr_2O_7$ pyrochlore under swift ion irradiation." *Materialia* 6 (2019): 100317.

9. Sharma, S. K., V. Grover, R. Shukla, A. Hussain, A. Mishra, R. C. Meena, and P. K. Kulriya. "Evidence of improved tolerance to electronic excitation in nanostructured $\text{Nd}_2\text{Zr}_2\text{O}_7$." *Journal of Applied Physics* 129, no. 11 (2021): 115902.
10. Kumar, A., P. K. Kulriya, S. K. Sharma, V. Grover, A. K. Tyagi, and V. K. Shukla. "Structural and compositional effects on the electronic excitation induced phase transformations in $\text{Gd}_2\text{Ti}_{2-y}\text{Zr}_y\text{O}_7$ pyrochlore." *Journal of Nuclear Materials* 539 (2020): 152278.
11. Oh, Si Hyoung, Robert Black, Ekaterina Pomerantseva, Jin-Hyon Lee, and Linda F. Nazar. "Synthesis of a metallic mesoporous pyrochlore as a catalyst for lithium– O_2 batteries." *Nature chemistry* 4, no. 12 (2012): 1004-1010.
12. Gardner, Jason S., Michel JP Gingras, and John E. Greedan. "Magnetic pyrochlore oxides." *Reviews of Modern Physics* 82, no. 1 (2010): 53.
13. Pal, Arkadeb, Abhishek Singh, A. K. Ghosh, and Sandip Chatterjee. "High-temperature spin-freezing transition in pyrochlore $\text{Eu}_2\text{Ti}_2\text{O}_7$: A new observation from ac-susceptibility." *Journal of Magnetism and Magnetic Materials* 462 (2018): 1-7.
14. Yadav, Pramod Kumar, Pappu Kumar Harijan, Abhishek Tripathi, and Chandan Upadhyay. "Effect of A-site Fe substitution on the magnetic behavior of $\text{Dy}_2\text{Ti}_2\text{O}_7$ spin ice." *Journal of Magnetism and Magnetic Materials* 481 (2019): 221-226.
15. Sharma, Saurabh K., Hari S. Mohanty, Dillip K. Pradhan, Ajay Kumar, Vivek K. Shukla, Fouran Singh, and Pawan K. Kulriya. "Structural, dielectric and electrical properties of pyrochlore-type $\text{Gd}_2\text{Zr}_2\text{O}_7$ ceramic." *Journal of Materials Science: Materials in Electronics* 31, no. 24 (2020): 21959-21970.
16. Liu, Hui, Youming Zou, Lei Zhang, Langsheng Ling, Hongyan Yu, Lei He, Changjin Zhang, and Yuheng Zhang. "Magnetic order and dynamical properties of the spin-

17. frustrated magnet $Dy_{2-x}Yb_xTi_2O_7$." *Journal of magnetism and magnetic materials* 349 (2014): 173-179.
18. Marques, M. D. R., F. S. Portela, A. A. M. Oliveira, PetrucioBarrozo, N. O. Moreno, P. C. A. Brito, and J. Albino Aguiar. "Structural and magnetic properties of pyrochlores $Gd_{2-x}M_xRu_2O_7$ (M= Ho, Y)." *Physica B: Condensed Matter* 407, no. 16 (2012): 3106-3108.
19. Clancy, J. P., J. P. C. Ruff, S. R. Dunsiger, Y. Zhao, H. A. Dabkowska, J. S. Gardner, Y. Qiu, J. R. D. Copley, T. Jenkins, and B. D. Gaulin. "Revisiting static and dynamic spin-ice correlations in $Ho_2Ti_2O_7$ with neutron scattering." *Physical Review B* 79, no. 1 (2009): 014408.
20. Panghal, Asha, Yogendra Kumar, P. K. Kulriya, Parasharam M. Shirage, and N. L. Singh. "Atomic order-disorder engineering in the $La_2Zr_2O_7$ pyrochlore under low energy ion irradiation." *Ceramics International* 47, no. 14 (2021): 20248-20259.
21. Ehlers, G., A. L. Cornelius, T. Fennell, M. Koza, S. T. Bramwell, and J. S. Gardner. "Evidence for two distinct spin relaxation mechanisms in 'hot 'spin ice $Ho_2Ti_2O_7$." *Journal of Physics: Condensed Matter* 16, no. 11 (2004): S635.
22. Snyder, J., B. G. Ueland, J. S. Slusky, H. Karunadasa, Robert Joseph Cava, Ari Mizel, and P. Schiffer. "Quantum-Classical Reentrant Relaxation Crossover in $Dy_2Ti_2O_7$ Spin Ice." *Physical review letters* 91, no. 10 (2003): 107201.
23. Gardner, J. S., A. Keren, G. Ehlers, C. Stock, Eva Segal, J. M. Roper, B. Fåk et al. "Dynamic frustrated magnetism in $Tb_2Ti_2O_7$ at 50 mK." *Physical Review B* 68, no. 18 (2003): 180401.

24. Bramwell, S. T., M. J. Harris, B. C. Den Hertog, M. J. P. Gingras, J. S. Gardner, D. F. McMorrow, A. R. Wildes et al. "Spin correlations in $\text{Ho}_2\text{Ti}_2\text{O}_7$: a dipolar spin ice system." *Physical Review Letters* 87, no. 4 (2001): 047205.
25. Fennell, Tom, P. P. Deen, A. R. Wildes, K. Schmalzl, D. Prabhakaran, A. T. Boothroyd, R. J. Aldus, D. F. McMorrow, and S. T. Bramwell. "Magnetic Coulomb phase in the spin ice $\text{Ho}_2\text{Ti}_2\text{O}_7$." *Science* 326, no. 5951 (2009): 415-417.
26. Xie, Y. L., L. Lin, Z. B. Yan, and J-M. Liu. "Magnetic phase transitions and monopole excitations in spin ice under uniaxial pressure: A Monte Carlo simulation." *Journal of applied physics* 117, no. 17 (2015): 17C714.
27. den Hertog, Byron C., and Michel JP Gingras. "Dipolar interactions and origin of spin ice in Ising pyrochlore magnets." *Physical review letters* 84, no. 15 (2000): 3430.
28. Cornelius, A. L., and J. S. Gardner. "Short-range magnetic interactions in the spin-ice compound $\text{Ho}_2\text{Ti}_2\text{O}_7$." *Physical Review B* 64, no. 6 (2001): 060406.
29. Liu, Hui, Jian Bian, Shiyun Chen, Yuan Feng, Yu Xie, and Baolong Fang. "Magnetic and dynamical properties in the diluted spin ice $\text{Dy}_{2-x}\text{La}_x\text{Ti}_2\text{O}_7$." *Journal of Magnetism and Magnetic Materials* 465 (2018): 316-322.
30. Nemytova, O. V., I. V. Piir, M. S. Koroleva, D. V. Perov, and A. B. Rinkevich. "Magnetic properties of nanocomposite and bulk rare earth titanates $\text{Ho}_2\text{Ti}_2\text{O}_7$ and $\text{Yb}_2\text{Ti}_2\text{O}_7$." *Journal of Magnetism and Magnetic Materials* 494 (2020): 165800.
31. Morosan, E., J. A. Fleitman, Q. Huang, J. W. Lynn, Y. Chen, X. Ke, M. L. Dahlberg, P. Schiffer, C. R. Craley, and R. J. Cava. "Structure and magnetic properties of the $\text{Ho}_2\text{Ge}_2\text{O}_7$ pyrogermanate." *Physical Review B* 77, no. 22 (2008): 224423.

32. Lin, L., Y. L. Xie, Z. Y. Zhao, J. J. Wen, Z. B. Yan, S. Dong, and J-M. Liu. "Enhanced magnetism-generated ferroelectricity in highly frustrated Fe-doped $\text{Ho}_2\text{Ti}_2\text{O}_7$." *Journal of Applied Physics* 117, no. 17 (2015): 17D915.
33. Playford, Helen Y., Craig L. Bull, Matthew G. Tucker, Nicholas P. Funnell, Christopher J. Ridley, Kenneth P. Marshall, and Richard I. Walton. "In situ neutron diffraction study of the formation of $\text{Ho}_2\text{Ge}_2\text{O}_7$ pyrochlore at high temperature and pressure." *Dalton Transactions* 46, no. 44 (2017): 15415-15423.
34. Panghal, Asha, Yogendra Kumar, P. K. Kulriya, Parasharam M. Shirage, and N. L. Singh. "Structural assessment and irradiation response of $\text{La}_2\text{Zr}_2\text{O}_7$ pyrochlore: Impact of irradiation temperature and ion fluence." *Journal of Alloys and Compounds* 862 (2021): 158556.
35. Rodríguez-Carvajal, Juan. "Recent advances in magnetic structure determination by neutron powder diffraction." *Physica B: Condensed Matter* 192, no. 1-2 (1993): 55-69.
36. Singh, Prajyoti, Arkadeb Pal, Vinod K. Gangwar, Prince K. Gupta, MohdAlam, Surajit Ghosh, R. K. Singh, A. K. Ghosh, and Sandip Chatterjee. "Wasp–Waisted loop and spin frustration in $\text{Dy}_{2-x}\text{Eu}_x\text{Ti}_2\text{O}_7$ pyrochlore." *J. of Magnetism and Magnetic Materials* 518 (2021): 167364.
37. Kumari, Renu, P. K. Kulriya, V. Grover, R. Shukla, K. Saravanan, S. Mohapatra, A. K. Tyagi, and D. K. Avasthi. "Radiation stability of $\text{Gd}_2\text{Zr}_2\text{O}_7$: effect of stoichiometry and structure." *Ceramics International* 42, no. 1 (2016): 103-109.
38. Chang, L. J., W. Schweika, Y-J. Kao, Y. Z. Chou, J. Perbon, Th Brückel, Hong-Chang Yang, Y. Y. Chen, and J. S. Gardner. "Magnetic correlations in $\text{Ho}_x\text{Tb}_{2-x}\text{Ti}_2\text{O}_7$." *Physical Review B* 83, no. 14 (2011): 144413.

39. Glerup, Marianne, Ole Faurskov Nielsen, and Finn Willy Poulsen. "The structural transformation from the pyrochlore structure, $A_2B_2O_7$, to the fluorite structure, AO_2 , studied by Raman spectroscopy and defect chemistry modeling." *Journal of Solid-State Chemistry* 160, no. 1 (2001): 25-32.
40. Kumar, Ajay, Saurabh Kumar Sharma, V. Grover, Yogendar Singh, Vivek Kumar, Vivek Kumar Shukla, and P. K. Kulriya. "Probing the Short-Range Ordering of Ion Irradiated $Gd_2Ti_{2-y}Zr_yO_7$ ($0.0 \leq y \leq 2.0$) Pyrochlore under Electronic Stopping Regime." *Journal of Nuclear Materials* (2022): 153682.
41. Saha, Surajit, Surjeet Singh, BrahimDkhil, S. Dhar, R. Suryanarayanan, G. Dhahenne, A. Revcolevschi, and A. K. Sood. "Temperature-dependent Raman and X-ray studies of the spin-ice pyrochlore $Dy_2Ti_2O_7$ and nonmagnetic pyrochlore $Lu_2Ti_2O_7$." *Physical Review B* 78, no. 21 (2008): 214102.
42. Mączka, M., M. L. Sanjuán, A. F. Fuentes, L. Macalik, J. Hanuza, K. Matsuhira, and Z. Hiroi. "Temperature-dependent studies of the geometrically frustrated pyrochlores $Ho_2Ti_2O_7$ and $Dy_2Ti_2O_7$." *Physical Review B* 79, no. 21 (2009): 214437.
43. Ross, K. A., Th Proffen, H. A. Dabkowska, J. A. Quilliam, L. R. Yaraskavitch, J. B. Kycia, and B. D. Gaulin. "Lightly stuffed pyrochlore structure of single-crystalline $Yb_2Ti_2O_7$ grown by the optical floating zone technique." *Physical Review B* 86, no. 17 (2012): 174424.
44. Kittel, C.: Introduction to solid state physics, 7thedn. Wiley, New Delhi (1995)
45. Liu, Hui, Youming Zou, Langsheng Ling, Lei Zhang, Changjin Zhang, and Yuheng Zhang. "Enhanced ferromagnetism and emergence of spin-glass-like transition in pyrochlore compound $Dy_2Ti_{2-x}V_xO_7$." *Journal of Magnetism and Magnetic Materials* 388 (2015): 135-142.

46. Hallas, A. M., J. A. M. Paddison, H. J. Silverstein, A. L. Goodwin, J. R. Stewart, A. R. Wildes, J. G. Cheng et al. "Statics and dynamics of the highly correlated spin ice $\text{Ho}_2\text{Ge}_2\text{O}_7$." *Physical Review B* 86, no. 13 (2012): 134431.
47. Yadav, Pramod K., Pinki Singh, Manjari Shukla, Soma Banik, and Chandan Upadhyay. "Effect of B-site substitution on structural, magnetic and optical properties of $\text{Ho}_2\text{Ti}_2\text{O}_7$ pyrochlore oxide." *Journal of Physics and Chemistry of Solids* 138 (2020): 109267.

Chapter 4

Effect of La^{3+} Substitution on Structural and Magnetic Properties of Frustrated $\text{Ho}_2\text{Ti}_2\text{O}_7$ Pyrochlore

In this chapter, magnetic and structural behaviour of $\text{Ho}_{2-x}\text{La}_x\text{Ti}_2\text{O}_7$ ($x = 0.0, 0.1, \text{ and } 0.2$) pyrochlore prepared through solid state standard method, were investigated by partial replacement of Ho^{3+} with nonmagnetic La^{3+} . Describe how A-site nonmagnetic doping affected the structural and magnetic results. A renowned quantum material $\text{Ho}_2\text{Ti}_2\text{O}_7$ in which structural and magnetic properties are coupled, is distinguished by its unusual spin freeze state. It was observed that Curie Weiss temperature (θ_{CW}) and effective magnetic moment (μ_{eff}) shrinking with rising chemical pressure leads to weakening of ferromagnetic character of the compounds. In terms of regulating the magnetism, it was discovered that B site doping is more effective than A site.

4.1 Introduction

The geometric frustration with the corner-sharing tetrahedron system in materials has drawn a lot of scientific attention to the magnetic pyrochlore oxides over the past many years. [1-7]. $\text{Ho}_2\text{Ti}_2\text{O}_7$, a well-known quantum material with associated structural and magnetic properties, stands out for its peculiar spin freeze state [8-13]. We studied the smaller cation germanium doping at the B site of $\text{Ho}_2\text{Ti}_2\text{O}_7$ pyrochlore in Chapter 3rd, and it was discovered that an increase in the amount of Ge (B site) results in a decrease in the ferromagnetic nature of the doped compounds. $\text{Ho}_2\text{Ti}_2\text{O}_7$ has a ferromagnetic Curie Weiss temperature (θ_{CW}) order of ~ 1.0 K which proves its large spin ice behaviour [14]. Marque *et al.* reported θ_{CW} for $\text{Ho}_2\text{Ru}_2\text{O}_7$ and $\text{Gd}_2\text{Ru}_2\text{O}_7$ are +1.12 K and -11.77 K, respectively [15] that depends upon the pyrochlore compositions. $\text{Dy}_2\text{Ti}_2\text{O}_7$ was found to have positive value of $\theta_{\text{CW}} \sim 1.0$ K [16] whereas $\text{Eu}_2\text{Ti}_2\text{O}_7$ [17] and $\text{Yb}_2\text{Ti}_2\text{O}_7$ [18] have shown negative θ_{CW} of -1.35 K and -0.8 K, respectively due to antiferromagnetic interactions. Recently, we have reported reduction in θ_{CW} from 0.86 K to 0.57 K by doping of the smaller size cation Ge^{4+} at the Ti^{4+} site in $\text{Ho}_2(\text{Ti}_{1-x}\text{Ge}_x)_2\text{O}_7$ ($x = 0.0, 0.2$ and 0.4) [19]. Thus, dilution is a vital tool that can validate the complex behavior of magnetic correlation and spin relaxation process. In the dilution process, magnetic ions (Dy and Ho) can be substituted with non-magnetic (Lu^{3+} , Y^{3+} and La^{3+}) ions [20-21]. The larger La^{3+} ions carry more strain and chemical pressure as compared to Lu and Y. The thermodynamic properties of La doped $\text{Ho}_2\text{Ti}_2\text{O}_7$ were studied by Kajanakova *et al.* [22] and dynamic spins correlations behavior of HLTO pyrochlore had been observed by Ehlers *et al.* in 2008 [23]. To the best of our knowledge, structural and magnetic correlation in La^{3+} doped $\text{Ho}_2\text{Ti}_2\text{O}_7$ pyrochlore system has been not investigated. It is very fascinating to examine the chemical pressure effect on structural and magnetic performance of these pyrochlore. These ingredients would play a

crucial role for not only understanding the behavior of frustrated materials but also important for probing the characteristic of magnetic ground state.

In current chapter, the correlation of the structural and magnetic characteristics of $\text{Ho}_{2-x}\text{La}_x\text{Ti}_2\text{O}_7$ (HLTO) pyrochlore is investigated. Structural ordering of the pyrochlore oxides was increased with La doping in the parent compound. Raman active mode associated with A cations shows red shift while the modes associated with B- cations displayed blue shift. No spin glassy pattern was traced in magnetic studies even letting down the temperature up to 2 K. Ferromagnetic character was found to decrease with increase in ionic radii ratio of HLTO compounds. Thus, more ordered pyrochlore structured composition shows a weaker ferromagnetic nature. In comparison with the prior studies, the magnetic study suggest that A site doping is less sensitive than B site doping for controlling magnetic properties.

4.2 Synthesis and Characterization

Solid-state technique was employed to prepare $\text{Ho}_{2-x}\text{La}_x\text{Ti}_2\text{O}_7$ ($x = 0.0, 0.1$ and 0.2) pyrochlore [24-25] by using high purity (>99.99%) precursors of Ho_2O_3 , TiO_2 , and La_2O_3 purchased by Sigma Aldrich. All ingredients were taken in stoichiometric percentage and homogenously mashed and thoroughly ground for 10 hrs in high energy ball mill system with ethanol as mixing medium. During the milling, an interval of 45 minutes is kept between two consecutive grinding to avoid the excessive heating caused undesirable effects in the powders. Powdered materials were pelletized into a cylindrical shape pellet having diameter of 8.0 millimetres and thickness of 1.0 millimetres. The prepared materials of all specimens were sintered at 1300°C (24 hrs) in the air ambient using muffle furnace. Again, the processes of grinding and palletizing were repeated followed by calcination at 1350°C for 24 hrs. Details of the synthesis process are shown in **Fig. 4.1**.

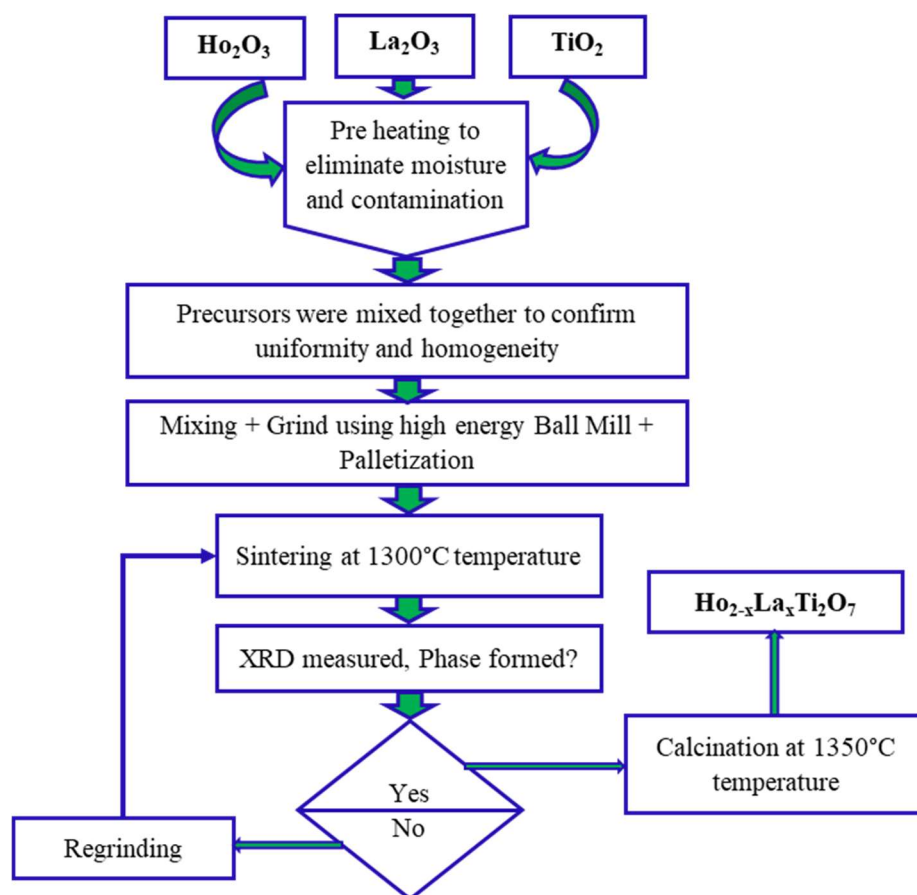


Fig. 4.1 Flowchart displays the detailed synthesis process of $Ho_{2-x}La_xTi_2O_7$.

XRD data was recorded using Bruker D8 advanced X-ray diffractometer between the range of 10° to 80° with 0.02° increment using scanning rate of $2^\circ/\text{min}$ [26]. Obtained XRD data was fitted by Rietveld refinement Fullprof program [27]. Surface morphology of as-synthesized pyrochlore was considered using SEM. The JSM-IT 200 model of JEOL-SEM setup, which has a tungsten-based electron gun operated at 30 kV, was used to conduct the SEM experiments. Raman spectroscopy (WiTec alpha 300 RA system with Nd: YAG laser of 532 nm) was used to investigate the phonon anharmonicity and structural ordering in the range of $100 - 800 \text{ cm}^{-1}$ at 300 K. EDX spectrometer setup was used to find concentration of as-prepared specimen. Magnetic measurement (DC) of each sample has been carried out at low temperature

using physical properties measurement system (cryogenics limited factory-made). During measurement, the functional magnetic field changed from -70 kOe and +70 kOe. Self-calibrating and integrated system (AC CY224C Aczet Pvt. Ltd) with 220 g maximum weight limit and 0.001 g readability is used to quantify density of the as-prepared samples.

4.3 Results and Discussions

4.3.1 Stability and Structural Investigation *via* XRD

The ionic radius ratio plays important role to determine the stability of pyrochlore structured ceramic. Ionic radius of Ho^{3+} , La^{3+} and Ti^{4+} ions (1.015Å, 1.162Å & 0.605Å, respectively) were used to calculate the stability factor. The stability factor of $\text{Ho}_{2-x}\text{La}_x\text{Ti}_2\text{O}_7$ specimen was estimated using equation (4.1) [28].

$$\frac{R_{(Ho/La)}}{R_{(Ti)}} = \frac{xR(La^{3+}) + (2 - x)R(Ho^{3+})}{R(Ti^{4+})} \dots \dots \dots (4.1)$$

A stable pyrochlore oxide structure is formed if ionic radii ratio lies in the range of $1.46 \leq RR \leq 1.78$ [29]. Calculated values of ionic radii ratio of HLTO compounds were found to be 1.68, 1.69 and 1.70 for $\text{Ho}_2\text{Ti}_2\text{O}_7$, $\text{Ho}_{1.9}\text{La}_{0.1}\text{Ti}_2\text{O}_7$, and $\text{Ho}_{1.8}\text{La}_{0.2}\text{Ti}_2\text{O}_7$, respectively which show that these compositions can be easily stabilized with pyrochlore symmetry. The ionic radii ratio increases linearly with increasing concentration of La content in HLTO samples resulting in an increment in the ordering of pyrochlore structure. These three samples ($x = 0.0$, 0.1 , and 0.2) were all discovered to be single phases free of any contaminants. Furthermore, we have also synthesized samples with $x = 0.3$ and 0.4 . Although ($x = 0.3$ and 0.4) samples had minimal contaminants as well as no single phase but their ionic radii ratios (1.72 and 1.74)

were found to lie in the stability range (1.46 to 1.78). **Fig. 4.2** displays the XRD data for the $x = 0.3$ and 0.4 specimens did not reveal the desired pyrochlore peaks. Few contaminated peaks are labelled by asterisk (**Fig. 4.2**). Therefore, magnetic studies have not been conducted on these samples.

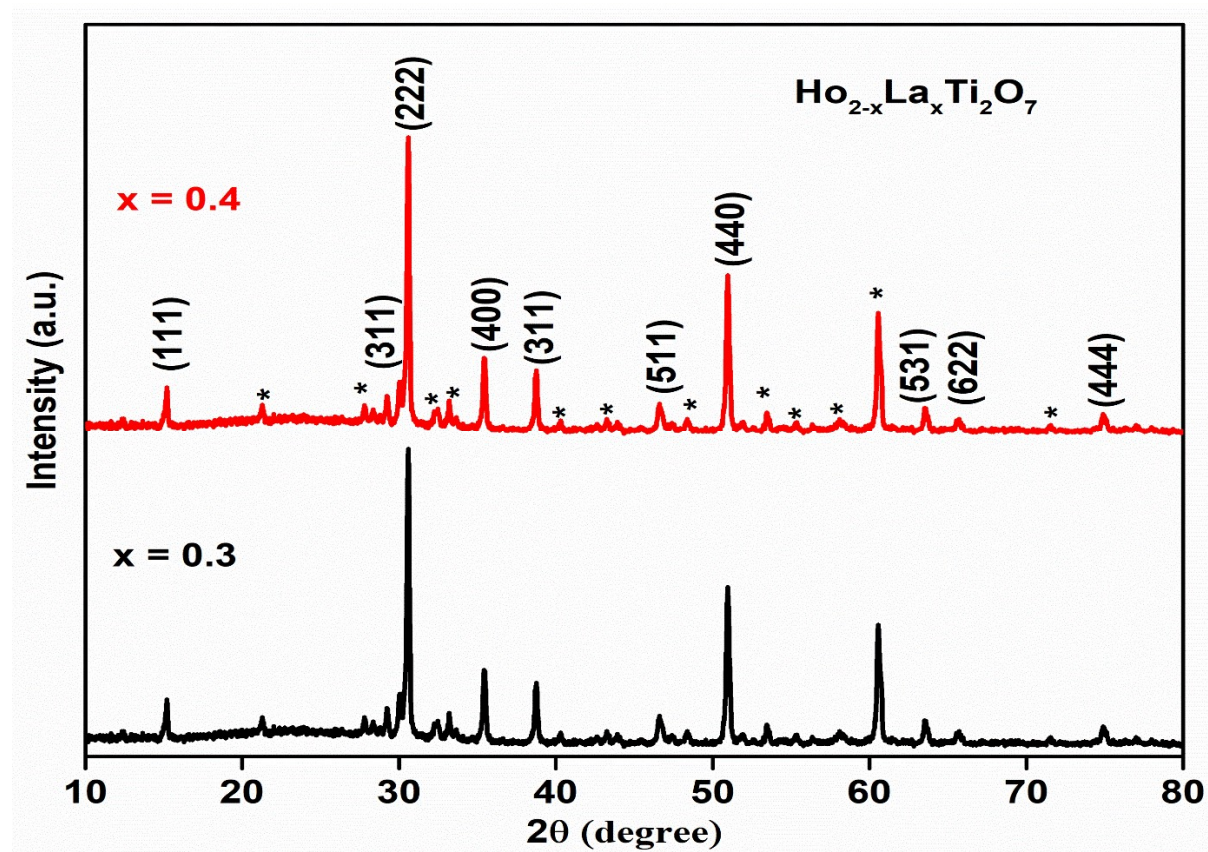


Fig. 4.2 XRD pattern of $\text{Ho}_{2-x}\text{La}_x\text{Ti}_2\text{O}_7$ with $x = 0.3$ and 0.4 . Single phase is not observed for these compositions. Contaminated peaks are marked by asterisk.

Structural analysis of the as-prepared compound is investigated by fitting the diffraction patterns on the basis of Fd-3m atomic positions using Rietveld refinement. **Fig. 4.3** shows the refined XRD data of (a) $\text{Ho}_2\text{Ti}_2\text{O}_7$, (b) $\text{Ho}_{1.9}\text{La}_{0.1}\text{Ti}_2\text{O}_7$, and (c) $\text{Ho}_{1.8}\text{La}_{0.2}\text{Ti}_2\text{O}_7$. The XRD data of each composition of HLTO series ($x = 0.0, 0.1, \text{ and } 0.2$) approves the space group of Fd-3m with impurity free single phase pyrochlore structure. The refinement process has been

performed in two steps using Fullprof-2005 software. In the first step, Le Bail refinement was performed which includes the refinement of background, scale factor, cell parameters, and peak shape parameters. The background was approximated with linear interpolation method by selecting several background points. A pseudo-Voigt function as an integration of Gaussian and Lorentzian profiles was used to model XRD peaks. In the second step, Rietveld refinement has been performed that involves the refinement of atomic coordinates (x parameter of 48f oxygen) with their occupancies. The refined parameters of HLTO series are displayed in **Table 4.1**.

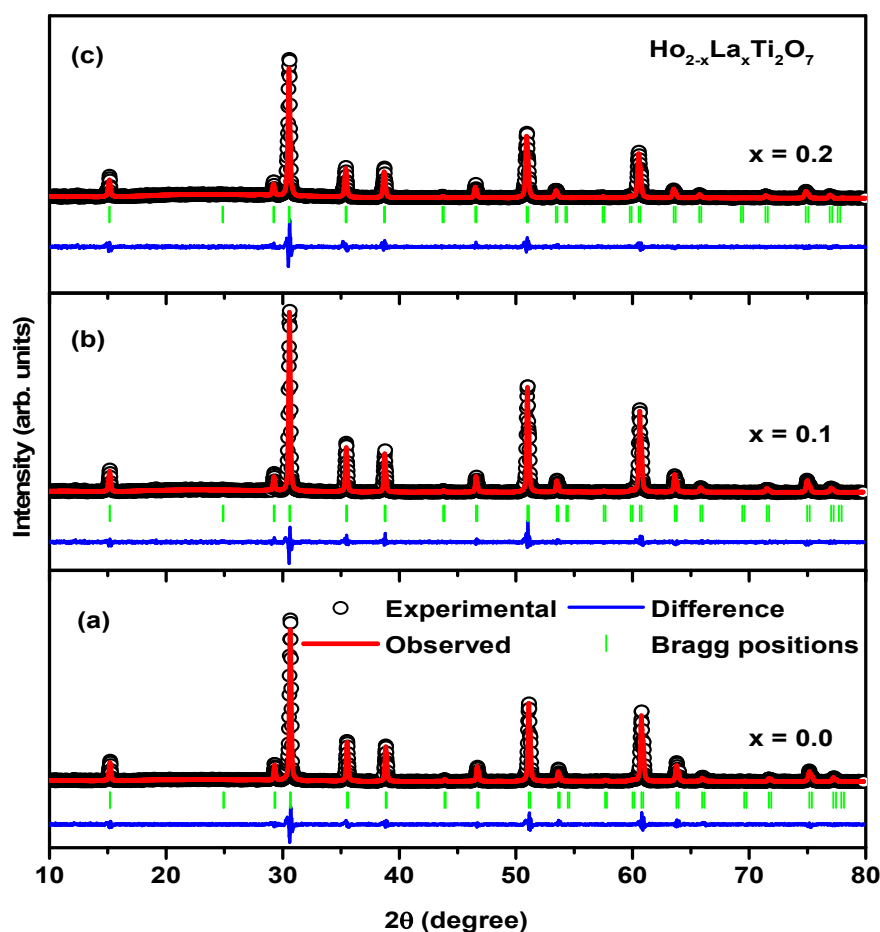


Fig. 4.3 Refined XRD profiles for (a) $\text{Ho}_2\text{Ti}_2\text{O}_7$, (b) $\text{Ho}_{1.9}\text{La}_{0.1}\text{Ti}_2\text{O}_7$, and (c) $\text{Ho}_{1.8}\text{La}_{0.2}\text{Ti}_2\text{O}_7$.

Since XRD data of pyrochlore involves two types of diffraction maxima. For $\text{Ho}_2\text{Ti}_2\text{O}_7$, high-intensity peaks belonging to even miller indices (222), (400), (440), (622), (444) and (800) located at $2\theta = 30.82^\circ, 35.69^\circ, 51.29^\circ, 60.96^\circ, 63.28^\circ,$ and 70.38° , respectively. Face centred cubic framework of both anions give rise to these high-intensity peaks.

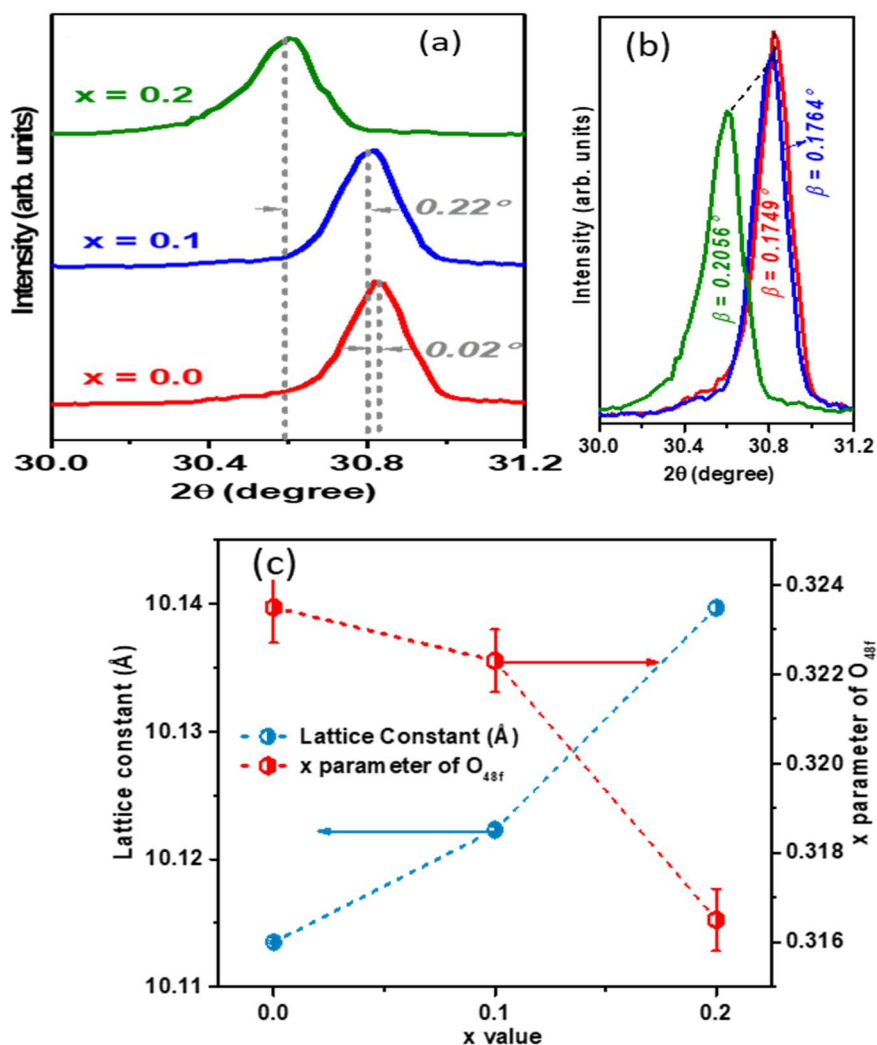


Fig. 4.4 An enlarged view of (222) planes for a variation in (a) peak position, (b) peak intensity with x value, and (c) lattice constant as well as a parameter of O_{48f} as a doping concentration of La in $\text{Ho}_{2-x}\text{La}_x\text{Ti}_2\text{O}_7$.

Moreover, the low intensity XRD peaks assigned to odd miller indices (111), (311), (331), (511), and (531) detected at $2\theta = 15.36^\circ$, 29.48° , 39.01° , 46.85° , and 53.4° , respectively attributed to the cationic size difference and anionic vacancy. Thus, the ordered pyrochlore superstructure (Fd-3m) comprises these two types of peaks and have three different oxygen Wyckoff positions surrounded by three different kinds of cationic arrangements [23, 30]. With the doping of La cation over Ho, the diffraction pattern is shifted towards lower 2θ values with nonmagnetic La doping as shown in **Fig. 4.4 (a)**. With respect to $x = 0$, the XRD profile of $\text{Ho}_{1.9}\text{La}_{0.1}\text{Ti}_2\text{O}_7$ shows a shifting of $\Delta\theta \approx 0.02^\circ$ which is further drastically increased as $\Delta\theta \approx 0.22^\circ$ on accommodating more La cation in $\text{Ho}_{1.8}\text{La}_{0.2}\text{Ti}_2\text{O}_7$ that is consist with earlier report on pyrochlore structured ceramic [30]. In addition to peak shifting, peak intensity also decreases on increasing x value as shown in **Fig. 4.4 (b)**. From the Rietveld refinement analysis, it is found that the lattice constant increases on increasing La doping. It must be noted that an increase in cell parameters with La doping at A-site leads to shift in the peak to lower 2θ values because ionic radius of La (1.162\AA) is larger than that of Ho (1.015\AA). As compared to $x = 0$, the composition with $x = 0.1$ shows a 0.09% increment in lattice constant which is further consecutively increased to 0.17% for the composition $x = 0.2$. It must be noted that the cell parameter is not increasing in a linear manner with respect to La doping at A-site as depicted in **Fig. 4.4 (c)**. Consequently, the incorporation of comparatively more ions in the lattice (cationic) is as per Vegard law [31]. In addition to R_A/R_B ratio, the strength of pyrochlore superstructure is characterized by displacement of x parameter of O_{48f} . The structure with x parameter of O_{48f} close to 0.3125 is identified as more ordered pyrochlore structure [6]. The x parameter of O_{48f} decreases on increasing La content at the place of Ho which exhibits increase in the strength of pyrochlore structure. The structural parameters; crystallite size and microstrain were estimated through Williamson-Hall (W-H) formalism as a linear fitting of the

data points of $\beta. \cos(\theta)$ as a function of $4. \sin(\theta)$. Seven peaks associated with (311), (222), (400), (331), (511), (440), and (622) were taken into account to draw W-H plots for all three compositions. **Fig. 4.5** shows W-H plots for **(a)** $\text{Ho}_2\text{Ti}_2\text{O}_7$, **(b)** $\text{Ho}_{1.9}\text{La}_{0.1}\text{Ti}_2\text{O}_7$, and **(c)** $\text{Ho}_{1.8}\text{La}_{0.2}\text{Ti}_2\text{O}_7$. Moreover, **Fig. 4.5 (d)** shows a variation in deduced crystallite size and microstrain which are calculated from the y-intercept and slope of linear W-H plot and are reported in **Table 4.1**.

Table 4.1 Parameters (structural) estimated from W-H plots and Rietveld analysis for $\text{Ho}_{2-x}\text{La}_x\text{Ti}_2\text{O}_7$.

$\text{Ho}_{2-x}\text{La}_x\text{Ti}_2\text{O}_7$	$x = 0.0$	$x = 0.1$	$x = 0.2$
Crystallite size (nm)	71(5)	87(6)	107(5)
Microstrain (%)	0.123(4)	0.122(2)	0.147(2)
48f (x, 0, 0)	0.3235(8)	0.3223(7)	0.3165(7)
Lattice constant (Å)	10.1135(1)	10.1223(3)	10.1397(4)
Ho/La–O_{48f} bond distance (Å)	2.5327(7)	2.5379(3)	2.5744(5)
Ho/La–O_{8b} bond distance (Å)	2.1875(3)	2.1922(2)	2.1951(1)
Ti–O_{48f} bond distance (Å)	1.9410(3)	1.9338(2)	1.908(2)
R_p, R_{wp}, R_{exp}, and χ^2	27.7, 24.1, 16.6, & 2.1	19.1, 19.4, 13.8, & 1.9	26.6, 24.5, 16.3, & 2.2

On increasing La content, the crystallite size is increased in a linear manner while microstrain remains almost constant for $x = 0.0$ and $x = 0.1$ concentrations. But micro-strain is drastically increased for the composition with the highest doping of La for $\text{Ho}_{1.8}\text{La}_{0.2}\text{Ti}_2\text{O}_7$. For $\text{Ho}_2\text{Ti}_2\text{O}_7$

composition, crystallite size was estimated to be $\sim 71 \pm 5$ nm which is increased by 22 % and 51 % on La doping in $\text{Ho}_{1.9}\text{La}_{0.1}\text{Ti}_2\text{O}_7$ and $\text{Ho}_{1.8}\text{La}_{0.2}\text{Ti}_2\text{O}_7$, respectively. These results are sufficient to conclude that the 10 % doping of La in $\text{Ho}_2\text{Ti}_2\text{O}_7$ drastically modify the structural properties of titanates as compared to 5 % doping.

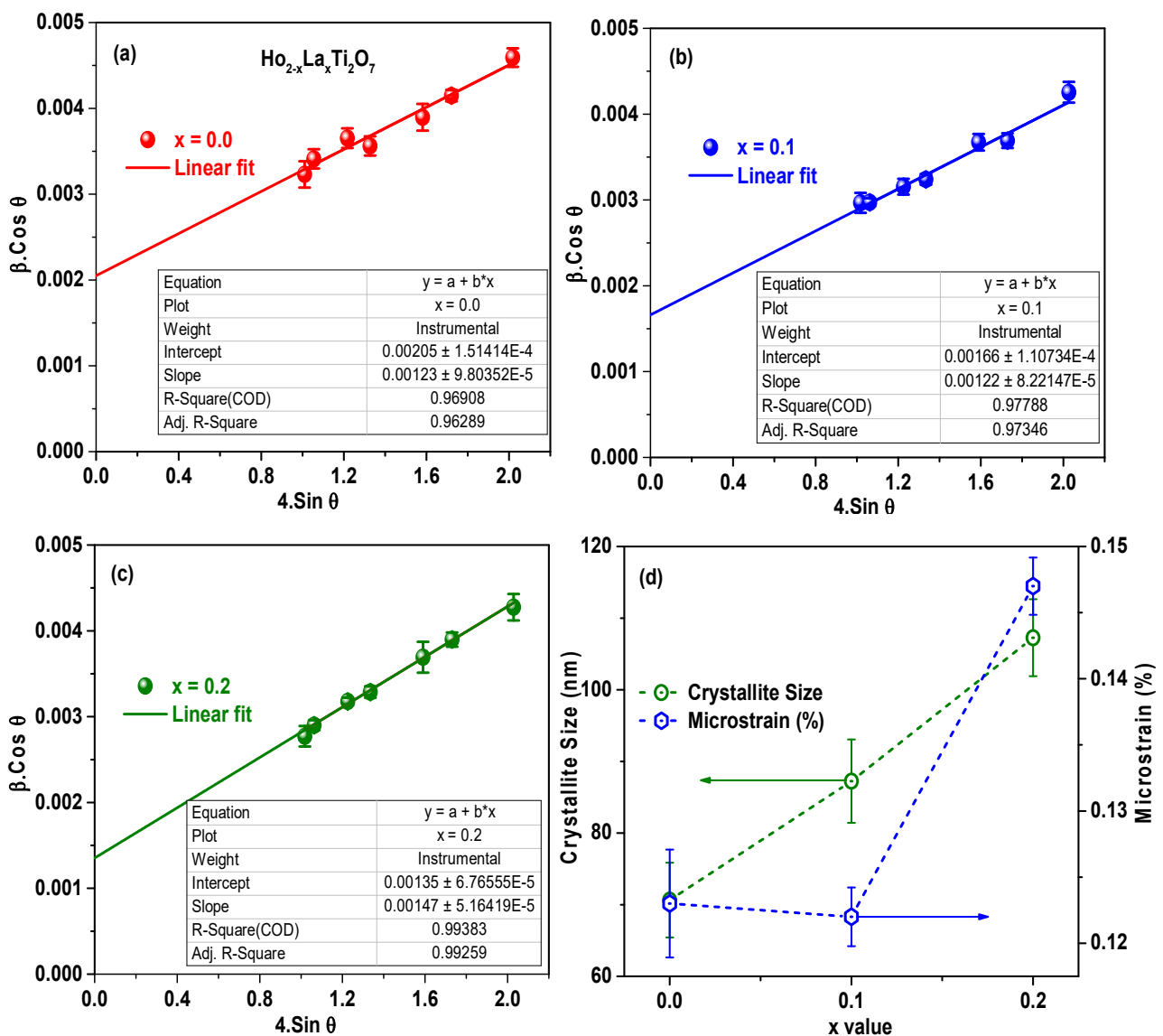


Fig. 4.5 W-H linear plots for (a) $x = 0.0$, (b) $x = 0.1$, and (c) $x = 0.2$. A representative for the variation in estimated (d) Crystallite size as well as microstrain.

4.3.2 Structural Investigation *via* Raman Spectroscopy

Raman spectroscopy plays a key role in the investigation of short-range structural behaviour like distortions, imperfection, ordering, electron-phonon and phonon-phonon interaction in all specimens.

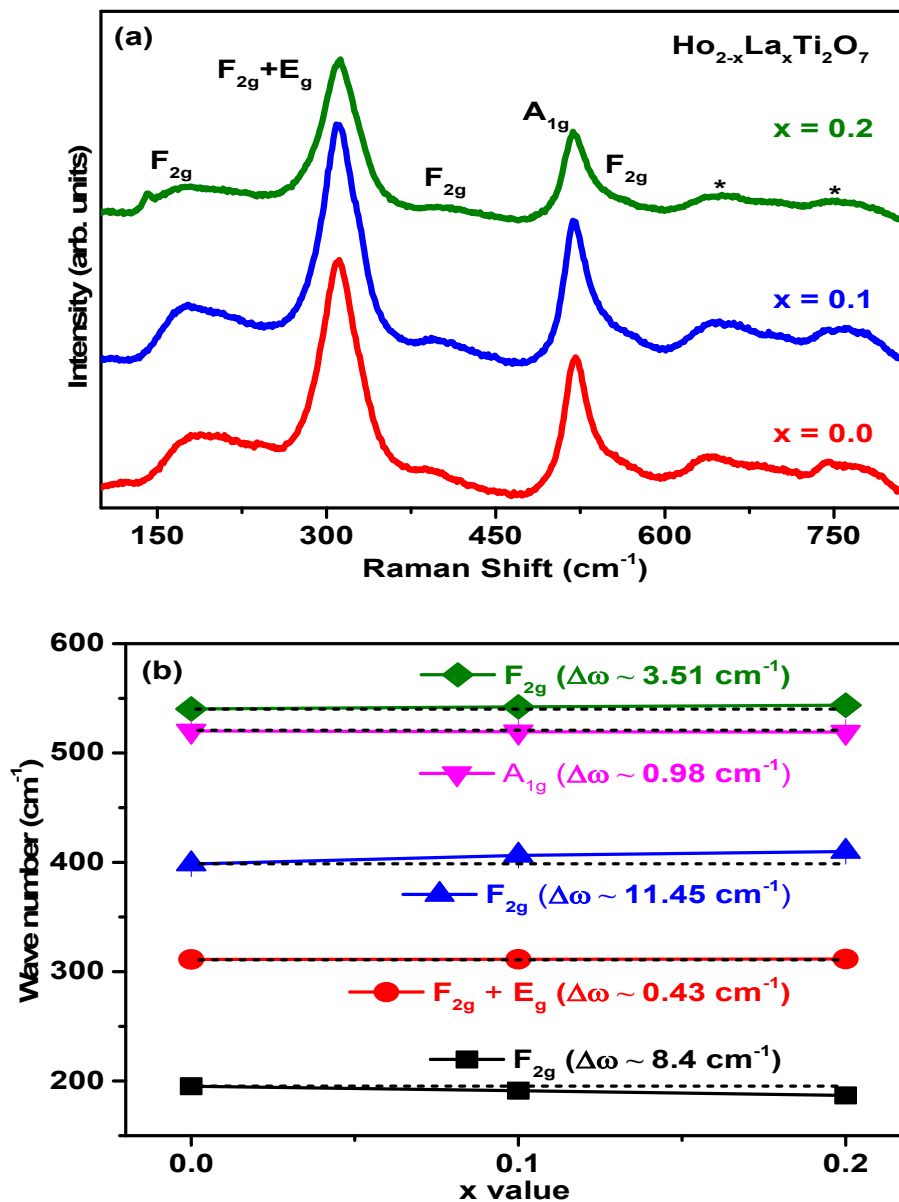


Fig. 4.6 (a) Raman spectra of $\text{Ho}_{2-x}\text{La}_x\text{Ti}_2\text{O}_7$ with $x = 0.0, 0.1,$ and 0.2 compositions, **(b)** variation in Raman active modes as a function of La-doping concentration.

Fig. 4.6 (a) shows the Raman spectra of $\text{Ho}_{2-x}\text{La}_x\text{Ti}_2\text{O}_7$ ($x = 0.0, 0.1,$ and 0.2) pyrochlore compositions. Based on the earlier reports, pyrochlore phonon modes based on factor group theory [32] are assigned as $[\text{E}_g+4\text{F}_{2g}+\text{A}_{1g}+7\text{F}_{1u}]$, where $\text{E}_g, 4\text{F}_{2g}$ and A_{1g} are six Raman modes (active) and 7F_{1u} mode is infrared active [33]. Raman spectrum was deconvoluted into seven Raman active bands for the compositions **(a)** $x = 0.0$, **(b)** $x = 0.1$, and **(c)** $x = 0.2$ depicted in **Fig. 4.7** and deduced position are also summarized in **Table 4.2**.

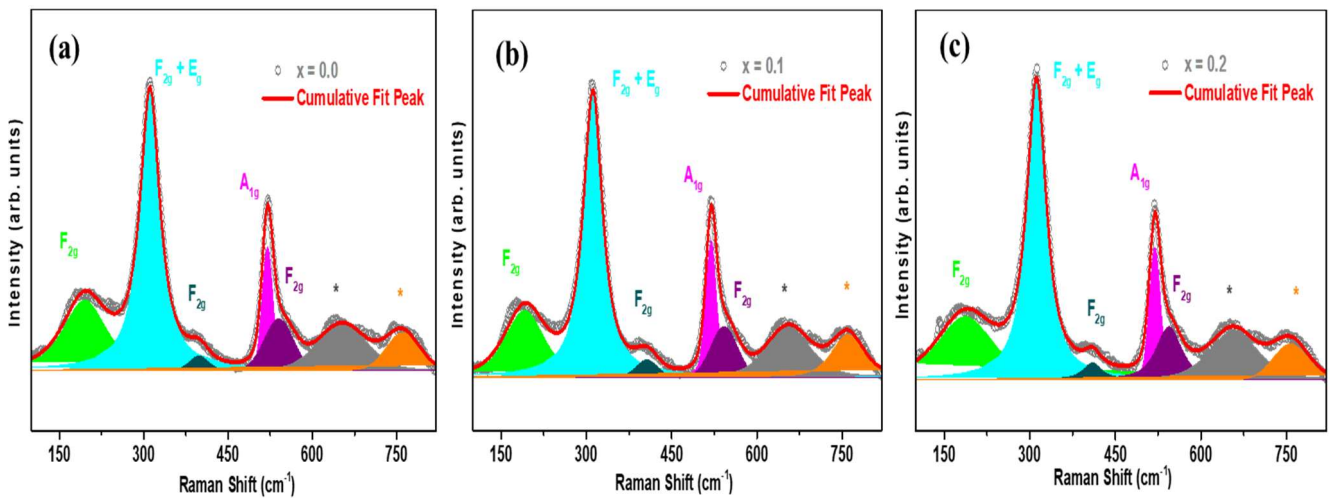


Fig. 4.7 (a-c) Deconvoluted Raman spectra for $x = 0.0, 0.1,$ and 0.2 .

Table 4.2 The position of deconvoluted Raman active modes for all three compositions.

$\text{Ho}_{2-x}\text{La}_x\text{Ti}_2\text{O}_7$	$\text{F}_{2g}(\text{cm}^{-1})$	$\text{F}_{2g} + \text{E}_g(\text{cm}^{-1})$	$\text{F}_{2g}(\text{cm}^{-1})$	$\text{A}_{1g}(\text{cm}^{-1})$	$\text{F}_{2g}(\text{cm}^{-1})$
x = 0.0	195.15 ± 0.41	311.18 ± 0.07	398.42 ± 0.86	520.17 ± 0.12	540.27 ± 0.86
x = 0.1	191.15 ± 0.46	311.36 ± 0.08	406.36 ± 0.71	519.43 ± 0.14	542.19 ± 0.78
x = 0.2	186.75 ± 0.52	311.61 ± 0.06	409.87 ± 0.89	519.19 ± 0.13	543.78 ± 0.83

It must be noted that two additional modes above 600 cm^{-1} are indicated by asterisk (653.4 cm^{-1} and 760.4 cm^{-1}) which can be attributed to 2nd order excitation or high-frequency IR active modes [34-35]. The peak at wavenumber $\sim 311.2\text{ cm}^{-1}$ can be assigned to F_{2g} and E_g modes in case of undoped $\text{Ho}_2\text{Ti}_2\text{O}_7$ composition in which F_{2g} links to bending modes ($\text{O}_{48f}\text{-Ho-O}_{48f}$) while E_g corresponds to sublattice (O_{48f}). The mode A_{1g} at wavenumber $\sim 520.2\text{ cm}^{-1}$ is allied with stretching bond (Ho-O_{48f}). Lowermost wavenumber peak at $\sim 195.2\text{ cm}^{-1}$ is associated with F_{2g} which is attributed to sublattice (O_{8b}). These both bands show a red shift as on increasing La-doping content. This shifting of phonon vibrations towards lower wavenumber side is associated with the increasing bond length or decreasing force constant on the replacement of a larger La^{3+} ion over Ho^{3+} . This redshift is also in accordance with the observed increment in bond lengths of Ho/La-O_{48f} and Ho/La-O_{8b} . This negligible change in the peak position of A_{1g} is linked with the movement of O_{8b} oxygen which can be correlated with a small variation in bond length of Ho/La-O_{8b} as measured from Rietveld refinement of XRD patterns. The rest of two Raman modes (F_{2g}) lie at $\sim 398.4\text{ cm}^{-1}$ and $\sim 540.3\text{ cm}^{-1}$ wavenumber in the present investigation. Moreover, shifting of phonons vibrations ($F_{2g} + E_g$ and $2 F_{2g}$) to higher wavenumber side with respect to La-content is related to the reducing bond length of Ti-O_{48f} as estimated from refinement. It is observed from the Raman analysis that Raman active mode associated with A cations shows red shift while the modes associated with B-cations exhibits blue shift. **Fig. 4.6 (b)** shows the Raman active modes as function of La^{3+} concentration in which the size of the symbol contains the error [36-37]. Remarkably, both Raman and XRD studies confirm a single-phase pyrochlore structure in all specimens with doping of La^{3+} ions on the A-site.

4.3.3 Composition and Microstructure Investigation

EDX measurement has been executed to check the concentrations of synthesized materials. It was observed that at the site (B^{4+}) ions are lesser than nominal concentrations when compared with A^{3+} site element in all specimens. This confirms the presence of extra A^{3+} ions on the B^{4+} site in HLTO compositions. This type of behaviour was also detected in other titanates such as $Yb_2Ti_2O_7$ which is known as stuffing [38]. Furthermore, EDX data verifies the substitution of La^{3+} in place of Ho^{3+} at A^{3+} site which is recorded in **Table 4.3**. Surface morphology investigation of as-prepared samples were performed by SEM. Recorded SEM images of $Ho_{2-x}La_xTi_2O_7$ specimens are shown in **Fig. 4.8**. These micrographs demonstrate surface morphology, grain size and porosity of HLTO pyrochlore. All specimens undergo high temperature sintering, which causes grain growth and the development of compact microstructure.

Table 4.3 Nominal and experimental mass (%) of $Ho_{2-x}La_xTi_2O_7$ ($x = 0.0, 0.1, \text{ and } 0.2$).

$Ho_{2-x}La_xTi_2O_7$	Nominal mass (%)				Experimental mass (%)		
	Ho	La	Ti	O	Ho	La	Ti
$x = 0.0$	61.35	0.00	17.81	20.84	61.43	0.00	17.82
$x = 0.1$	58.57	2.60	17.89	20.94	60.54	3.42	17.04
$x = 0.2$	55.76	5.22	17.98	21.04	57.21	5.32	17.27

Discrete grain boundaries are seemingly noticeable and simply distinct without any imperfections in all specimens. The grain size distribution in all three compositions were examined by measuring the size of around 100 grains in SEM micrographs through image J software. The grain size distribution histogram was plotted and fitted with Gaussian profile as depicted in **Fig. 4.8 (b, d, and f)**.

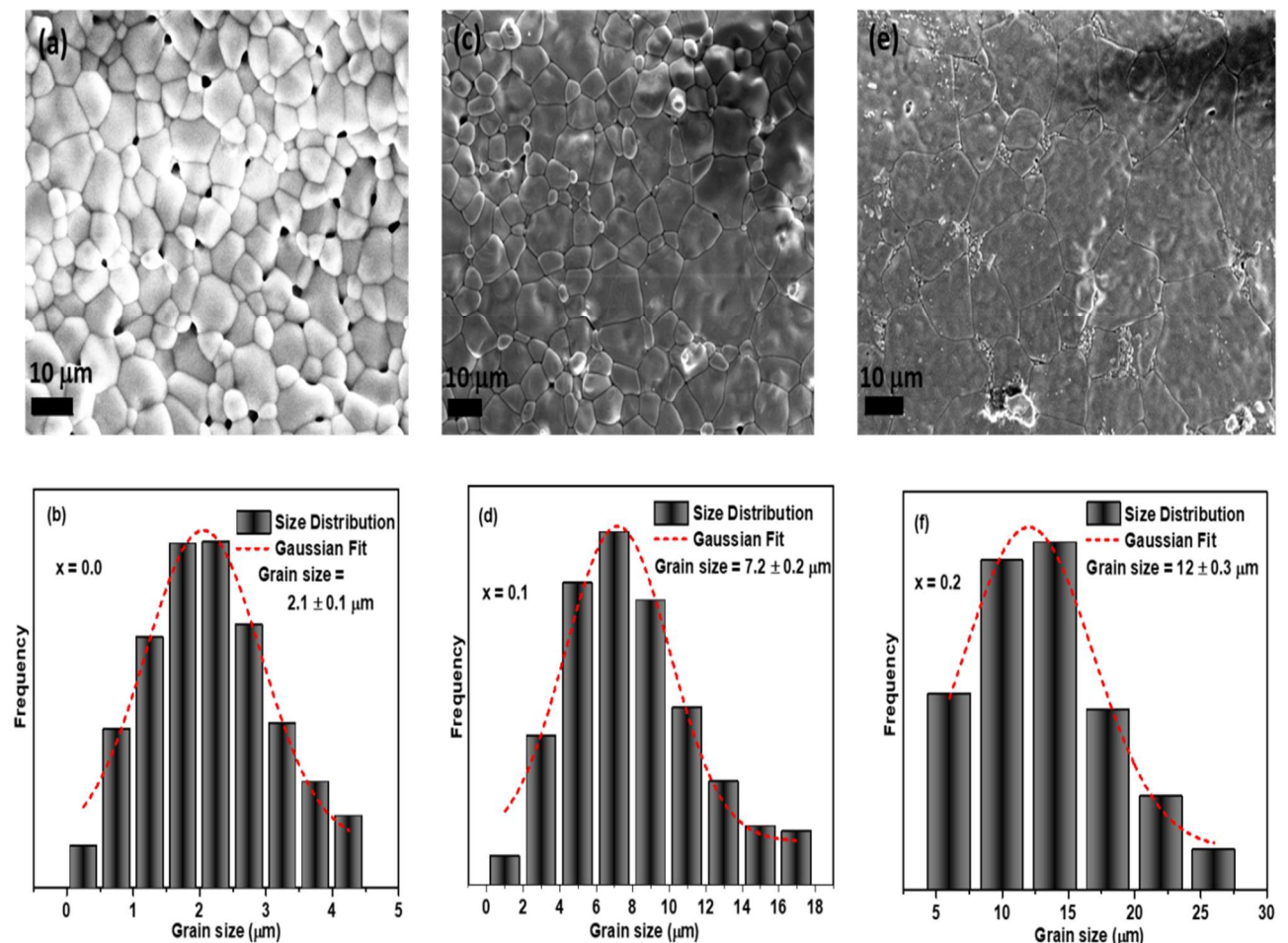


Fig. 4.8 (a, c, and e) SEM images and **(b, d, and f)** grain size distribution (a representation through histogram and size estimation through Gaussian fitting) of $\text{Ho}_{2-x}\text{La}_x\text{Ti}_2\text{O}_7$ ($x = 0.0, 0.1$ and 0.2) system.

The quantitative analysis of grain size using SEM micrographs provide an average value of grain size as $2.1 \pm 0.1 \mu\text{m}$, $7.2 \pm 0.2 \mu\text{m}$, and $12 \pm 0.3 \mu\text{m}$ for $x = 0.0$, $x = 0.1$, and $x = 0.2$, correspondingly. Since, XRD provides the most accurate information about the crystallite size in the range below 100 nm [7, 39] which can be calculated from Scherrer formula or W-H formulism take into account only coherently diffractive regions. On the contrary, SEM takes the micrographs of the diffused incoherently diffractive regions. Therefore, crystallite size and grain size calculated from XRD and SEM, respectively have different values. It can be seen that grain size increases with arise in the amount of La^{3+} at the A site. Grain growth is observed by ~ 3.4 and ~ 5.7 times at the doping concentration of $\text{Ho}_{0.9}\text{La}_{0.1}\text{Ti}_2\text{O}_7$ and $\text{Ho}_{0.8}\text{La}_{0.2}\text{Ti}_2\text{O}_7$, respectively. Observed trends from the SEM micrograph are in accordance with XRD results. Since, La doping leads to an increment in radius ratio (RR) from 1.68 to 1.70, this shows that composition with the highest RR for $x = 0.2$ can be easily stabilized with pyrochlore structure comparatively lower temperature in the $\text{Ho}_{2-x}\text{La}_x\text{Ti}_2\text{O}_7$ series. As all three compositions have experienced a same heating protocol, therefore the composition $x = 0.2$ have got comparatively more temperature and time for grain growth as compared to $x = 0$ and $x = 0.1$ compositions. Such type of grain size distribution was observed in $\text{Gd}_2\text{Ti}_{2-x}\text{Zr}_x\text{O}_7$ as on increasing doping of larger cation, Zr^{4+} at the place of Ti^{4+} . They found that the grain size decreases from $\sim 8 \mu\text{m}$ to $\sim 2 \mu\text{m}$ with increasing Zr^{4+} over Ti^{4+} in $\text{Gd}_2\text{Ti}_{2-x}\text{Zr}_x\text{O}_7$ for which RR varies from 1.74 ($\text{Gd}_2\text{Ti}_2\text{O}_7$) to 1.46 ($\text{Gd}_2\text{Zr}_2\text{O}_7$), respectively [8]. The grain size was estimated as $\sim 1.24 \pm 0.1 \mu\text{m}$ by Panghal *et al.*, for $\text{La}_2\text{Zr}_2\text{O}_7$ (RR = 1.61) sintered at 1500°C for 24 hrs [40]. Sharma *et al.*, were reported average grain size as for $\sim 1.0 \pm 0.02 \mu\text{m}$ for $\text{Nd}_2\text{Zr}_2\text{O}_7$ (RR = 1.54) sintered at 1350°C for 36 hrs [6]. Unlike these studies based on solid-state reaction methods, Kulriya *et al.*, also performed the grain growth studies on nanocrystalline $\text{Gd}_2\text{Ti}_2\text{O}_7$ synthesized through high energy ball milling followed by spark plasma sintering and estimated values were found

to be 6 μm to 10 μm as on sintering at 1300°C to 1500°C, respectively [41]. The observed grain size variation from 2 μm (Ho₂Ti₂O₇ with RR = 1.68) to 12 μm (Ho_{1.8}La_{0.2}Ti₂O₇ with RR = 1.70) affirmed that a relatively more ordered pyrochlore structure with larger RR value is experienced higher grain growth as they can be easily stabilized at lower heating temperature. To verify the grain growth with increasing La content, the density of the cylindrical pellets is measured experimentally and the obtained values are summarized in **Table 4.4**. The theoretical density of all three compositions were approximated with the help of atomic weight of all three ions namely; Ho (164.93032 gram/mole), La (138.905gram/mole), Ti (47.867 gram/mole), and O (15.9994 gram/mole) and the following relation (4.2) was employed.

$$\text{Theoretical density} = \frac{8 \times 10^{18} \times M}{6.02 \times 10^{23} \times a^3} \dots \dots \dots (4.2)$$

Where ‘a’ is the lattice constant in angstrom from **Table 4.1** and M is molecular weight.

Table 4.4 The theoretical density, experimental density and grain size estimated for specimens ($x = 0.0$, $x = 0.1$, and $x = 0.2$).

Ho_{2-x}La_xTi₂O₇	Theoretical density (g/cm³)	Experimental density (g/cm³)	Relative density	Grain size (μm)
x = 0.0	6.927	6.404	0.925	2.1(1)
x = 0.1	6.849	6.422	0.938	7.2(2)
x = 0.2	6.788	6.520	0.960	12.0(3)

The relative density was calculated as a ratio of observed experimental density to estimated theoretical density which is increased from 0.925 to 0.960 with x value. In other words, the porosity approximated as 7.5 %, 6.2 %, and 4.0 % for $x = 0.0$, $x = 0.1$, and $x = 0.2$, respectively. These variation in relative porosity revealed the reduction in free volume with increasing x value.

4.3.4 DC Magnetization Study

To study the magnetic behavior of HLTO specimens, magnetic measurements have been performed on all compositions using physical properties measurement system. The temperature-dependent magnetic susceptibility data of all specimens were recorded up to 2K with a functional field of 1000 Oe. **Fig. 4.9** shows variation in the magnetic susceptibility of HLTO compounds with temperature. All compositions follow the paramagnetic behaviour and exhibit overlapping in both field cooling (FC) and zero field cooling (ZFC) curves. This response specifies that neither spin glassy state nor ordering of spin occurs in all specimens even cooling the sample down to 2K.

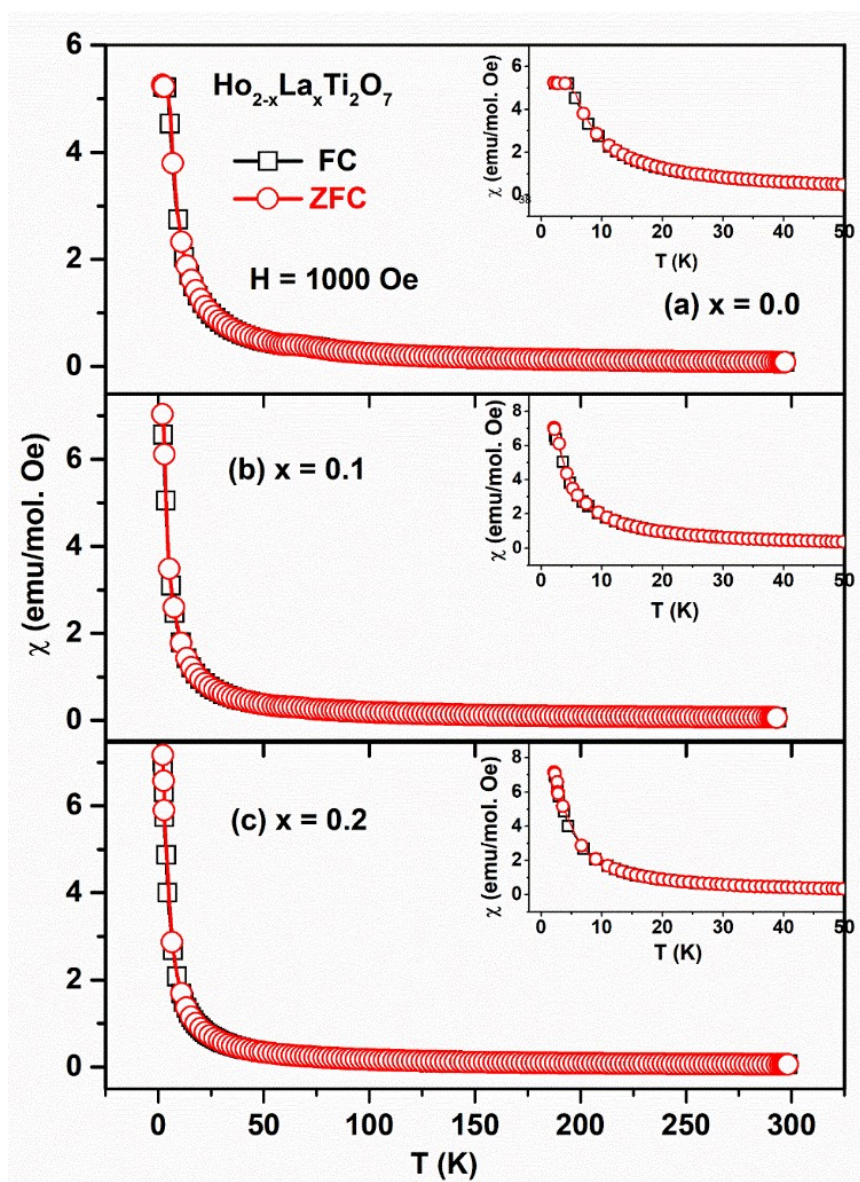


Fig. 4.9 Magnetic susceptibility vs temperature plots of $\text{Ho}_{2-x}\text{La}_x\text{Ti}_2\text{O}_7$ ($x = 0.0, 0.1$ and 0.2 figure **a**, **b** and **c**, respectively) compounds in the presence of 1000 Oe magnetic field (FC and ZFC). **Inset:** FC and ZFC curves recorded in the range of 2 – 50 K.

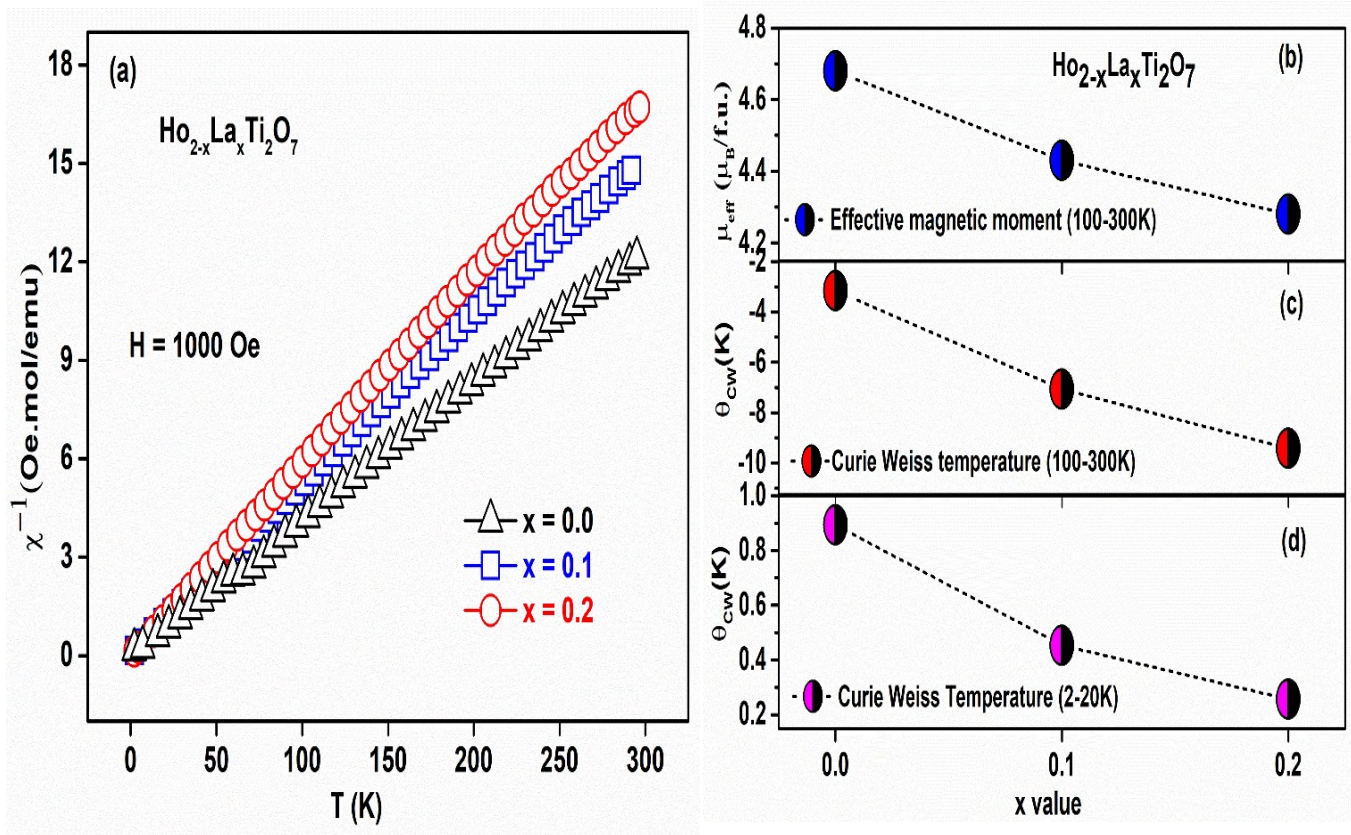


Fig. 4.10 (a) Display the inverse susceptibility (χ^{-1}) vs. temperature of the $\text{Ho}_{2-x}\text{La}_x\text{Ti}_2\text{O}_7$ ($x = 0.0, 0.1$ and 0.2) specimens with functional field of 1000 Oe. **(b)** Effective magnetic moments were estimated from Curie Weiss (CW) law at temperature (100 – 300 K). The Curie Weiss temperatures were calculated from fitting at temperature range of **(c)** 100 – 300 K, and **(d)** 2 – 20 K.

Fig. 4.10 (a) shows how the temperature (T) affects the inverse magnetic susceptibility (χ^{-1}) of HLTO compounds. Recorded graph displays linear behaviour for all compositions and complies with the Curie-Weiss law.

$$\chi = \frac{C}{T - \theta_{\text{CW}}} \dots \dots \dots (4.3)$$

Where C is Curie-constant and θ_{CW} is Curie-Weiss temperature. Effective magnetic moment (μ_{eff}) is calculated from experimental data using Curie constant [$C = \frac{N\mu_{eff}^2}{3K}$], K and N are the Boltzmann constant and Avogadro number, respectively [13].

$$\mu_{eff}^2 = y\mu_{Ho}^2 + x\mu_{La}^2 \dots \dots \dots (4.4)$$

Equation (4.4) can be employed to get theoretical effective magnetic moments. Where, y and x are number of Ho and La atoms/*f.u.*, respectively and μ_{Ho} and μ_{La} are magnetic moment of Ho^{3+} and La^{3+} atoms, respectively [42]. The calculated moment from electronic configuration ($4f^{10}$) of the free Ho^{3+} (5I_8) ions is $10.6\mu_B/Ho$. The temperature range used in the fitting process has a valuable impact on the recorded results. So, the data were fitted in the low-temperature (2 – 20 K) as well as a high-temperature (100 – 300 K) range. To avoid the effect of large crystal field splitting of the multiplets (Ho^{3+}), this fitting temperature range was selected which is appropriate for lower crystal field excitation. Identical fitting temperatures were also used in the earlier reported work [12, 16, 43]. The value of effective magnetic moment in both fittings are same and data obtained from the high-temperature fitting was plotted as shown in **Fig. 4.10 (b)**, which is consistent with previously reported results [12, 24]. Moreover, it may be noted that the experimental (estimated using Curie Weiss law) values of $\mu_{eff}/Ho(La)$ are smaller than theoretical data indicating occurrence of strong magnetic interaction between (Ho-Ho) spins. Frustration can be possible reason behind this as signified in the earlier reports [16, 30]. Observed positive values of θ_{CW} specify the ferromagnetic behavior of all synthesized compounds. Rise in chemical pressure results in lowering of θ_{CW} values (see fitted data 2-20K) which clearly shows the weakening of ferromagnetic character for all specimens. All obtained

parameters (CW temperatures θ_{CW}) are displayed in **Fig. 4.10 (c and d)**. This trend in the magnetic data is due to a change in dipolar and exchange interaction which results in the shifting of energy barrier in the doped compounds [43]. Experimentally observed magnetic parameters such as Weiss temperatures (θ_{CW}), magnetic moments (μ_{eff}) and saturation magnetization (M_{sat}) are recorded in **Table 4.5**. It is interesting to note that the Curie Weiss temperature changes dominantly with initial La^{3+} doping ($x = 0.1$), but evolves slowly with higher doping ($x = 0.2$), which is also consistent with the values of M_{sat} at 2 K.

Table 4.5 Experimentally observed magnetic parameters of the $Ho_{2-x}La_xTi_2O_7$ ($x = 0.0, 0.1, 0.2$) system.

$Ho_{2-x}La_xTi_2O_7$	θ_{CW} (K) (2-20K)	θ_{CW} (K) (100 – 300K)	$\mu_{eff}/f.u.$ (μ_B)	$M_{sat}/f.u.$ (μ_B)
x = 0.0	0.893	-3.156	4.68	7.89
x = 0.1	0.454	-7.064	4.43	6.93
x = 0.2	0.257	-9.423	4.28	6.53

M-H diagrams of $Ho_{2-x}La_xTi_2O_7$ compositions at 2 K are displayed in **Fig. 4.11**. It shows a decrease in the experimentally estimated saturation magnetization (M_{sat}) with lowering the concentration of magnetic Ho ions (increasing La content). The calculated values of magnetization are 7.89, 6.93 and 6.53 $\mu_{B/Ho}$ for $x = 0.0, 0.1$ and 0.2 respectively, which is lower than theoretical estimated values. The observation of lesser magnetization can be explained on

the basis of the powder angular averaging effect and single-ion anisotropy [28]. In magnetic pyrochlore oxide, the magnetic site (16d) is mostly accountable for magnetization, however nonmagnetic site (16c) is too contributory to magnetization. But the atoms are fixed at the magnetic Wyckoff position for all specimens, it implies that the 16c site is also responsible for a reduction in saturation magnetization [44].

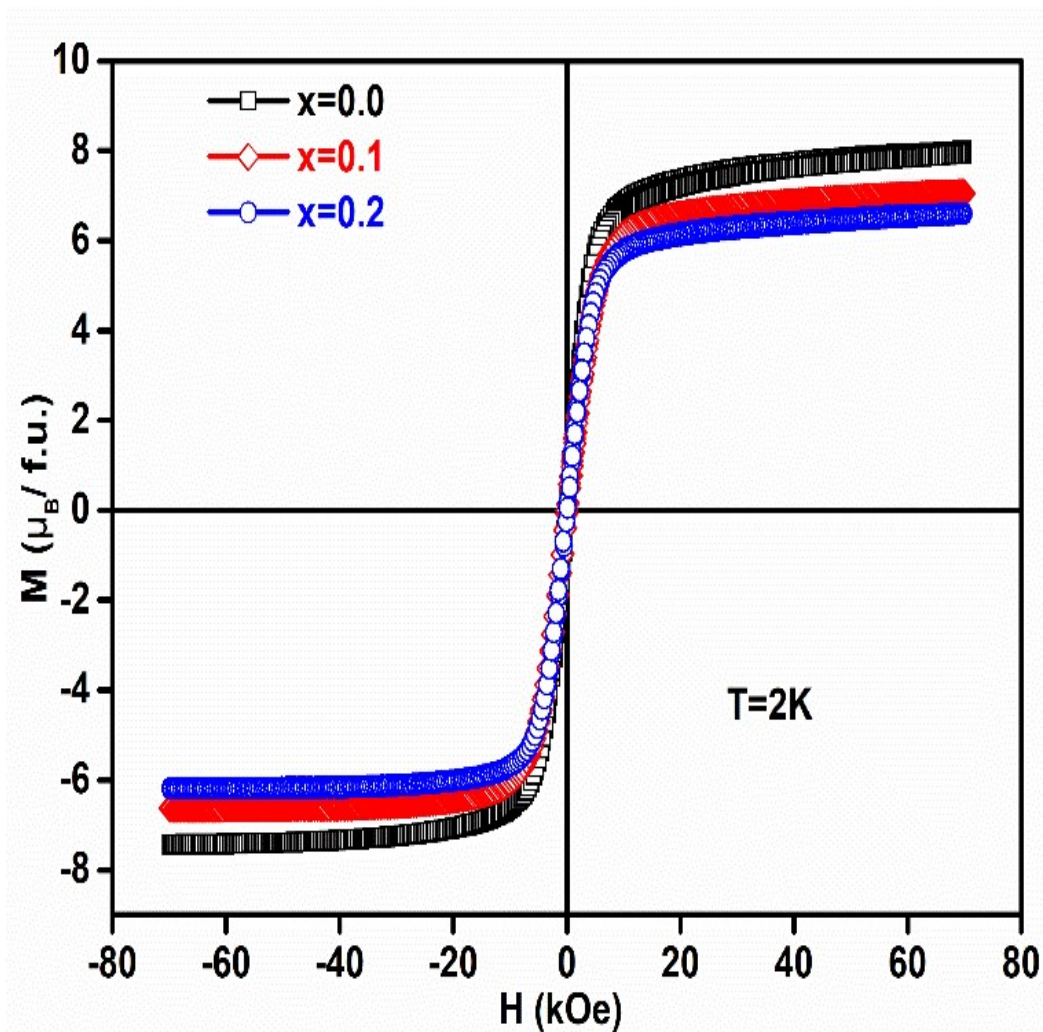


Fig. 4.11 M-H diagrams of $\text{Ho}_{2-x}\text{La}_x\text{Ti}_2\text{O}_7$ specimens recorded at 2 K.

It can be concluded that chemical pressure effect weakens ferromagnetic character, which is accordant to the results of inverse susceptibility (χ^{-1}) against temperature curve. Similar type of magnetization behaviour was also noticed in $\text{Ho}_2(\text{Ti}_{1-x}\text{Ge}_x)_2\text{O}_7$, where magnetization is decreased by the doping of the smaller cation Ge^{4+} in place of Ti^{4+} (B site) [19]. The comparison of doping at the A and B sites in the $\text{Ho}_2\text{Ti}_2\text{O}_7$ shows that θ_{CW} decreased by 71% and 33 % due to 10 % doping of larger cation (La^{3+}) at A site and smaller cation (Ge^{4+}) at B site, respectively. Thus, these results are plausible to conclude that B site doping is more sensitive than A site doping in terms of controlling magnetic properties. Moreover, Liu *et al.* reported that the θ_{CW} was reduced to 45% when the nonmagnetic La^{3+} was substituted (10%) at the A site of $\text{Dy}_2\text{Ti}_2\text{O}_7$ compound [43]. Therefore, on comparing with the prior studies, larger decrement in θ_{CW} with similar doping amount was observed in the present work. This could be due to the large crystal field splitting of Ho^{3+} (multiplets) cations.

4.4 Conclusion

A prominent ceramic holmium titanate ($\text{Ho}_2\text{Ti}_2\text{O}_7$) in which magnetic and structural features are coupled, is recognized by its unfamiliar spin freeze state. In the present chapter, magnetic and structural behaviour of $\text{Ho}_{2-x}\text{La}_x\text{Ti}_2\text{O}_7$ pyrochlore prepared through solid state method, were explored by partial replacement of Ho^{3+} with nonmagnetic La^{3+} . The formation of a single-phasic, contamination-free pyrochlore crystal structure with linearly increasing cell parameters that adhere to Vegard's law was proven by structural analysis. The crystalline size (71 ± 5 nm, 87 ± 6 nm and 107 ± 5 nm for $x = 0.0, 0.1$ and 0.2 , respectively) calculated from W-H plot is increased with nonmagnetic La doping which is consistent with electron microscopy studies. Further, Raman spectra reveals that La^{3+} was entirely dissolved in the $\text{Ho}_2\text{Ti}_2\text{O}_7$ host material without significantly altering its structural integrity, which is in good

accord with the XRD results. Raman studies shown the red and blue shift of the phonon mode and increase in the structural ordering due to increase in the ionic radii ratio by incorporation of La in $\text{Ho}_{2-x}\text{La}_x\text{Ti}_2\text{O}_7$. All samples of SEM micrographs are made up of agglomerative, micron-sized spherical particles. Structural ordering of the pyrochlore oxides was found to increase with La doping in the $\text{Ho}_{2-x}\text{La}_x\text{Ti}_2\text{O}_7$ system. Even after lowering the temperature by up to 2 K, no spin glassy pattern could be found. It was observed that the ferromagnetic feature is continuously diminishing with chemical pressure in all specimens. Variation in the dipolar and exchange interaction is the cause of this behavior in the magnetic data. A large reduction the Curie Weiss temperature in the case of $\text{Ho}_2\text{Ti}_2\text{O}_7$ doped with La^{3+} suggested that A site doping is less sensitive than B site doping for controlling magnetic properties. Furthermore, reduction in the value of θ_{CW} also depends upon the nature and location of the dopant. Large reduction in the θ_{CW} for $\text{Ho}_2\text{Ti}_2\text{O}_7$ doped with La^{3+} suggested that doping at the A site can be used for the tuning the θ_{CW} . Future research into these system by crystallographic alterations at temperatures where spin ices are known to freeze and lose their equilibrium, would be fascinating.

References

1. Gardner, Jason S., Michel JP Gingras, and John E. Greedan. "Magnetic pyrochlore oxides." *Reviews of Modern Physics* 82, no. 1 (2010): 53.
2. Harris, Mark J., S. T. Bramwell, D. F. McMorrow, T. H. Zeiske, and K. W. Godfrey. "Geometrical frustration in the ferromagnetic pyrochlore $\text{Ho}_2\text{Ti}_2\text{O}_7$." *Physical Review Letters* 79, no. 13 (1997): 2554.
3. Morris, David Jonathan Pryce, D. A. Tennant, S. A. Grigera, B. Klemke, C. Castelnovo, R. Moessner, C. Czternasty et al. "Dirac strings and magnetic monopoles in the spin ice $\text{Dy}_2\text{Ti}_2\text{O}_7$." *Science* 326, no. 5951 (2009): 411-414.
4. Oh, Si Hyoun, Robert Black, Ekaterina Pomerantseva, Jin-Hyon Lee, and Linda F. Nazar. "Synthesis of a metallic mesoporous pyrochlore as a catalyst for lithium– O_2 batteries." *Nature chemistry* 4, no. 12 (2012): 1004-1010.
5. Shlyakhtina, A. V., and L. G. Shcherbakova. "New solid electrolytes of the pyrochlore family." *Russian Journal of Electrochemistry* 48, no. 1 (2012): 1-25.
6. Sharma, Saurabh Kumar, V. Grover, A. K. Tyagi, D. K. Avasthi, U. B. Singh, and P. K. Kulriya. "Probing the temperature effects in the radiation stability of $\text{Nd}_2\text{Zr}_2\text{O}_7$ pyrochlore under swift ion irradiation." *Materialia* 6 (2019): 100317.
7. Sharma, S. K., V. Grover, R. Shukla, A. Hussain, A. Mishra, R. C. Meena, and P. K. Kulriya. "Evidence of improved tolerance to electronic excitation in nanostructured $\text{Nd}_2\text{Zr}_2\text{O}_7$." *Journal of Applied Physics* 129, no. 11 (2021): 115902.
8. Kumar, A., P. K. Kulriya, S. K. Sharma, V. Grover, A. K. Tyagi, and V. K. Shukla. "Structural and compositional effects on the electronic excitation induced phase transformations in $\text{Gd}_2\text{Ti}_{2-y}\text{Zr}_y\text{O}_7$ pyrochlore." *Journal of Nuclear Materials* 539 (2020): 152278.

9. Bramwell, Steven T., and Michel JP Gingras. "Spin ice state in frustrated magnetic pyrochlore materials." *Science* 294, no. 5546 (2001): 1495-1501.
10. Balents, Leon. "Spin liquids in frustrated magnets." *Nature* 464, no. 7286 (2010): 199-208.
11. Binder, Kurt, and A. Peter Young. "Spin glasses: Experimental facts, theoretical concepts, and open questions." *Reviews of Modern physics* 58, no. 4 (1986): 801.
12. Liu, Hui, Youming Zou, Lei Zhang, Langsheng Ling, Hongyan Yu, Lei He, Changjin Zhang, and Yuheng Zhang. "Magnetic order and dynamical properties of the spin-frustrated magnet $Dy_{2-x}Yb_xTi_2O_7$." *Journal of magnetism and magnetic materials* 349 (2014): 173-179.
13. Clancy, J. P., J. P. C. Ruff, S. R. Dunsiger, Y. Zhao, H. A. Dabkowska, J. S. Gardner, Y. Qiu, J. R. D. Copley, T. Jenkins, and B. D. Gaulin. "Revisiting static and dynamic spin-ice correlations in $Ho_2Ti_2O_7$ with neutron scattering." *Physical Review B* 79, no. 1 (2009): 014408.
14. Cornelius, A. L., and J. S. Gardner. "Short-range magnetic interactions in the spin-ice compound $Ho_2Ti_2O_7$." *Physical Review B* 64, no. 6 (2001): 060406.
15. Marques, M. D. R., F. S. Portela, A. A. M. Oliveira, PetrucioBarrozo, N. O. Moreno, P. C. A. Brito, and J. Albino Aguiar. "Structural and magnetic properties of pyrochlores $Gd_{2-x}M_xRu_2O_7$ (M= Ho, Y)." *Physica B: Condensed Matter* 407, no. 16 (2012): 3106-3108.
16. Liu, Hui, Youming Zou, Langsheng Ling, Lei Zhang, Changjin Zhang, and Yuheng Zhang. "Enhanced ferromagnetism and emergence of spin-glass-like transition in pyrochlore compound $Dy_2Ti_{2-x}V_xO_7$." *Journal of Magnetism and Magnetic Materials* 388 (2015): 135-142.

17. Pal, Arkadeb, Abhishek Singh, A. K. Ghosh, and Sandip Chatterjee. "High-temperature spin-freezing transition in pyrochlore $\text{Eu}_2\text{Ti}_2\text{O}_7$: A new observation from ac-susceptibility." *Journal of Magnetism and Magnetic Materials* 462 (2018): 1-7.
18. Nemytova, O. V., I. V. Piir, M. S. Koroleva, D. V. Perov, and A. B. Rinkevich. "Magnetic properties of nanocomposite and bulk rare earth titanates $\text{Ho}_2\text{Ti}_2\text{O}_7$ and $\text{Yb}_2\text{Ti}_2\text{O}_7$." *Journal of Magnetism and Magnetic Materials* 494 (2020): 165800.
19. Chandra, Kailash, Vinod Singh, Saurabh K. Sharma, and Pawan K. Kulriya. "Structural magnetic properties correlation in Ge doped frustrated $\text{Ho}_2\text{Ti}_2\text{O}_7$ pyrochlore." *Journal of Magnetism and Magnetic Materials* (2022): 169694.
20. Xing, Hui, Hanjie Guo, Chunmu Feng, Zhu-An Xu, and Hao Zeng. "On the origin of the two thermally driven relaxations in diluted spin ice $\text{Dy}_{1.6}\text{Y}_{0.4}\text{Ti}_2\text{O}_7$." *Journal of Physics: Condensed Matter* 25, no. 4 (2012): 046005.
21. Snyder, J., B. G. Ueland, Ari Mizel, J. S. Slusky, H. Karunadasa, R. J. Cava, and P. Schiffer. "Quantum and thermal spin relaxation in the diluted spin ice $\text{Dy}_{2-x}\text{M}_x\text{Ti}_2\text{O}_7$ (M= Lu, Y)." *Physical Review B* 70, no. 18 (2004): 184431.
22. Kajňaková, M., M. Orendáč, A. Orendáčová, A. Vlček, T. Fennell, and S. T. Bramwell. "Thermodynamic properties of magnetically diluted dipolar spin ice." *Journal of Magnetism and Magnetic Materials* 272 (2004): E989-E991.
23. Ehlers, Georg, E. Mamontov, M. Zamponi, A. Faraone, Y. Qiu, A. L. Cornelius, C. H. Booth et al. "Frustrated spin correlations in diluted spin ice $\text{Ho}_{2-x}\text{La}_x\text{Ti}_2\text{O}_7$." *Journal of Physics: Condensed Matter* 20, no. 23 (2008): 235206.
24. Shukla, Manjari, Soma Banik, Rajan K. Pandey, and Chandan Upadhyay. "Role of chemical pressure on optical and electronic structure of $\text{Ho}_2\text{Ge}_x\text{Ti}_{2-x}\text{O}_7$." *Journal of Physics: Condensed Matter* 32, no. 11 (2019): 115501.

25. Berwal, Umang, Vinod Singh, and Rinku Sharma. " Key role of Tb³⁺ doping on structural and photoluminescence properties of Gd₂Ti₂O₇ pyrochlore oxide." *Ceramics International* (2022).
26. Kulriya, P. K., F. Singh, A. Tripathi, R. Ahuja, A. Kothari, R. N. Dutt, Y. K. Mishra, Amit Kumar, and D. K. Avasthi. "Setup for in situ X-ray diffraction study of swift heavy ion irradiated materials." *Review of Scientific Instruments* 78, no. 11 (2007): 113901
27. Rodríguez-Carvajal, Juan. "Recent advances in magnetic structure determination by neutron powder diffraction." *Physica B: Condensed Matter* 192, no. 1-2 (1993): 55-69.
28. Singh, Prajyoti, Arkadeb Pal, Vinod K. Gangwar, Prince K. Gupta, MohdAlam, Surajit Ghosh, R. K. Singh, A. K. Ghosh, and Sandip Chatterjee. "Wasp–Waisted loop and spin frustration in Dy_{2-x}Eu_xTi₂O₇ pyrochlore." *J. of Magnetism and Magnetic Materials* 518 (2021): 167364.
29. Kumari, Renu, P. K. Kulriya, V. Grover, R. Shukla, K. Saravanan, S. Mohapatra, A. K. Tyagi, and D. K. Avasthi. "Radiation stability of Gd₂Zr₂O₇: effect of stoichiometry and structure." *Ceramics International* 42, no. 1 (2016): 103-109.
30. Chang, L. J., W. Schweika, Y-J. Kao, Y. Z. Chou, J. Perbon, Th Brückel, Hong-Chang Yang, Y. Y. Chen, and J. S. Gardner. "Magnetic correlations in Ho_xTb_{2-x}Ti₂O₇." *Physical Review B* 83, no. 14 (2011): 144413.
31. L. Vegard: *Z. Phys.* 5 (1921) 17.
32. Saha, Surajit, Surjeet Singh, BrahimDkhil, S. Dhar, R. Suryanarayanan, G. Dhahenne, A. Revcolevschi, and A. K. Sood. "Temperature-dependent Raman and -ray studies of the spin-ice pyrochlore Dy₂Ti₂O₇ and nonmagnetic pyrochlore Lu₂Ti₂O₇." *Physical Review B* 78, no. 21 (2008): 214102.

33. Glerup, Marianne, Ole Faurskov Nielsen, and Finn Willy Poulsen. "The structural transformation from the pyrochlore structure, $A_2B_2O_7$, to the fluorite structure, AO_2 , studied by Raman spectroscopy and defect chemistry modeling." *Journal of Solid-State Chemistry* 160, no. 1 (2001): 25-32.
34. Maćzka, M., M. L. Sanjuán, A. F. Fuentes, L. Macalik, J. Hanuza, K. Matsuhira, and Z. Hiroi. "Temperature-dependent studies of the geometrically frustrated pyrochlores $Ho_2Ti_2O_7$ and $Dy_2Ti_2O_7$." *Physical Review B* 79, no. 21 (2009): 214437.
35. Kumar, Ajay, Saurabh Kumar Sharma, V. Grover, Yogendar Singh, Vivek Kumar, Vivek Kumar Shukla, and P. K. Kulriya. "Probing the Short-Range Ordering of Ion Irradiated $Gd_2Ti_2-yZryO_7$ ($0.0 \leq y \leq 2.0$) Pyrochlore under Electronic Stopping Regime." *Journal of Nuclear Materials* 564 (2022): 153682.
36. Singh, Prajyoti, Arkadeb Pal, Vinod K. Gangwar, Surajit Ghosh, Ranjan K. Singh, A. K. Ghosh, and Sandip Chatterjee. "Spin freezing and field induced transition in $(Tb_{1-x}Eu_x)_2Ti_2O_7$: A magnetic property study." *Journal of Magnetism and Magnetic Materials* 490 (2019): 165512.
37. Subramanian, M. A., G. Aravamudan, and GV Subba Rao. "Oxide pyrochlores—a review." *Progress in Solid State Chemistry* 15, no. 2 (1983): 55-143.
38. Ross, K. A., Th Proffen, H. A. Dabkowska, J. A. Quilliam, L. R. Yaraskavitch, J. B. Kycia, and B. D. Gaulin. "Lightly stuffed pyrochlore structure of single-crystalline $Yb_2Ti_2O_7$ grown by the optical floating zone technique." *Physical Review B* 86, no. 17 (2012): 174424.
39. Kaliyaperumal, Amirthapandian Sankarakumar, and Thangadurai Paramasivam. "Grain size engineering in nanocrystalline $Y_2Zr_2O_7$: A detailed study on the grain size

- correlated electrical properties." *Journal of Alloys and Compounds* 831 (2020): 154782.
40. Panghal, Asha, Pawan K. Kulriya, Yogendra Kumar, Fouran Singh, and N. L. Singh. "Investigations of atomic disorder and grain growth kinetics in polycrystalline $\text{La}_2\text{Zr}_2\text{O}_7$." *Applied Physics A* 125, no. 6 (2019): 1-11.
41. Kulriya, P. K., Tiankai Yao, Spencer Michael Scott, Sonal Nanda, and Jie Lian. "Influence of grain growth on the structural properties of the nanocrystalline $\text{Gd}_2\text{Ti}_2\text{O}_7$." *Journal of Nuclear Materials* 487 (2017): 373-379.
42. Orendáč, M., P. Vrábel, A. Orendáčová, J. Prokleška, V. Sechovský, S. Singh, R. Suryanarayanan, and A. Revcolevschi. "Magnetic order in hybrid frustrated magnets $\text{Gd}_{2-x}\text{Tb}_x\text{Ti}_2\text{O}_7$ ($x = 0.2$ and 0.5)." *Journal of Physics: Condensed Matter* 24, no. 18 (2012): 186003.
43. Liu, Hui, Jian Bian, Shiyun Chen, Yuan Feng, Yu Xie, and Baolong Fang. "Magnetic and dynamical properties in the diluted spin ice $\text{Dy}_{2-x}\text{La}_x\text{Ti}_2\text{O}_7$." *Journal of Magnetism and Magnetic Materials* 465 (2018): 316-322.
44. Yadav, Pramod K., Pinki Singh, Manjari Shukla, Soma Banik, and Chandan Upadhyay. "Effect of B-site substitution on structural, magnetic and optical properties of $\text{Ho}_2\text{Ti}_2\text{O}_7$ pyrochlore oxide." *Journal of Physics and Chemistry of Solids* 138 (2020): 109267.

Chapter 5

Probing the Influence of Ho^{3+} Substitution at A-site on Structural and Magnetic Studies of $(\text{Gd}_{1-y}\text{Ho}_y)_2\text{Ti}_2\text{O}_7$ ($y = 0.0, 0.2, 0.4, \text{ and } 0.6$) Pyrochlore

This chapter analyses the probing the influence of Ho^{3+} substitution at A-site on structural and magnetic properties of $(\text{Gd}_{1-y}\text{Ho}_y)_2\text{Ti}_2\text{O}_7$ ($y = 0.0, 0.2, 0.4, \text{ and } 0.6$) ceramics. Antiferromagnetically (AFM) linked Heisenberg spins are predicted to be extremely frustrating in the $\text{Gd}_2\text{Ti}_2\text{O}_7$ pyrochlore lattice because there are numerous ways to minimize the exchange energy. Magnetic studies have demonstrated the system becomes less antiferromagnetic (AFM) character as a result of the increased chemical pressure in $\text{Gd}_2\text{Ti}_2\text{O}_7$. The glassy pattern could not be found even when the temperature was lowered by up to 2 K. Moreover, a larger increment in θ_{CW} was observed with a similar amount of doping linked to the earlier studies. This might be brought on by the Gd-Ho cation's strong crystal field splitting. In comparison of A and B site substitution, it can be said that doping at the B site is more effective at regulating magnetic features than doping at the A site.

5.1 Introduction

The pyrochlore structured ceramic $A_2B_2O_7$ (A and B stand for rare earth elements and transition metal respectively) have fascinated an excessive deal of research interest over the last two decades [1-5]. Geometrical frustration in pyrochlore oxides is an important phenomenon of devotion for theorists and experimentalists. [6-14]. We studied the smaller cation germanium doping at the B site of $Ho_2Ti_2O_7$ pyrochlore in Chapter 3rd, and it was discovered that an increase in the amount of Ge (B site) results in a decrease in the ferromagnetic nature of the doped compounds. On the other hand, chapter 4th summarised that nonmagnetic (La^{3+}) dilution at the A site of $Ho_2Ti_2O_7$ diminishes the ferromagnetic feature of the compounds with a rise in chemical pressure. $Ho_2Ti_2O_7$ doped with La^{3+} showed a significant decrease in the Curie Weiss temperature which indicates, when it comes to regulating magnetic characteristics, A site doping is less sensitive than B site doping. The current chapter revealed the effect of magnetic element (Ho) doping at A site of $Gd_2Ti_2O_7$ material on structural and magnetic properties. And also compared the result of magnetic and nonmagnetic substitution at the A site of titanates.

The pyrochlore $Ho_2Ti_2O_7$ is referred to as spin ice material and behaves similarly to water ice by following the spin ice rule whereas $Gd_2Ti_2O_7$ exhibits long range ordered phase [15]. Single ion anisotropy, dipole exchange interactions, crystal field effects and ferromagnetic interactions cause the spins of rare earth ions in spin ice materials to align two spins directly toward and two spins directly away from the tetrahedron's centre. $Tb_2Ti_2O_7$ has a changing spin liquid nature down to the lowest possible temperature [16]. The effective moment for $Gd_2Ti_2O_7$ pyrochlore was reported by Raju *et al.* to be close to theoretical limit of $7.94 \mu_B$ and to have a Curie temperature of $\theta_{CW} \sim -10$ K [17]. $Ho_2Ti_2O_7$ has Curie temperature of $\theta_{CW} \sim 1.0$ K, which supports its significant spin ice feature [18]. As reported by Kailash *et al.* by increasing the

doping of the smaller cation Ge^{4+} in place of Ti^{4+} (B-site), the Curie Weiss temperature of the $\text{Ho}_2(\text{Ti}_{1-x}\text{Ge}_x)_2\text{O}_7$ (with $x = 0.0, 0.2,$ and 0.4) system is lowered from 0.86 K to 0.57 K due to decrement in ferromagnetic nature of the compounds [19]. Different Curie temperatures for several other pyrochlores were also noted in the earlier studies. Curie temperature for $\text{Dy}_2\text{Ti}_2\text{O}_7$ was found to be $\theta_{\text{CW}} \sim 1.0$ K [20] while $\text{Gd}_2\text{Ru}_2\text{O}_7$ and $\text{Ho}_2\text{Ru}_2\text{O}_7$ have Curie temperatures of -11.77 K and $+1.12$ K correspondingly, as conveyed by Marques *et al.* [21].

Although in earlier studies, specific investigations into the structure and magnetic behavior of $\text{Gd}_2\text{Ti}_2\text{O}_7$ and $\text{Ho}_2\text{Ti}_2\text{O}_7$ were made [15, 22]. Learning how chemical pressure affects the magnetic properties of $(\text{Gd}_{1-y}\text{Ho}_y)_2\text{Ti}_2\text{O}_7$ polycrystalline pyrochlore, is exceedingly difficult. It is really motivating to study how Ho^{3+} substitution at A site of $\text{Gd}_2\text{Ti}_2\text{O}_7$ affects the material's structural and magnetic characteristics. As per literary analysis, the stability of pyrochlore ($\text{A}_2\text{B}_2\text{O}_7$) is controlled by ion radius ratio of A^{3+} and B^{4+} cations. The value of $R_{\text{A}}/R_{\text{B}}$ (RR) for the stable pyrochlore structure ranges from 1.46 to 1.78 . The structure changes to defect fluorite for $\text{RR} < 1.46$ and produces a perovskite layered structure for $\text{RR} > 1.78$ [23-24]. Gd^{3+} and Ho^{3+} have cationic radii of 1.053 and 1.015 , respectively. Due to this, $R_{\text{Gd}}/R_{\text{Ti}}$ and $R_{\text{Ho}}/R_{\text{Ti}}$ have respective ratios of 1.74 and 1.68 , signifying that the core pyrochlore structure is unaffected by the substitution of Ho^{3+} ions in $\text{Gd}_2\text{Ti}_2\text{O}_7$ host matrix. Hence, we have examined the relationship between the magnetic and structural characteristics of $(\text{Gd}_{1-y}\text{Ho}_y)_2\text{Ti}_2\text{O}_7$ ($y = 0.0, 0.2, 0.4$ and 0.6) pyrochlore in the present chapter.

The synthesis of GHTO pyrochlore was accomplished by a solid-state process. X-ray Diffraction, Raman Spectroscopy, and physical properties measurement system were used to characterize all compositions of produced compounds. Structural and magnetic analysis reveals that the increase in magnetization is caused by weakening of the antiferromagnetic (AFM) character and contribution of the 16d magnetic site, as well as a decrease in the ratio of ionic

radii (1.74 to 1.70) or change in oxygen (O_{48f}) as on growing Ho^{3+} concentration over Gd^{3+} . Ho doping in the parent molecule was seen to cause a decrease in the structural ordering of the pyrochlore oxides. Even after varying the temperature (300 K to 2 K), spin glassy type transition could not be detected. This character is considered to be relevant to the fight between FM and AFM interaction, which is correlated to local structural disorder and magnetic frustration.

5.2 Experimental Procedure

$(Gd_{1-y}Ho_y)_2Ti_2O_7$ ($y = 0.0, 0.2, 0.4$ and 0.6) pyrochlores were formed by ordinary solid state reaction route [25-26]. Gd_2O_3 , Ho_2O_3 and TiO_2 ingredients with purity $>99.99\%$ were bought by sigma Aldrich. These precursors were taken in stoichiometric proportion and ground in ball mill (high energy) for 10.0 hours with ethanol as mixing intermediate. In order to prevent the powder's unwanted effects from being generated by excessive heating, a 45-minute break was kept between each hour of grinding while ball milling. The powdered ingredient was converted into cylindrical pellets with diameter of 8 millimetres. Synthesized pellets of all compositions were sintered at 30 hours ($1250^\circ C$) in the air furnace. Samples were calcined at $1300^\circ C$ for 24 hours after regrinding and repalletization. **Fig. 5.1** illustrates the synthesis procedure's detailed algorithm. XRD (Rigaku Miniflex 600) results were collected in the range of $10 - 80^\circ$ with rate of scanning 2.0° per minute. The collected XRD data was analysed through Fullprof program Rietveld refinement [27]. Structural ordering and phonon anharmonicity were considered using Raman spectra (with YAG laser 532 nm Nd: alpha 300 RA WiTec system) between range of $100 - 800\text{ cm}^{-1}$ at room temperature. Factual concentration of the prepared compounds was estimated by EDX spectrometer. Physical properties measurement system (cryogenics limited manufactured) was employed to perform dc magnetic measurements of each composition.

Throughout the measurement, there were changes in the functional magnetic field between -70 kOe and +70 kOe.

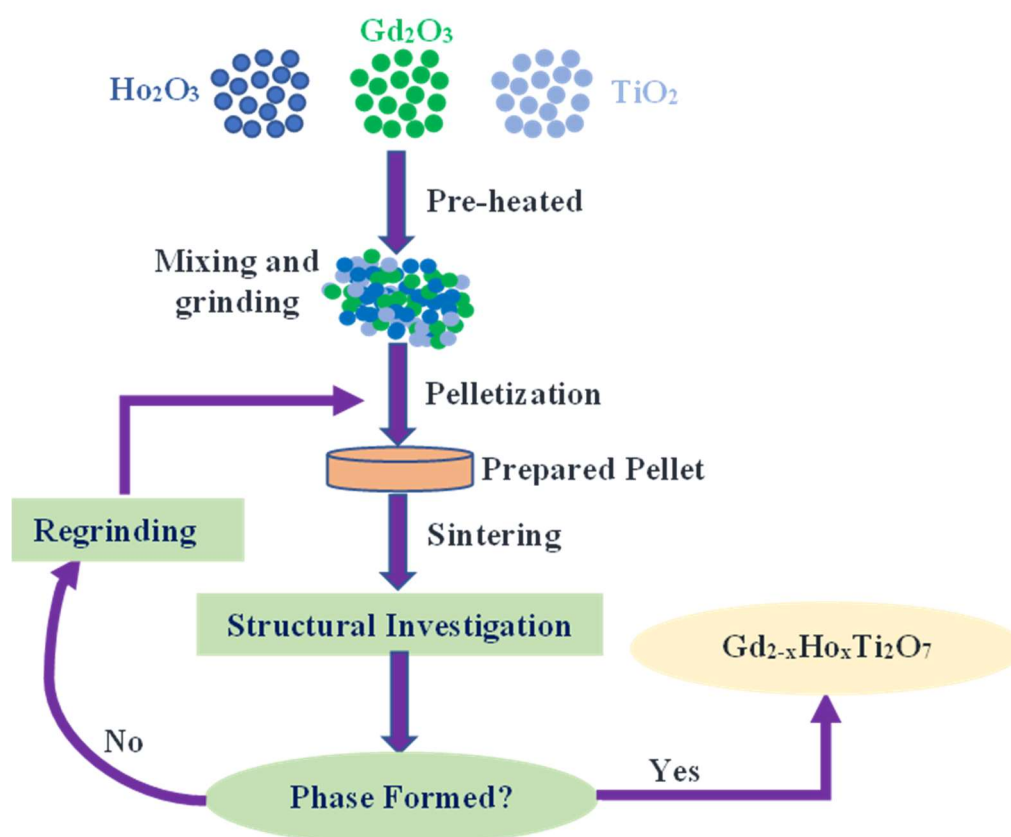


Fig. 5.1 Schematic figure of method used in the synthesis of $(Gd_{1-y}Ho_y)_2Ti_2O_7$ samples.

5.3 Results and Discussions

5.3.1 Stability and Structural Investigation Using XRD

The ionic radius ratio of cations A^{3+} and Ti^{4+} is crucial aspect impacting stability of $A_2Ti_2O_7$ ceramic. We have evaluated ionic radius ratio for each specimen using eq. (5.1), [19] which is listed in **Table 5.1**. The ions Gd^{3+} , Ho^{3+} , and Ti^{4+} have ionic radii of 1.053 Å, 1.015 Å and 0.605 Å correspondingly. Ionic radius ratio values for all compositions range from 1.46 to 1.78, which is a definite sign that each sample has a pyrochlore structure. The linear decrease in the

R_A/R_{Ti} (Ionic radii ratio) with increasing Ho concentration in $(Gd_{1-y}Ho_y)_2Ti_2O_7$ ($y = 0.0, 0.2, 0.4$ and 0.6) specimens leads to increase in structural disorder. On doping of Ho content (R_A/R_B decreases) or we can say size difference (between A and B cations) diminutions it shows that pyrochlore structure weakening or less probability of pyrochlore superstructural ordering.

$$\frac{R_{Gd/Ho}}{R_{Ti}} = \frac{(1-y) R_{Gd} + y R_{Ho}}{R_{Ti}} \dots \dots \dots (5.1)$$

The single phase pyrochlore structure is supported by data of XRD taken at room temperature for each component of the GHTO series. Every sample has a pure, uncontaminated pyrochlore phase. The acquired data were improved using Rietveld refinement founded on the locations of Fd-3m atoms. The refined XRD data of $(Gd_{1-y}Ho_y)_2Ti_2O_7$ system are displayed in **Fig. 5.2 (a, b, c and d)**. Using the Fullprof-2005 software, the refinement process has been carried out in two parts [28]. Le Bail refining, which involves the refinement of background, scale factor, cell parameters, and peak shape parameters, was carried out in the first step. Selecting a number of baseline points allowed the linear interpolation method to approximate the background. To simulate XRD peaks, a pseudo-Voigt function that merges Gaussian and Lorentzian profiles was applied. The 48f oxygen x parameter and their occupancies were refined as part of the Rietveld refinement process in the second stage. **Table 5.1** illustrates the refined features of GHTO specimens.

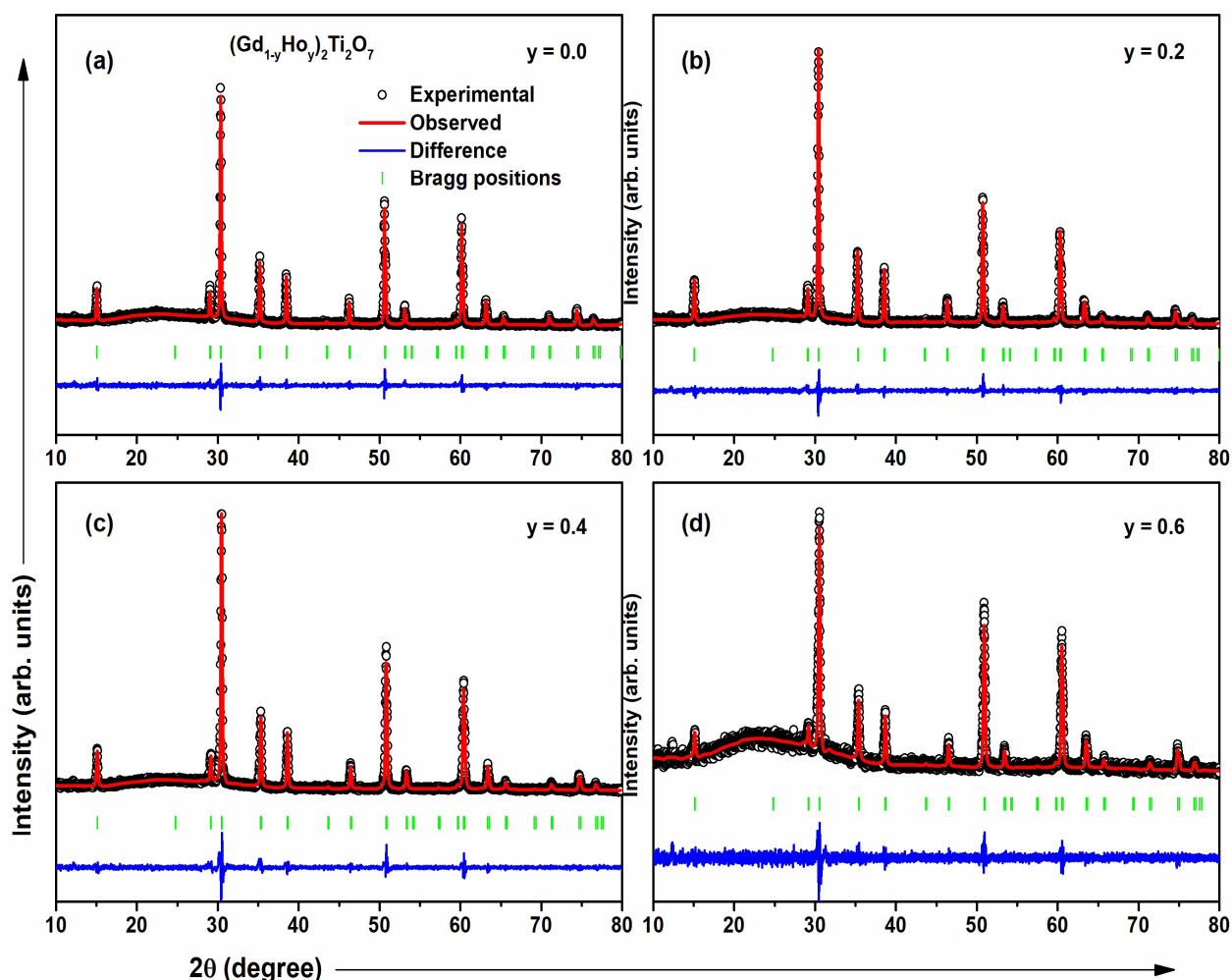


Fig. 5.2 A series of refined XRD patterns of $(Gd_{1-y}Ho_y)_2Ti_2O_7$ with concentration of Ho: (a) $y = 0.0$, (b) 0.2 , (c) 0.4 , and (d) 0.6 .

Since two different types of diffraction maxima are present in the pyrochlore XRD data. High-intensity peaks for GHTO were identified at $2\theta = 30.52^\circ, 35.49^\circ, 50.24^\circ, 60.48^\circ, 63.53^\circ,$ and 71.23° , respectively. These peaks referred to the even miller indices (222), (400), (440), (622), (444), and (800). These peaks exhibit a fluorite structure that is anion-deficient fluorite. In the second instance, XRD peaks (low intensity) were also identified at $2\theta = 15.34^\circ, 28.24^\circ, 38.23^\circ,$

47.73°, and 53.29° with odd miller indices (111), (311), (331), (511), and (531) that correspond to ordered superstructure pyrochlore. These two sorts of peaks are therefore part of the ordered pyrochlore superstructure (Fd-3m), which also has 3 different oxygen Wyckoff spots and three different forms of cationic configurations surrounding it [29-30].

Table 5.1 The structural parameters for $(Gd_{1-y}Ho_y)_2Ti_2O_7$ that were calculated from W-H plots and Rietveld analyses.

$(Gd_{1-y}Ho_y)_2Ti_2O_7$	y = 0.0	y = 0.2	y = 0.4	y = 0.6
Ionic radius ratio (R_A/R_{Ti})	1.74	1.72	1.71	1.70
Crystallite size (nm)	77 (4)	70 (3)	57 (3)	55 (3)
Microstrain (%)	0.100 (8)	0.109 (6)	0.080 (10)	0.078 (8)
Cell parameter (Å)	10.1948 (3)	10.1746 (3)	10.1600 (4)	10.1428 (4)
48f (x, 0, 0)	0.3208 (3)	0.3214 (4)	0.3224 (3)	0.3257 (5)
Gd/Ho–O_{48f} bond length (Å)	2.5640 (6)	2.5619 (4)	2.5575 (7)	2.5180 (8)
Gd/Ho–O_{8b} bond length (Å)	2.2072 (4)	2.2029 (1)	2.1997 (1)	2.1960 (6)
Ti–O_{48f} bond length (Å)	1.9505 (3)	1.9437 (2)	1.9360 (3)	1.9347 (4)
R_p, R_{wp}, R_{exp}, and χ^2	23.0, 19.8, 15.2, and 1.69	21.8, 18.4, 14.8, and 1.55	24.0, 20.9, 14.3, and 2.14	27.8, 21.2, 17.9, and 1.34

The lattice parameter is observed to decrease with rising Ho doping based on the results of the Rietveld refinement analysis. Doping Ho at site A rather than Gd implies that a smaller ion is accommodated in the structure, and the structure should undergo lattice shrinkage. It should be noticed that the XRD peak (111) shifts to higher 2θ values (right side shifting). The peak shifting behavior of the XRD data is shown in **Fig. 5.3 (a)**. The peak shifts to higher 2θ values when cell parameters are decreased with Ho doping at the A-site because Ho^{3+} ionic radius (1.015 Å) is less than Gd^{3+} (1.053 Å) ionic radius. Moreover, **Fig. 5.3 (b)**. Shows the variation of O_{48f} parameter with Ho concentration in $(\text{Gd}_{1-y}\text{Ho}_y)_2\text{Ti}_2\text{O}_7$. As the amount of Ho increases in the place of Gd, the x parameter of O_{48f} increases, signifying a decrease in the strength of pyrochlore. The migration of the x parameter of O_{48f} is another factor that describes the strength of the pyrochlore superstructure in addition to the ionic ratio ratios. It is determined that the structure with an O_{48f} x value near 0.3125 is a more ordered pyrochlore structure [31].

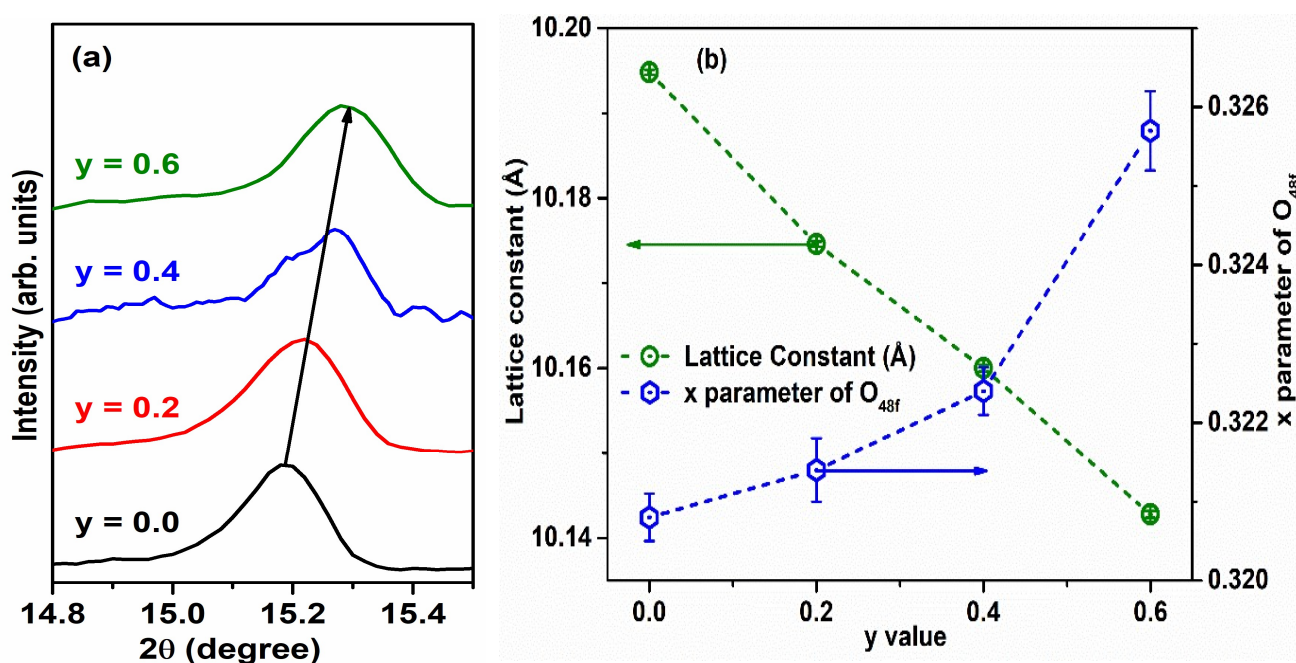


Fig. 5.3 (a) A shift in (111) diffraction maximum, **(b)** variation in lattice constant and x - parameter of O_{48f} as on increasing Ho concentration in $(\text{Gd}_{1-y}\text{Ho}_y)_2\text{Ti}_2\text{O}_7$.

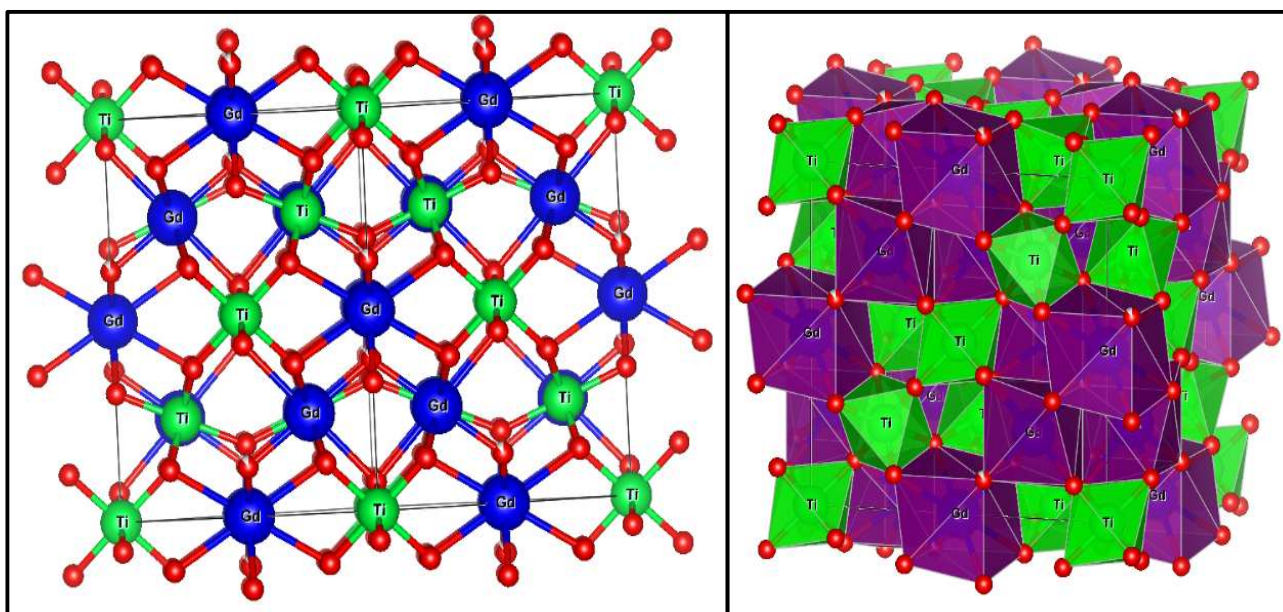


Fig. 5.4 Refined crystal structure for $Gd_2Ti_2O_7$. Violet polyhedron represents $[GdO_6^{48f}O_2^{8b}]$ hexagonal bipyramid and green polyhedron represents TiO_6^{48f} octahedra.

The refined crystal structure of $Gd_2Ti_2O_7$ has been shown in **Fig. 5.4**. In this crystal structure Violet polyhedron represents $[GdO_6^{48f}O_2^{8b}]$ hexagonal bipyramid and green polyhedron represents TiO_6^{48f} octahedra. It is evident that Gd^{3+} exists in an ideal cube geometry with eight coordinates, but Ti^{4+} is in a distorted octahedron geometry with six coordinates. These are the features of a typical fluorite flaw structure [32-33]. The Williamson-Hall approach was used to quantify the crystallite size and microstrain (structural parameters) by linearly fitting the data points of $\beta\cos\theta$ as a function of $4\sin\theta$. Wavelength of the employed X-rays source for the copper K line is 1.54 Å, and structural parameter (k) is maintained at 0.94 for spherical crystals with this cubic regularity. **Fig. 5.5** displays W-H plots for (a) $Gd_2Ti_2O_7$, (b) $Gd_{1.6}Ho_{0.4}Ti_2O_7$, (c) $Gd_{1.2}Ho_{0.8}Ti_2O_7$ and (d) $Gd_{0.8}Ho_{1.2}Ti_2O_7$. Additionally, **Fig. 5.5 (e)**

displays a fluctuation in the detected crystallite size and microstrain, which are determined from the y-intercept and slope of the linear W-H plot and are also presented in **Table 5.1**.

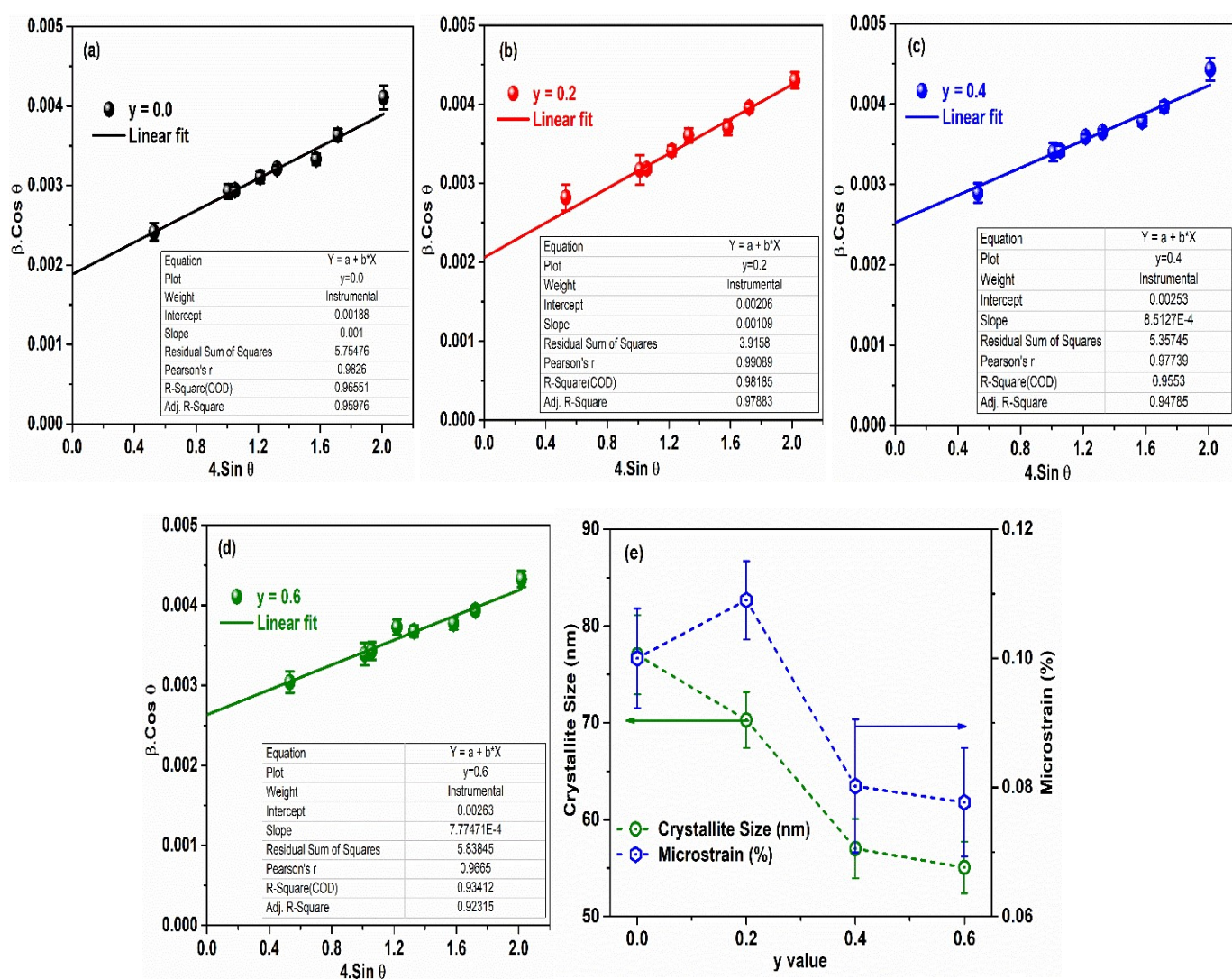


Fig. 5.5 Williamson-Hall (W-H) plots of $(Gd_{1-y}Ho_y)_2Ti_2O_7$ with concentration of Ho: (a) $y = 0.0$, (b) 0.2, (c) 0.4, and (d) 0.6 and (e) a variation in crystallite size and microstrain as a function of Ho concentration.

It was noticed that as Ho^{3+} ions concentration increased crystallite size decreased. This is due to the reductions in the size difference between A and B cations on Ho substitution. Along with

that microstrain was found to drastically diminish for the compositions with the doping of Ho ($y = 0.2, 0.4$ and 0.6) for $(\text{Gd}_{1-y}\text{Ho}_y)_2\text{Ti}_2\text{O}_7$ compounds. This states that the merger of smaller-sized ions into cationic lattice causes the lattice to relax. Consequently, rigorous structural analysis reveals that all four synthesized specimens are fully single phasic with complete dissolution of Ho^{3+} ions at the location of Gd^{3+} .

5.3.2 Raman Spectroscopic Study

The analysis of structural behaviour in all specimens, such as distortions, defects, symmetry, phonon-phonon and electron-phonon interaction, is greatly aided by Raman spectroscopy [34]. It also indicates the degree of disorder and anharmonicity (phonon) in the materials. The Raman spectra of $(\text{Gd}_{1-y}\text{Ho}_y)_2\text{Ti}_2\text{O}_7$ ($y = 0.0, 0.2, 0.4$ and 0.6) pyrochlores are displayed in **Fig. 5.6 (a)**. In accordance with earlier findings, we designated the pyrochlore phonon modes as $(\Gamma = 4F_{2g} + A_{1g} + E_g)$ where $4F_{2g}$, A_{1g} and E_g are six active Raman modes for ideal $\text{A}_2\text{B}_2(\text{O}1)_6(\text{O}2)_1$ pyrochlore [35]. The factor group theory [36] supports each of these phonon modes. The Raman spectra for the compositions **(b)** $y = 0.0$, **(c)** $y = 0.2$, **(d)** $y = 0.4$ and **(e)** $y = 0.6$ was deconvoluted into seven Raman active bands and the estimated position are listed in **Table 5.2**.

Two Raman modes ($F_{2g} + E_g$) with F_{2g} mode owing to $\text{O}_{48f}\text{-Gd(Ho)-O}_{48f}$ (bending mode) and E_g mode assigning to sublattice (O_{48f}) modes can be found in the highest intensity peak at 310.8 cm^{-1} . The Gd(Ho)-O_{48f} stretching bonds are allied with the 2nd intense peak at 516.7 cm^{-1} , which is designated as the A_{1g} mode. F_{2g} mode is allocated to least frequency band around 157.5 cm^{-1} . According to **Fig. 5.6 (a)** the O_{8b} sublattice vibration is related to the first allocated F_{2g} mode. Locations of the last two F_{2g} Raman modes are 419.1 cm^{-1} and 552.7 cm^{-1} correspondingly. Two

more modes beyond 600 cm^{-1} (specified by asterisk), which are either infrared (high frequency) active modes or higher order excitation should be noticed [37].

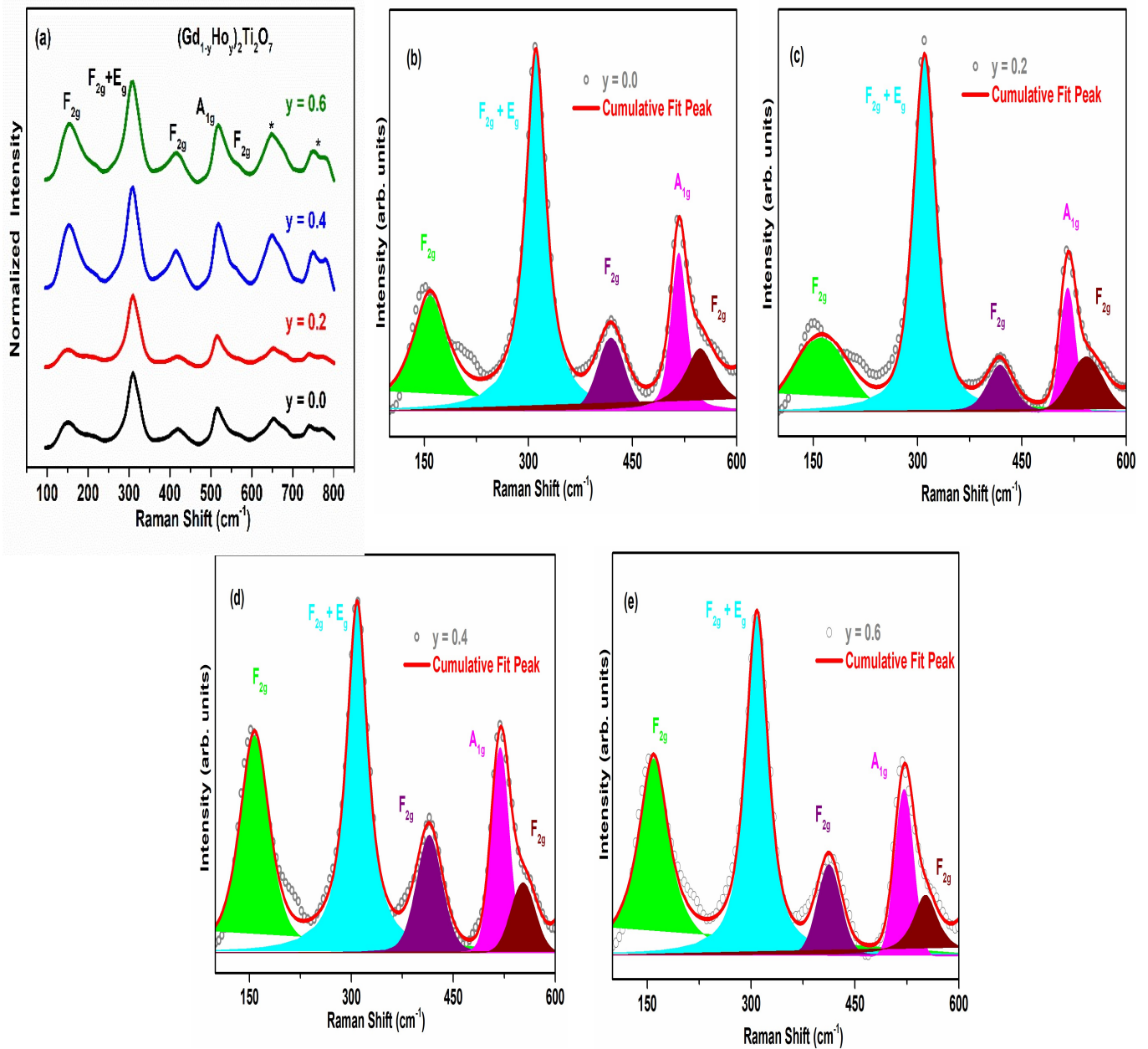


Fig. 5.6 (a) Raman spectrum of $(\text{Gd}_{1-y}\text{Ho}_y)_2\text{Ti}_2\text{O}_7$ with $y = 0.0, 0.2, 0.4$ and 0.6 **(b-e)** Raman spectra that have been deconvoluted for $y = 0.0, 0.2, 0.4$ and 0.6 .

Table 5.2 Deconvoluted Raman active mode locations for each of the three compositions.

$(\text{Gd}_{1-y}\text{Ho}_y)_2\text{Ti}_2\text{O}_7$	$F_{2g} (\text{cm}^{-1})$	$F_{2g} + E_g (\text{cm}^{-1})$	$F_{2g} (\text{cm}^{-1})$	$A_{1g} (\text{cm}^{-1})$	$F_{2g} (\text{cm}^{-1})$
$y = 0.0$	157.5	310.8	419.1	516.7	552.7
$y = 0.2$	158.6	310.3	418.5	515.9	551.9
$y = 0.4$	159.2	308.6	414.7	519.0	547.5
$y = 0.6$	161.0	308.4	412.6	521.0	542.9

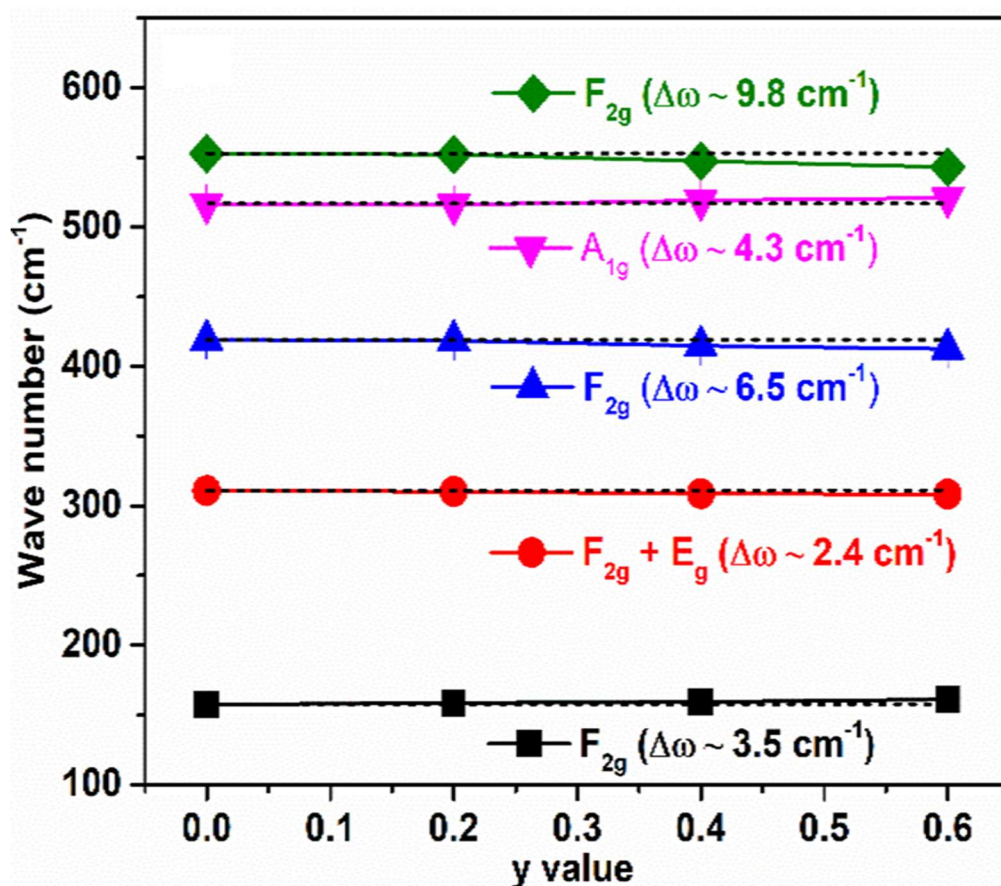


Fig. 5.7 Raman active modes vary in relation to the amount of Ho doping.

The Raman active modes as a variation of Ho concentration are described in **Fig. 5.7** [38]. Raman bands (F_{2g} and A_{1g}) were seen to shift to the higher wavenumber side (blue shift) with increase in Ho content. The observed decrease in the bond lengths (increasing force constant) of Gd/Ho–O_{48f} and Gd/Ho–O_{8b} as estimated from refinement of XRD data (**Table 5.1**) is likewise consistent with this blue shift. On the other hand, The Raman modes ($F_{2g} + E_g, 2F_{2g}$) were observed to shift to the lower wavenumber side, as shown in **Fig. 5.7**. All of these bands exhibit a red shift with an increase in Ho concentration. The lattice contraction on the substitution of a smaller Ho³⁺ ion over Gd³⁺ is related to the shifting of phonon vibrations towards the lower wavenumber side (red shift). Notably, Ho³⁺ ion doping on the A-site supports a single phasic pyrochlore structure in all compounds in both Raman and XRD examinations.

5.3.3 Compositional Analysis by EDX

The compositions of elements of the prepared specimens were ascertained using energy-dispersive X-ray measurement. **Table 5.3** provides a summary of the corresponding calculated outcomes. We observe that the experimental composition of the Ti is lower than the nominal composition, which might be caused by TiO₂ volatility. Other rare earth titanates have also shown this type of behaviour [20, 39]. Furthermore, the EDX data for the Ho³⁺/Gd³⁺ ions at the doping of Ho³⁺ in place of the Gd³⁺ cation is supported by the A-cationic site. Thus, the observed EDX findings agree with the XRD and Raman results.

Table 5.3 The $(Gd_{1-y}Ho_y)_2Ti_2O_7$ compounds' nominal and experimental mass (%) are displayed.

$(Gd_{1-y}Ho_y)_2Ti_2O_7$	Nominal mass (%)				Experimental mass (%)		
	Gd	Ho	Ti	O	Gd	Ho	Ti
y = 0.0	60.22	0.00	18.34	21.44	60.79	0.00	18.07
y = 0.2	47.89	12.56	18.23	21.32	48.12	12.73	17.87
y = 0.4	35.72	24.98	18.12	21.19	36.23	25.18	17.56
y = 0.6	23.67	37.24	18.02	21.07	24.86	37.64	16.84

5.3.4 Study of DC Magnetization

DC magnetic characterization of all compositions has been carried out utilizing a vibrating sample magnetometer to examine the magnetic behaviour of GHTO specimens. All specimen's temperature-dependent magnetic susceptibility data up to 2K at a functional field of 1000 Oe were recorded. Magnetic susceptibility changes with temperature of GHTO compounds are depicted in **Fig. 5.8 (a, b, c and d)**. All compositions were found to display paramagnetic behaviour and zero-field cooling (ZFC) and field cooling (FC) graphs overlap. According to this reaction, even at 2K temperature not all compositions exhibit either a spin glassy state or spin ordering. Moreover, **Fig. 5.9 (a)** shows how the inverse susceptibility of GHTO specimen changes with temperature. Recorded graph displays linearity for all samples and complies with the Curie-Weiss equation $[\chi = \frac{C}{T-\theta_{cw}}]$ between the ranges of 2 K and 300 K. In above equation,

θ_{cw} denotes the CW temperature and C is CW constant. $C = \frac{N\mu_{eff}^2}{3K}$ (Where K symbolizes

Boltzmann constant and N is the Avogadro number) is used to get effective magnetic moment (μ_{eff}) [19].

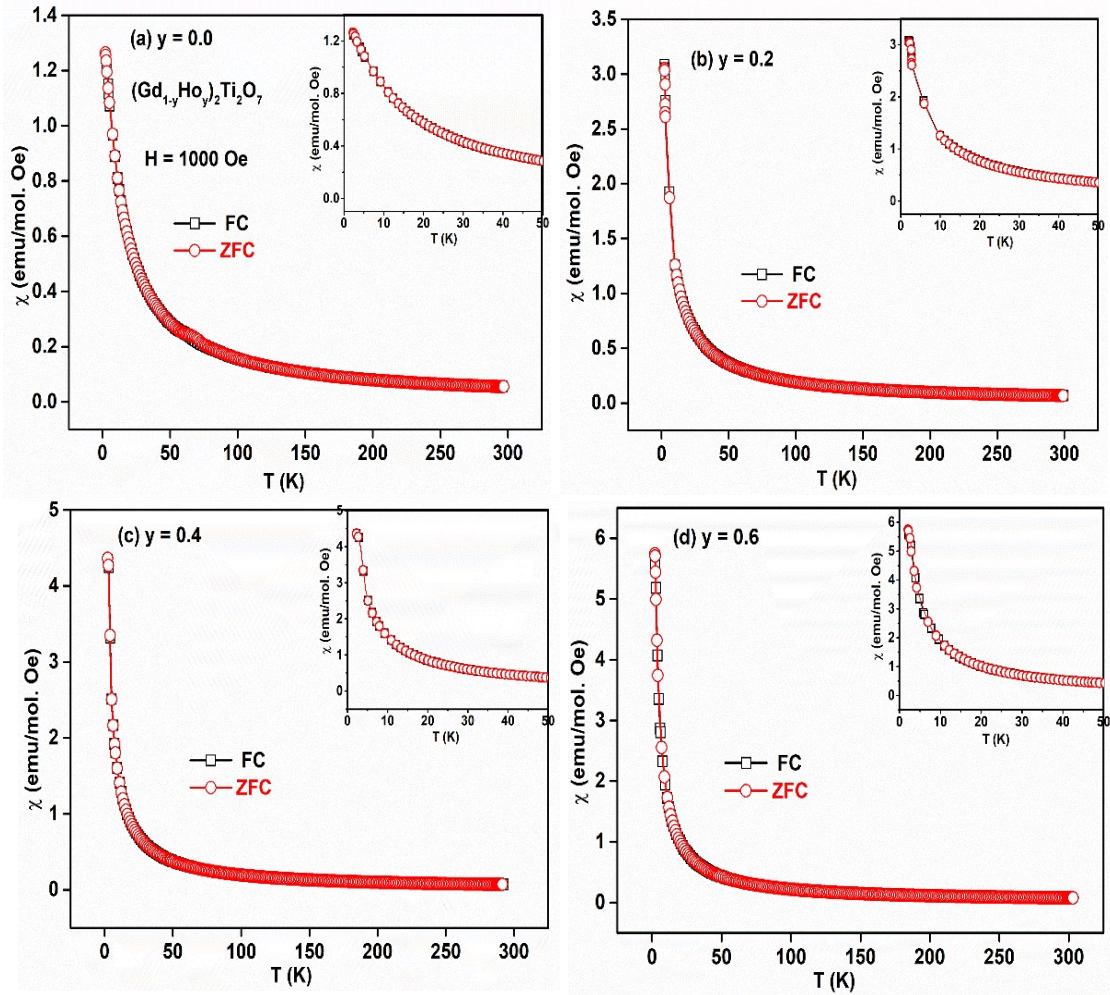


Fig. 5.8 Plots of $(Gd_{1-y}Ho_y)_2Ti_2O_7$ specimens magnetic susceptibility vs temperature (FC and ZFC) at operational field of 1 kOe for (a) $y = 0.0$ (b) $y = 0.2$ (c) $y = 0.4$ and (d) $y = 0.6$ Inset: FC and ZFC patterns recorded between 2 and 50 K.

$$\mu_{eff}^2 = p\mu_{Gd}^2 + q\mu_{Ho}^2 \dots\dots\dots(5.2)$$

Equation (5.2) is being used to derive theoretically effective magnetic moments. Where p and q denote the number of Gd and Ho atoms per f.u. correspondingly and μ_{Gd} and μ_{Ho} denote the respective magnetic moments of Gd and Ho atoms. Theoretical magnetic moment $\mu_{the} = g\sqrt{J(J+1)} \mu_B$ can be estimated using total angular momentum (J) and Lande g factor. The corresponding values for the Lande g factor ($g_{Gd} = 2$ and $g_{Ho} = 1.25$) and total angular moment ($J_{Gd} = 7/2$ and $J_{Ho} = 8$). So, the calculated (theoretically) magnetic moment (μ_{the}) for Gd^{3+} and Ho^{3+} is $7.94 \mu_B/Gd$ and $10.6 \mu_B/Ho$ respectively. Data was fitted in two temperature range (2 – 20 K and 100 – 300 K) in order to acquire the magnetic parameters. This acceptable temperature ranges were chosen because it is suitable for reduced crystal field excitation and avoids the influence of large crystal field splitting of Gd^{3+} . The same temperature ranges as in the earlier reports was employed for the fitting [40-41]. Fig. 5.9 (b, c and d) displays experimentally observed Curie Weiss temperatures (θ_{CW}) and magnetic moment (μ_{eff}). The reported values of θ_{CW} for $Gd_2Ti_2O_7$ and $Ho_2Ti_2O_7$ are -10.0 K and $+1.0$ K correspondingly [17-18]. According to our results, θ_{CW} is negative (Antiferromagnetic) when $y = 0$, but steadily rises with higher Ho^{3+} content, which is consistent with prior data [21].

The estimated values (Listed in Table 5.4) of the magnetic moment (μ_{eff}) were also found to increase with rising Ho contents. This entails that as the lattice is doped with much more Ho^{3+} ions, the magnetic interaction becomes more and more ferromagnetic. This could be the result of a shift in the dipolar and exchange interaction among the Gd^{3+} spins or ferromagnetic interaction among Gd–Ho (Ho–Ho) spins. Moreover, in comparison to theoretical data, the experimental magnetic moments (μ_{eff}) were found to be lower. It should be emphasized that exchange interaction among the half-filled (4f shell) of Gd^{3+} and 4f sublattice of Ho^{3+} is the reason why experimental values of μ_{eff} are lesser than those predicted by theory [39].

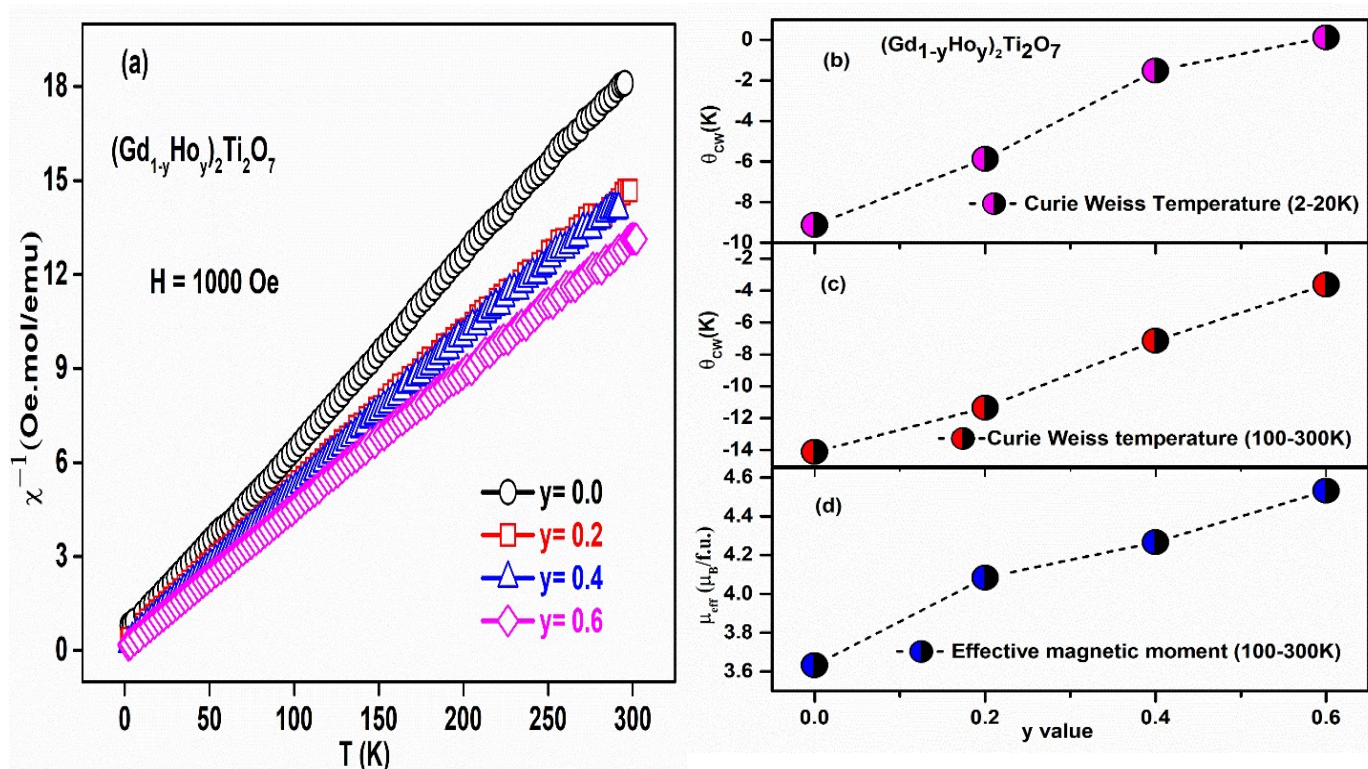


Fig. 5.9 (a) The temperature-dependent inverse susceptibility (χ^{-1}) curve for the GHTO ($y = 0, 0.2, 0.4,$ and 0.6) compounds. The estimated Curie Weiss temperatures from fitting at temperature range of **(b)** 2 – 20 K and **(c)** 100 – 300 K **(d)** Estimated effective magnetic moments at temperature (100 – 300 K).

Table 5.4 The magnetic parameters of $(\text{Gd}_{1-y}\text{Ho}_y)_2\text{Ti}_2\text{O}_7$ as observed experimentally.

$(\text{Gd}_{1-y}\text{Ho}_y)_2\text{Ti}_2\text{O}_7$	$\mu_{\text{eff}}/\text{f.u.}$ (μ_B)	$M_{\text{sat}}/\text{f.u.}$ (μ_B)	θ_{CW} (K) (2-20K)	θ_{CW} (K) (100-300K)
$y = 0.0$	3.64	13.32	-9.13	-14.13
$y = 0.2$	4.09	11.31	-5.87	-11.35
$y = 0.4$	4.27	9.46	-1.53	-7.16
$y = 0.6$	4.56	7.83	+0.14	-3.64

GHTO specimens M-H diagrams, which were captured at low temperature (2K) are shown in **Fig. 5.10**. It is noticed that magnetization decreases with raising the doping levels of holmium. **Table 5.4** summarises the saturation magnetization (M_{sat}) values that were estimated experimentally for the parent and all doped compounds. The magnetic (16d) site is the primary cause of the drop in saturation magnetization because the amounts of magnetic ions are increased (due to doping of Ho) at the 16d site for $(\text{Gd}_{1-y}\text{Ho}_y)_2\text{Ti}_2\text{O}_7$ system [42].

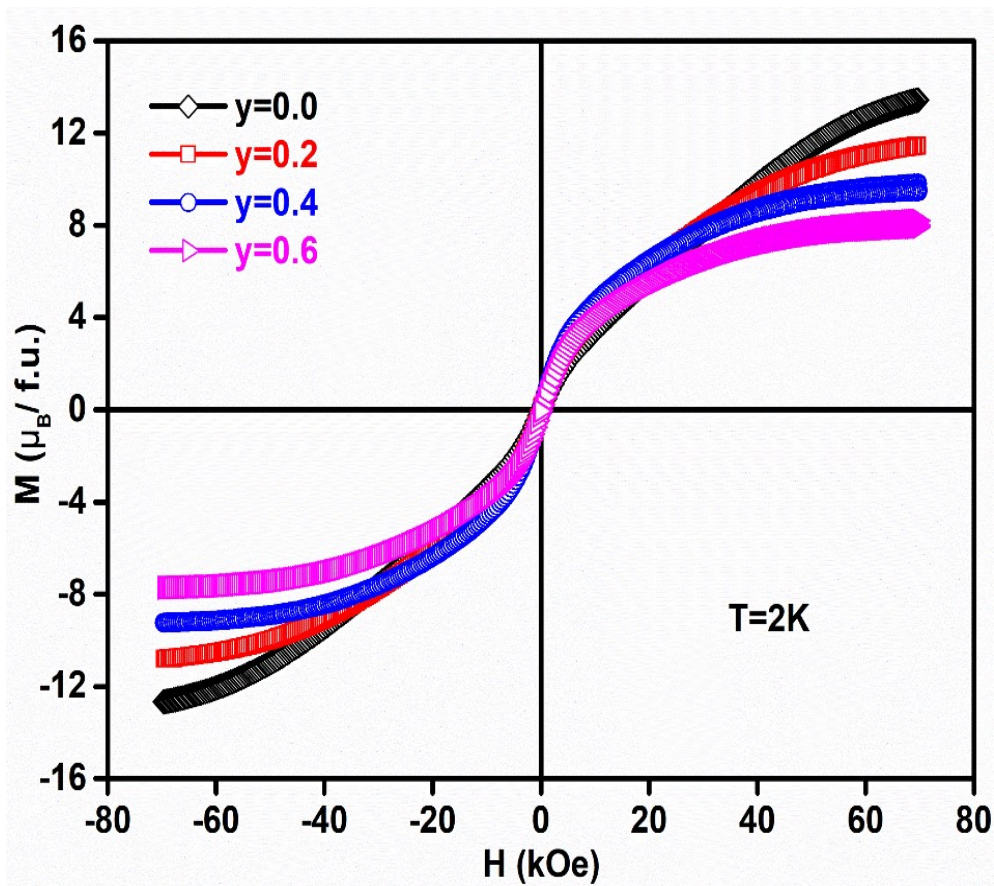


Fig. 5.10 M-H graphs of samples of $(\text{Gd}_{1-y}\text{Ho}_y)_2\text{Ti}_2\text{O}_7$ taken at 2 K.

Moreover, we see that the magnetization in the undoped compound ($y = 0.0$) does not approach saturation until the field is increased to 7 Tesla, and the values of saturation magnetization are reduced with rising in Ho concentration. It is evident that the system has a propensity for an improved ferromagnetic nature, which is linked to the current data increase in CW temperature (θ_{CW}). This might be because the spin angles of Gd-O-Ho increase and boost FM interaction among Gd-O-Ho spins [43].

It has been concluded that chemical pressure (Ho doping) effect enhances the FM (weaken AFM nature), which agrees with results of the inverse susceptibility versus temperature graph. Measured values of M_{sat} are lower than those estimated (theoretically) for $(Gd_{1-y}Ho_y)_2Ti_2O_7$ system owing to the effects of particle angular averaging and single ion anisotropy [24]. In our recently published articles, Kailash *et al.* [19, 31] reported that doping at the B and A sites in the $Ho_2Ti_2O_7$ reveals that θ_{CW} dropped by 33% and 71% owing to 10% doping of Ge^{4+} (smaller cation) at B site and La^{3+} (larger cation) at A site, correspondingly. In present study, θ_{CW} is found to increase 36% by the substitution of comparable amount of smaller cation (Ho^{3+}) at the A site of $Gd_2Ti_2O_7$. According to Liu *et al.* the θ_{CW} was decreased to 19% when the smaller ions Yb^{3+} were substituted (10%) at the A site of the $Dy_2Ti_2O_7$ [41]. Moreover, when nonmagnetic La^{3+} was substituted at the A site of $Dy_2Ti_2O_7$, CW temperature was lowered to 45% [40].

Based on these findings, it is logical to conclude that B site doping is more capable of controlling magnetic characteristics than A site doping. Furthermore, the nature and location of the dopant have an impact upon the value of θ_{CW} changes. As conclusion, when comparing the current work to prior findings, a higher increment in θ_{CW} was seen with an equivalent quantity of doping. This may be caused by the Gd-Ho cation's significant crystal field splitting.

In the future, when temperatures are such that spin ices are probably to freeze and become unstable, it would be intriguing to understand the crystallographic alterations of such systems.

5.4 Conclusion

In this chapter, Structural and magnetic investigation of $(\text{Gd}_{1-y}\text{Ho}_y)_2\text{Ti}_2\text{O}_7$ ($y = 0.0, 0.2, 0.4$ and 0.6) pyrochlore oxides have been studied by substitution of smaller cation Ho^{3+} in place of Gd^{3+} . Antiferromagnetically (AFM) linked Heisenberg spins are predicted to be extremely frustrating in the $\text{Gd}_2\text{Ti}_2\text{O}_7$ pyrochlore lattice because there are numerous ways to minimize the exchange energy. Each of the compositions was formed through ordinary solid state reaction route. Structural evaluation has proven that cubic pyrochlore (impurity-free) crystals with a cell parameter that continuously shrinkage and justifies Vegard rule. The crystallite size figured from W H graph is diminished with magnetic Ho substituting which is validate the reduction in structural ordering of prepared specimens. Raman bands show the red and blue shift of phone modes with increasing Ho content.

Result of rising Ho content is that there is increase in Curie Weiss temperature ($\theta_{\text{CW}} = -9.13$ to $+0.14$ K) and effective magnetic moment ($\mu_{\text{eff}}/\text{f.u.} = 3.64$ to $4.56 \mu_{\text{B}}$) and decrease in the ionic radii ratio (1.74 to 1.70), which leads to enhancement of ferromagnetic feature of the materials. Owing to the FM connections among Gd and Ho cations, the compounds exhibit a propensity toward a boosted FM interaction on Ho substitution. This character is considered to be relevant to the fight between FM and AFM interaction, which is correlated to local structural disorder and magnetic frustration. A significant rise in the θ_{CW} for $\text{Gd}_2\text{Ti}_2\text{O}_7$ doped with Ho^{3+} revealed that the θ_{CW} can be controlled by doping at the A site.

Furthermore, the glassy pattern could not be found even when the temperature was lowered by up to 2 K. In comparison of A and B site substitution, it can be said that doping at the B site is more effective at regulating magnetic features than doping at the A site. Moreover, a larger increment in θ_{CW} was observed with a similar amount of doping linked to the earlier studies. This might be brought on by the Gd-Ho cation's strong crystal field splitting. It would be exciting to examine the crystal structural transformations of such systems in the future at temperatures where spin ices are prone to freezing and becoming unstable.

References

1. Gardner, Jason S., Michel JP Gingras, and John E. Greedan. "Magnetic pyrochlore oxides." *Reviews of Modern Physics* 82, no. 1 (2010): 53.
2. Harris, Mark J., S. T. Bramwell, D. F. McMorrow, T. H. Zeiske, and K. W. Godfrey. "Geometrical frustration in the ferromagnetic pyrochlore $\text{Ho}_2\text{Ti}_2\text{O}_7$." *Physical Review Letters* 79, no. 13 (1997): 2554.
3. Morris, David Jonathan Pryce, D. A. Tennant, S. A. Grigera, B. Klemke, C. Castelnovo, R. Moessner, C. Czternasty et al. "Dirac strings and magnetic monopoles in the spin ice $\text{Dy}_2\text{Ti}_2\text{O}_7$." *Science* 326, no. 5951 (2009): 411-414.
4. Sharma, Saurabh K., Hari S. Mohanty, Dillip K. Pradhan, Ajay Kumar, Vivek K. Shukla, Fouran Singh, and Pawan K. Kulriya. "Structural, dielectric and electrical properties of pyrochlore-type $\text{Gd}_2\text{Zr}_2\text{O}_7$ ceramic." *Journal of Materials Science: Materials in Electronics* 31, no. 24 (2020): 21959-21970.
5. Yadav, Pramod Kumar, Pappu Kumar Harijan, Abhishek Tripathi, and Chandan Upadhyay. "Effect of A-site Fe substitution on the magnetic behavior of $\text{Dy}_2\text{Ti}_2\text{O}_7$ spin ice." *Journal of Magnetism and Magnetic Materials* 481 (2019): 221-226.
6. Sharma, Saurabh Kumar, V. Grover, A. K. Tyagi, D. K. Avasthi, U. B. Singh, and P. K. Kulriya. "Probing the temperature effects in the radiation stability of $\text{Nd}_2\text{Zr}_2\text{O}_7$ pyrochlore under swift ion irradiation." *Materialia* 6 (2019): 100317.
7. Sharma, S. K., V. Grover, R. Shukla, A. Hussain, A. Mishra, R. C. Meena, and P. K. Kulriya. "Evidence of improved tolerance to electronic excitation in nanostructured $\text{Nd}_2\text{Zr}_2\text{O}_7$." *Journal of Applied Physics* 129, no. 11 (2021): 115902.

8. Kumar, A., P. K. Kulriya, S. K. Sharma, V. Grover, A. K. Tyagi, and V. K. Shukla. "Structural and compositional effects on the electronic excitation induced phase transformations in $Gd_2Ti_2-yZr_yO_7$ pyrochlore." *Journal of Nuclear Materials* 539 (2020): 152278.
9. Oh, Si Hyoung, Robert Black, Ekaterina Pomerantseva, Jin-Hyon Lee, and Linda F. Nazar. "Synthesis of a metallic mesoporous pyrochlore as a catalyst for lithium– O_2 batteries." *Nature chemistry* 4, no. 12 (2012): 1004-1010.
10. Shlyakhtina, A. V., and L. G. Shcherbakova. "New solid electrolytes of the pyrochlore family." *Russian Journal of Electrochemistry* 48, no. 1 (2012): 1-25.
11. Bramwell, Steven T., and Michel JP Gingras. "Spin ice state in frustrated magnetic pyrochlore materials." *Science* 294, no. 5546 (2001): 1495-1501.
12. Balents, Leon. "Spin liquids in frustrated magnets." *Nature* 464, no. 7286 (2010): 199-208.
13. Hanawa, M., Yuji Muraoka, T. Tayama, T. Sakakibara, J. Yamaura, and Z. Hiroi. "Superconductivity at 1 K in $Cd_2Re_2O_7$." *Physical Review Letters* 87, no. 18 (2001): 187001.
14. Binder, Kurt, and A. Peter Young. "Spin glasses: Experimental facts, theoretical concepts, and open questions." *Reviews of Modern physics* 58, no. 4 (1986): 801.
15. Clancy, J. P., J. P. C. Ruff, S. R. Dunsiger, Y. Zhao, H. A. Dabkowska, J. S. Gardner, Y. Qiu, J. R. D. Copley, T. Jenkins, and B. D. Gaulin. "Revisiting static and dynamic spin-ice correlations in $Ho_2Ti_2O_7$ with neutron scattering." *Physical Review B* 79, no. 1 (2009): 014408.

16. Fritsch, K., K. A. Ross, Y. Qiu, J. R. D. Copley, T. Guidi, R. I. Bewley, H. A. Dabkowska, and B. D. Gaulin. "Antiferromagnetic spin ice correlations at (12, 12, 12) in the ground state of the pyrochlore magnet $Tb_2Ti_2O_7$." *Physical Review B* 87, no. 9 (2013): 094410.
17. Raju, N. P., M. Dion, M. J. P. Gingras, T. E. Mason, and J. E. Greedan. "Transition to long-range magnetic order in the highly frustrated insulating pyrochlore antiferromagnet $Gd_2Ti_2O_7$." *Physical Review B* 59, no. 22 (1999): 14489.
18. Cornelius, A. L., and J. S. Gardner. "Short-range magnetic interactions in the spin-ice compound $Ho_2Ti_2O_7$." *Physical Review B* 64, no. 6 (2001): 060406.
19. Chandra, Kailash, Vinod Singh, Saurabh K. Sharma, and Pawan K. Kulriya. "Structural magnetic properties correlation in Ge doped frustrated $Ho_2Ti_2O_7$ pyrochlore." *Journal of Magnetism and Magnetic Materials* (2022): 169694.
20. Liu, Hui, Youming Zou, Langsheng Ling, Lei Zhang, Changjin Zhang, and Yuheng Zhang. "Enhanced ferromagnetism and emergence of spin-glass-like transition in pyrochlore compound $Dy_2Ti_{2-x}V_xO_7$." *Journal of Magnetism and Magnetic Materials* 388 (2015): 135-142.
21. Marques, M. D. R., F. S. Portela, A. A. M. Oliveira, PetrucioBarrozo, N. O. Moreno, P. C. A. Brito, and J. Albino Aguiar. "Structural and magnetic properties of pyrochlores $Gd_{2-x}M_xRu_2O_7$ (M= Ho, Y)." *Physica B: Condensed Matter* 407, no. 16 (2012): 3106-3108.
22. Petrenko, O. A., M. R. Lees, G. Balakrishnan, V. N. Glazkov, and S. S. Sosin. "Magnetic phases in a $Gd_2Ti_2O_7$ pyrochlore for a field applied along the [100] axis." *Physical Review B* 85, no. 18 (2012): 180412.

23. Berwal, Umang, Vinod Singh, and Rinku Sharma. "Structural and optical studies on Dy³⁺ doped Gd₂Ti₂O₇ pyrochlore as white light emission." *Ceramics International* (2022).
24. Singh, Prajyoti, Arkadeb Pal, Vinod K. Gangwar, Prince K. Gupta, MohdAlam, Surajit Ghosh, R. K. Singh, A. K. Ghosh, and Sandip Chatterjee. "Wasp–Waisted loop and spin frustration in Dy_{2–x}Eu_xTi₂O₇ pyrochlore." *J. of Magnetism and Magnetic Materials* 518 (2021): 167364.
25. Berwal, Umang, Vinod Singh, and Rinku Sharma. "Key role of Tb³⁺ doping on structural and photoluminescence properties of Gd₂Ti₂O₇ pyrochlore oxide." *Ceramics International* (2022).
26. Shukla, Manjari, Soma Banik, Rajan K. Pandey, and Chandan Upadhyay. "Role of chemical pressure on optical and electronic structure of Ho₂Ge_xTi_{2–x}O₇." *Journal of Physics: Condensed Matter* 32, no. 11 (2019): 115501.
27. Rodríguez-Carvajal, Juan. "Recent advances in magnetic structure determination by neutron powder diffraction." *Physica B: Condensed Matter* 192, no. 1-2 (1993): 55-69.
28. Rodriguez-Carvajal, J. "FULLPROF. 2k: Rietveld, profile matching and integrated intensity refinement of X-ray and neutron data, V 1.9 c." *Laboratoire Leon Brillouin, CEA, Saclay* (2001).
29. Ehlers, Georg, E. Mamontov, M. Zamponi, A. Faraone, Y. Qiu, A. L. Cornelius, C. H. Booth et al. "Frustrated spin correlations in diluted spin ice Ho_{2–x}La_xTi₂O₇." *Journal of Physics: Condensed Matter* 20, no. 23 (2008): 235206.
30. Chang, L. J., W. Schweika, Y-J. Kao, Y. Z. Chou, J. Perßon, Th Brückel, Hong-Chang Yang, Y. Y. Chen, and J. S. Gardner. "Magnetic correlations in Ho_xTb_{2–x}Ti₂O₇." *Physical Review B* 83, no. 14 (2011): 144413.

31. Chandra, Kailash, Vinod Singh, Saurabh K. Sharma, and Pawan K. Kulriya. "La³⁺ substitution effect on structural and magnetic properties of frustrated Ho₂Ti₂O₇ pyrochlore." *Journal of Alloys and Compounds* (2022): 168311.
32. Zuniga, Jose P., Santosh K. Gupta, Maya Abdou, Héctor A. De Santiago, Alexander A. Puretzky, Melonie P. Thomas, Beth S. Guiton, Jue Liu, and Yuanbing Mao. "Size, structure, and luminescence of Nd₂Zr₂O₇ nanoparticles by molten salt synthesis." *Journal of Materials Science* 54, no. 19 (2019): 12411-12423.
33. Singh, Hari, Saurabh Kumar Sharma, and P. K. Kulriya. "Electronic excitation driven structural evolution in Ce_{0.8}Zr_{0.2}O₂." *Ceramics International* (2022).
34. Mohanty, Hari Sankar, Tapabrata Dam, Hitesh Borkar, Dhiren K. Pradhan, K. K. Mishra, Ashok Kumar, Balaram Sahoo et al. "Structural transformations and physical properties of (1-x)Na_{0.5}Bi_{0.5}TiO₃-xBaTiO₃ solid solutions near a morphotropic phase boundary." *Journal of Physics: Condensed Matter* 31, no. 7 (2018): 075401.
35. Singh, Prajyoti, Arkadeb Pal, Vinod K. Gangwar, Surajit Ghosh, Ranjan K. Singh, A. K. Ghosh, and Sandip Chatterjee. "Spin freezing and field induced transition in (Tb_{1-x}Eu_x)₂Ti₂O₇: A magnetic property study." *Journal of Magnetism and Magnetic Materials* 490 (2019): 165512.
36. Glerup, Marianne, Ole Faurskov Nielsen, and Finn Willy Poulsen. "The structural transformation from the pyrochlore structure, A₂B₂O₇, to the fluorite structure, AO₂, studied by Raman spectroscopy and defect chemistry modeling." *Journal of Solid-State Chemistry* 160, no. 1 (2001): 25-32.
37. Maćzka, M., M. L. Sanjuán, A. F. Fuentes, L. Macalik, J. Hanuza, K. Matsuhira, and Z. Hiroi. "Temperature-dependent studies of the geometrically frustrated pyrochlores Ho₂Ti₂O₇ and Dy₂Ti₂O₇." *Physical Review B* 79, no. 21 (2009): 214437.

38. Subramanian, M. A., G. Aravamudan, and GV Subba Rao. "Oxide pyrochlores—a review." *Progress in Solid State Chemistry* 15, no. 2 (1983): 55-143.
39. Liu, Hui, Youming Zou, Langsheng Ling, Lei Zhang, Wei Tong, Changjin Zhang, and Yuheng Zhang. "Frustrated magnetism and dynamical properties in pyrochlore-type magnet $\text{Dy}_2\text{Ti}_{2-x}\text{Fe}_x\text{O}_7$." *Journal of magnetism and magnetic materials* 369 (2014): 107-113.
40. Liu, Hui, Jian Bian, Shiyun Chen, Yuan Feng, Yu Xie, and Baolong Fang. "Magnetic and dynamical properties in the diluted spin ice $\text{Dy}_{2-x}\text{La}_x\text{Ti}_2\text{O}_7$." *Journal of Magnetism and Magnetic Materials* 465 (2018): 316-322.
41. Liu, Hui, Youming Zou, Lei Zhang, Langsheng Ling, Hongyan Yu, Lei He, Changjin Zhang, and Yuheng Zhang. "Magnetic order and dynamical properties of the spin-frustrated magnet $\text{Dy}_{2-x}\text{Yb}_x\text{Ti}_2\text{O}_7$." *Journal of magnetism and magnetic materials* 349 (2014): 173-179.
42. Yadav, Pramod K., Pinki Singh, Manjari Shukla, Soma Banik, and Chandan Upadhyay. "Effect of B-site substitution on structural, magnetic and optical properties of $\text{Ho}_2\text{Ti}_2\text{O}_7$ pyrochlore oxide." *Journal of Physics and Chemistry of Solids* 138 (2020): 109267.
43. Feng, Yuan, Shoujin Zhu, Jian Bian, Feng Chen, Shiyun Chen, Cuiling Ma, Hui Liu, and Baolong Fang. "Magnetic and electrical transport properties of the pyrochlore iridate $\text{Bi}_{2-x}\text{Co}_x\text{Ir}_2\text{O}_7$." *Journal of Magnetism and Magnetic Materials* 451 (2018): 283-287.

Chapter 6

Summary and Future Perspective

This chapter provides a summary of the research done for the current thesis. Additionally indicated are future perspectives and directions for this work's expansion. This thesis focuses on the investigations of structural and magnetic behavior of pyrochlore structured ceramics ($A_2B_2O_7$) synthesized by standard solid-state method. The two main ideas of my work magnetism and geometric frustration are summarized in this chapter.

6.1 Summary

The present thesis key findings and conclusions are as follows:

- ❖ Firstly, The B-site Ge doped pyrochlore titanate $\text{Ho}_2(\text{Ti}_{1-x}\text{Ge}_x)_2\text{O}_7$ produced via solid state reaction is detailed in terms of its structural and magnetic properties. Structural evaluation it has been proven that impurity free cubic type pyrochlore crystals form with a lattice constant that continuously lowers and follows Vegard's law. The stiffening of the phonon mode due to phonon-phonon anharmonic interaction was further validated by a pyrochlore phase analysis using Raman spectroscopy. As the x value is increased, the computed crystallite size from the WH plot decreases from 94 nm to 54 nm. The SEM micrographs demonstrate the compact form of spherical grains with grain sizes on the order of $\sim 6.2 \mu\text{m}$, $\sim 4.9 \mu\text{m}$ and $\sim 3.8 \mu\text{m}$ as Ge concentration increases. This decreasing trend in grain size is correlated with either a decline in the samples' relative density or an increase in their porosity depending on the value of x. The magnetic studies come to the conclusion that the doped compound's ferromagnetic connection is less than that of pure $\text{Ho}_2\text{Ti}_2\text{O}_7$ leading to alteration of exchange and dipolar interaction. The outcome also shows that the energy barrier has changed as a result of the doped compounds altered crystal field levels. On the contrary, structural analysis reveals that the pyrochlore superstructural ordering increases with increasing x-value in $\text{Ho}_2(\text{Ti}_{1-x}\text{Ge}_x)_2\text{O}_7$ as seen by the increase in radii ratio (R_A/R_B) or change in O_{48f} oxygen as on rising Ge content over Ti. This leads to reduced ferromagnetic propensity in more stable pyrochlore structured compositions. Additionally, $\text{Ho}_2(\text{Ti}_{1-x}\text{Ge}_x)_2\text{O}_7$ showed no spin glassy pattern even after being cooled to 2 K in all compositions.

- ❖ In order to better understand the magnetic and structural behavior of $\text{Ho}_{2-x}\text{La}_x\text{Ti}_2\text{O}_7$ (A-site doping) pyrochlore Ho^{3+} was partially replaced with the magnetic La^{3+} . Structural research demonstrated the creation of a single-phasic, contaminant-free pyrochlore crystal structure with linearly increasing cell parameters that satisfy Vegard's law. The crystalline size (71 ± 5 nm, 87 ± 6 nm and 107 ± 5 nm for $x = 0.0, 0.1$ and 0.2 , respectively) considered from W-H plot is enlarged with nonmagnetic La doping which is in accordance with investigations using electron microscopy. All SEM micrograph specimens are composed of agglomerative, spherical micron-sized particles. With La doping, it was observed that the $\text{Ho}_{2-x}\text{La}_x\text{Ti}_2\text{O}_7$ system's pyrochlore oxides' structural ordering became more ordered. Raman spectra show that La^{3+} was completely dissolved in the $\text{Ho}_2\text{Ti}_2\text{O}_7$ host matrix without appreciably affecting its structural integrity which is consistent with the XRD findings. Through the insertion of La into $\text{Ho}_{2-x}\text{La}_x\text{Ti}_2\text{O}_7$ Raman measurements have revealed a red and blue shift of the phonon mode as well as an increase in structural ordering. All specimens didn't show the spin glassy phase and ferromagnetic features were seen to continuously deteriorate as a result of chemical pressure. A huge reduction in the CW temperature (as compared to B- site) in the case of $\text{Ho}_2\text{Ti}_2\text{O}_7$ substituted with La^{3+} proposed that A site doping is less sensitive than B site doping for regulating magnetic characteristics. A huge reduction in the θ_{CW} for $\text{Ho}_2\text{Ti}_2\text{O}_7$ doped with La^{3+} proposed that doping at the A site can be cast-off for tuning of the θ_{CW} .
- ❖ Further in this thesis, Structural and magnetic investigation of $(\text{Gd}_{1-y}\text{Ho}_y)_2\text{Ti}_2\text{O}_7$ ($y = 0.0, 0.2, 0.4$ and 0.6) pyrochlore oxides have been studied by substitution of Ho^{3+} in place of Gd^{3+} . Antiferromagnetically (AFM) linked Heisenberg spins are predicted to be

extremely frustrating in the $\text{Gd}_2\text{Ti}_2\text{O}_7$ pyrochlore lattice because there are numerous ways to minimize the exchange energy. Each of the compositions was formed through ordinary solid state reaction route. Both Raman and XRD findings supported the presence of a single phasic cubic pyrochlore structure. The crystallite size (77 (4), 70 (3), 57 (3) and 55 (3) for $y = 0.0, 0.2, 0.4,$ and $0.6,$ respectively) computed from WH graph is decreased with magnetic Ho substitution, which is employed to validate the deteriorate in structural ordering of the produced specimens. Raman bands show the red and blue shift of phone modes with increasing Ho content. Result of rising Ho content is that there is increase in Curie Weiss temperature ($\theta_{\text{CW}} = -9.13$ to $+0.14$ K) and effective magnetic moment ($\mu_{\text{eff}}/\text{f.u.} = 3.64$ to $4.56 \mu_{\text{B}}$) and decrease in the ionic radii ratio (1.74 to 1.70), which leads to enhancement of ferromagnetic feature of the materials. Although, Magnetic investigations did not reveal any evidence of a spin glassy pattern in all compositions. Magnetic studies have also demonstrated the system becomes less antiferromagnetic (AFM) character as a result of the increased chemical pressure in $\text{Gd}_2\text{Ti}_2\text{O}_7$. This is due to generation of ferromagnetic interaction among Gd–Ho (Ho–Ho) spins and disrupted network of Gd^{3+} ions. In comparison of A and B site substitution, it can be said that doping at the B site is more effective at regulating magnetic features than doping at the A site. It would be exciting to examine the crystal structural transformations of such systems in the future at temperatures where spin ices are prone to freezing and becoming unstable.

6.2 Future Perspective

The current thesis work provides a logical route for further research on a number of features.

There are a few potential prospects in the future quest for pyrochlore-structured compounds.

- ❖ It would be fascinating to make all of these pyrochlore using the Sol-gel and floating zone method and contrast the results with those made using the solid-state sintering method.
- ❖ High-pressure high-temperature synthesis may be used to substitute silicon a cation that is even smaller than germanium onto the pyrochlore B-site. Exchange interactions in the silicon spin ices $\text{Ho}_2\text{Si}_2\text{O}_7$ and $\text{Dy}_2\text{Si}_2\text{O}_7$ would be greatly improved over those in $\text{Ho}_2\text{Ge}_2\text{O}_7$. As a result, these materials would be pushed closer and closer to the spin ice phase diagram's critical point or perhaps into a brand-new net antiferromagnetic phase.
- ❖ To investigate the AC susceptibility and magnetization relaxation of $\text{Ho}_{2-x}\text{La}_x\text{Ti}_2\text{O}_7$ (A-site doping) and $\text{Ho}_2\text{Ti}_{2-x}\text{Ge}_x\text{O}_7$ (B-site doping) spin ice materials.
- ❖ Single ion anisotropy with dipolar exchanges was realized to harvest interesting magnetic assets. Examining this structure's whole AC and DC magnetic learning is exceedingly difficult.
- ❖ To justify the findings from magnetic measurements, one can investigate temperature-dependent neutron diffraction.
- ❖ To further evaluate the magnetic monopole similarities an active area of research is looking for new spin ice with significant monopole concentrations at low temperatures.